UNIVERSITY OF OKLAHOMA

GRADUATE COLLEGE

REACTIVATION MECHANISMS OF HETEROGENEOUS, COMPLEX FAULT ZONES

A DISSERTATION

SUBMITTED TO THE GRADUATE FACULTY

In partial fulfillment of the requirements for the

Degree of

DOCTOR OF PHILOSOPHY

By

VINCENT HEESAKKERS
Norman, Oklahoma
2010

REACTIVATION MECHANISMS OF HETEROGENEOUS,
COMPLEX FAULT ZONES

A DISSERTATION APPROVED FOR
CONOCOPHILLIPS SCHOOL OF GEOLOGY AND GEOPHYSICS

BY

Dr. Ze'ev Reches, Chair

Dr. Jean-Claude Roegiers

Dr. Shankar Mitra

Dr. Randy Keller

Dr. David Lockner

ACKNOWLEDGEMENTS

This dissertation would not have been possible without my advisor Dr. Ze'ev Reches, who encouraged and guided me to reach the heights and explore the depths on a professional and personal level. I am grateful to Ze'ev for my career and his time and dedication to share his wisdom, experience and knowledge on so many levels. Many thanks go to Dr. David Lockner for his mentorship and hospitality to host me in the lab of the USGS for rock mechanics experiments. I thank the other members of the advising committee: Dr. Jean-Claude Roegiers, Dr. Shankar Mitra, Dr. Randy Keller and Dr. David Stearns, for their involvement and flexibility to help me pursue this degree. Special thanks to all principal investigators of NELSAM for their support and assistance. I was assisted during my underground mapping and other activities in TauTona mine by many and I acknowledge all for the help and support: Matthew Zechmeister, Tom Dewers, Kate Moore, Curnell Campher, Selwyn Adams, Reggie Domoney and Amir Allam. I want to acknowledge Mark Zoback and Amie Lucier for their assistance and discussion regarding the stress analysis and the aid during underground activities by Amie. Thanks to Seth Busetti for his assistance with finite element modeling. I wish to distinguish employees of AngloGold Ashanti in TauTona mine, especially Shaun Murphy and all employees of the rock engineering and geology departments, for their hospitality, scientific discussions and great efforts to assist in logistics, but most of all to guard my safety during my stay. Credit goes out to Gerrie van Aswegen, Marie Gerenger and Talita Bacon for hosting me and providing assistance in many aspects during my visits to South Africa. I am thankful for the financial support of the National Science Foundation, USA (Grant # 0409605),

and ICDP towards the Natural Laboratory in South African Mines (NELSAM) project that made my research possible.

I thank my office mates Dustin Sweet, Jonathan Funk and Elisheva Patterson for their daily moral support and shenanigans, and my roommates Matthew Zechmeister and Dustin Sweet for unforgettable times we shared. Great help in my accomplishment was the appropriate distraction and support of close friends in both the US and The Netherlands. Every single one contributed in his or her own special way to give me strength to complete this degree. Special thoughts go out to a close friend, Andreas Lemmens, as his passing forms a memorable moment during the practice of my degree.

Finally, I dedicate this work to my mother, Lucia Vranken, and my sister, Angelique Heesakkers, for their sacrifice and immeasurable support towards my adventure to pursue this degree. Even the North Atlantic Ocean cannot separate “The three Musketeers”.

TABLE OF CONTENTS

LIST OF TABLES

LIST OF FIGURES

ABSTRACT

Fault reactivation occurs on a short-term cycle of tens to thousands of years between infrequent earthquakes, and on long-term cycles of fault inactivity for $10^6 – 10^7$ years. During long-term cycles, faults may heal and renew their strength. The objective of the present work is to study the mechanisms of fault reactivation after a long dormant period, when the pre-existing fault is not necessarily “weak”.

The study is conducted along the Pretorius fault, TauTona mine, South Africa. The deep gold mines in South Africa provide access to earthquake processes at focal depth, which was motivation for the NELSAM (Natural Earthquake Laboratory in South African Mines) project to develop an underground earthquake laboratory at ~3.5 km depth within TauTona mine (Ch. 1). The present study is conducted within the NELSAM site that includes the 2.7 Ga Pretorius fault, which has been inactive for at least 2.0 Ga and is currently being reactivated due to nearby mining activity. I characterize the fault zone by 3D underground mapping within mining tunnels at 3.6 km depth (Ch. 2). The structural analysis is accompanied by fracture analysis from borehole image logs and micro-structural studies. I find that the Pretorius fault is structurally complex, with a 20-30 m wide zone of anastomosing, dominantly steep fault segments that contain a strong cohesive sintered cataclasite. Despite the size of the Pretorius fault, a few km long with ~200m horizontal and 30-60 m vertical displacement, its complexity reflects the fault zone immaturity.

The exposed rupture zone of the M2.2 of December 12, 2004, was mapped in detail at focal depth (Ch. 3). It reactivated three to four quasi-planar, non-parallel segments of the Pretorius fault, with characteristic generation of fresh fine grained rock powder along the

contact of the quartzitic host rock and the cataclasite, indicating localization of slip during the event. To investigate the mechanism responsible for such localization, rock mechanics experiments were conducted on cataclasite and quartzite samples within the fault zone. The results show a mechanical contrast between the quartzite, that show significant strain hardening due to dilation of micro-cracks, and the weaker but more brittle cataclasite. A finite element analysis suggest that this mechanical heterogeneity effectively controls the localization of shear strain at the contact, similar to the observations of the M2.2 rupture and rock mechanics experiments.

The stresses associated with the M2.2 rupture are calculated from in-situ stress measurements on borehole failures of three boreholes within 60 m from the exposed rupture (Ch. 4). The calculations, combined with the geometry of the rupture zone, suggest that slip during the M2.2 occurred under low shear stress. It is likely that stress interaction between the reactivated segments, and dynamic weakening due to gouge formation and lubrication allowed such slip. The earthquake energy balance of the event is estimated by combining field observations and stress measurements with the seismic signal. It appears that the fracture energy cannot be ignored and contributes for ~ 1/3 to the total energy, similar to the frictional heat energy contribution.

The unique setting provided an extraordinary data set of a single earthquake with field observations at focal depth, rock mechanics, rupture-associated stresses and seismic signal. The results describe reactivation processes in detail and contribute to the understanding of earthquake mechanisms.

Chapter 1:

Fault Reactivation and Rupture Zones

OBJECTIVES AND APPROACH

It is generally accepted that brittle faults in the upper crust can be reactivated after periods of inactivity (Scholz, 1998). During active periods fault-zones typically move by infrequent earthquakes separated by tens to thousands of years, while displacement localizes along weak surfaces. Between earthquakes, fault-zones may experience fault-healing processes that renew their strength and resistance to rupture (Marone, 1998; Muhuri et al., 2003). This short-term cycle of fault activity, referred to as the earthquake cycle (Thatcher, 1983), terminates when faults become dormant due to changes in the regional tectonic activity. However, faults may be reactivated after being dormant for $10^6 – 10^7$ years, by younger tectonic phases, frequently with inversion of the sense of motion along the fault. Examples of fault reactivation after long term of inactivity have been observed along the Palisades fault, Grand Canyon (Reches, 1978), along faults within the Colorado Plateau, Arizona (Huntoon, 1974), the North Sea basin (Oudmayer and de Jager, 1993; Wiprut and Zoback, 2000), and at multiple scales from basins to small structures within a basin (Lowell, 1995). The long term of inactivity can lead to significant strengthening by cementation of fault rock, depending on associated fluids, mineralogy and cementation, similar to processes observed in shear bands (Fossen et al., 2007). Thus, pre-existing faults are not necessarily “weak” and later earthquakes can occur after the pre-existing fault has strengthened through time. While many fault-zone minerals are weak hydrated alteration products of the host rocks, quartz and calcite

cementation are common and under the right conditions, faults may heal to nearly undamaged rock strength.

The main objective of this dissertation is to study mechanisms of fault reactivation after long periods of inactivity, with emphasis on rupture and associated damage resulting from a single seismic event. Many studies of brittle fault zones in the upper crust are restricted to 2D field observations of partially exposed faults that accumulated multiple slip events and/or periods of fault healing, after which the fault zones are exhumed at the surface. Observations at outcrops are then often extrapolated to represent the characteristics of the fault zone under the assumption of a homogeneous fault system. To eliminate these limitations, the present work focuses on an ancient fault is a deep mine. The selected fault is the Pretorius fault in TauTona mine, located within the Witwatersrand Basin, South Africa (Fig. 1.1). The setting within the TauTona mine provided an outstanding site for an in-situ study of mechanisms of fault reactivation and rupture processes. The fault is being reactivated now by mining operations after a dormant period of ~2.0 Ga. The mine provides access to the fault-zone at ~3.5 km depth, and provides opportunities for high resolution, 3D, in-situ study of rupture processes. Several other studies analyzed ruptures within deep mines in South Africa, documenting rockbursts that formed in previously unfaulted regions (McGarr et al., 1979; Ortlepp, 1992, 2000). The only in-situ analyses of a rupture along a pre-existing fault-zone is the M4.6, Matjhabeng earthquake, 1999, along the Dagbreek fault, Welkom, South Africa (Dor et al., 2001).

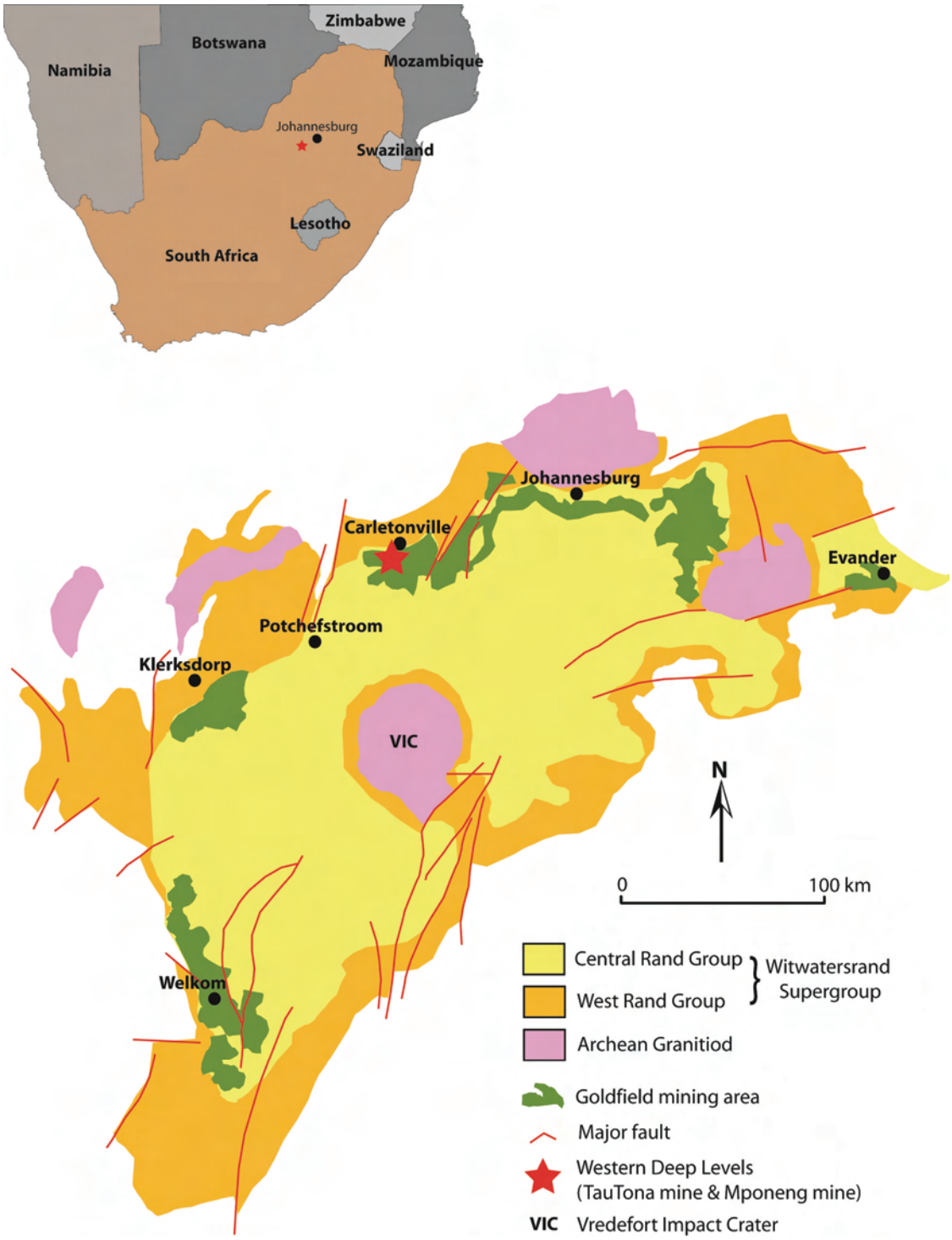

Figure 1.1: Simplified geological map of the Witwatersrand Basin, South Africa, illustrating the distribution of the Witwatersrand Supergroup and the Archean Granitoid, the major goldfields and the location of the TauTona and Mponeng mine in Western Deep Levels (after Frimmel and Minter, 2002).

SETTING OF THE STUDY

This study was conducted as part of the NELSAM (Natural Earthquake Laboratory in South African Mines) project, which is designed to investigate seismogenic processes at focal-depths of earthquakes in deep gold mines of South Africa (Reches, 2006; Reches and Ito, 2007). The mines provide a unique setting, with in-situ access to hypocenters of earthquakes of moment-magnitude -2 to as large as 4, where the larger magnitudes often occur along pre-existing fault-zones. Mining operations control the location, magnitude and timing of the earthquakes, and allow for installation of a variety of instruments in a three-dimensional array, at distances of 1-100 m from anticipated hypocenters. The setting within the mines provides opportunities to monitor fault activity before, during, and after an earthquake. The direct accessibility to active faults at focal depth allows studies of earthquake processes by integrating multiple disciplines. The scientific objectives of NELSAM are to contribute key data in the following areas:

I. Determination of scales and processes of the nucleation zone.

II. Detailed properties, dynamics and energetics of rupture process.

III. Stress/Strain/Strength distribution in rocks, in the vicinity of active faults.

IV. Characterization of active fault-zones.

V. Chemical compositional variations of fluid and gas during the earthquake cycle.

VI. Microbial activity along active faults.

To address the above objectives the NELSAM site was developed in an area covering 900 m^2, at a depth of ~3.5 km that is located in the SSE corner of the Tautona mine. The NELSAM site includes the future development of TauTona mine as well as the inactive,

2700 Ma old Pretorius fault. Within this site, a total of 18 vertical and inclined boreholes were drilled within tunnels at two different mining levels; level 118 (11,800 ft) and level 120 (12,000 ft). The boreholes were instrumented with: 3D broadband accelerometers, velocity seismometers, electrodes and thermisters, that form a dense 3D network around the Pretorius fault, a 110 m long strain meter that crosses the Pretorius fault, a gas emission monitoring system with onsite mass-spectrometer and gamma detector and a microbial monitoring system.

The establishment and layout of instrumentation at the NELSAM site is based on a detailed structural characterization of the Pretorius fault (Ch. 2). The exposure of the M2.2 event of December 12, 2004, was located during underground mapping of the fault-zone. Detail mapping of the rupture at focal depth revealed reactivation of several segments of the Pretorius fault (Ch. 3). The NELSAM drilling program provided core samples for rock mechanics analysis in the fault zone (Ch. 3), and borehole data for in-situ stress analysis (Ch. 4). This dissertation presents a unique multi-disciplinary dataset of 3D in-situ field observations, rock mechanics and stress measurements that are combined with finite element modeling, to analyze the mechanics and energetics of the M2.2 event along the Pretorius fault.

DISSERTATION ORGANIZATION

The main focus of this dissertation is to investigate the mechanisms of reactivation along the Pretorius fault in Tautona mine, South Africa. The dissertation is presented as stand-alone chapters that will be prepared for submission in major scientific journals:

Chapter 1 presents the framework for the study and its objectives.

Chapter 2 characterizes the 3D structure of the Pretorius fault, based on integration of underground mapping observations and borehole data analysis. The structural development, the 3D complexity and maturity of the fault-zone is described, including the origin of the massive, cohesive cataclastic fault rock that is observed along many segments of the Pretorius fault.

Chapter 3 includes three parts; a summary of detailed observations of the exposed rupture zone of the M2.2 2004 earthquake along the Pretorius fault; the mechanical properties of rocks the Pretorius fault-zone determined from rock-mechanics experiments; a finite element analysis of the mechanisms that control the reactivation of the Pretorius fault during this M2.2 event. It is postulated that rheological heterogeneities within fault-zones, and not necessarily the absolute strength, control the localization and reactivation of the pre-existing fault segments.

Chapter 4 presents an analysis of the stress state associated with the M2.2 rupture and combines the field observations with the seismic signal in order to estimate the energetics of the this event. Slip along the M2.2 rupture surfaces occurred under low resolved shear stress, suggesting significant weakening during the event. The radiation energy of the M2.2 event contributes for 2-13% to the total energy budget, the heat energy occupies at least 30%, and the estimated fracture energy contributes for at least 33% to the total energy budget.

Chapter 5 deals with a finite element analysis of the effects of rheology on the folding geometry above a single ramp system. The analysis indicates that fold asymmetry, fore-limb steepness and the location of maximum curvature with respect to the ramp,

are strongly affected by the weakness of the sedimentary cover, modeled by an elastic-plastic-damage material that undergoes significant dilation.

Chapter 2:

Structure of the Pretorius Fault, TauTona Mine, South Africa

INTRODUCTION

The NELSAM (Natural Earthquakes Laboratory in South African Mines) project was designed to study earthquake processes at their focal depth. The deep gold mines in South Africa provide an excellent setting to study such processes (Reches, 2006). The main research site is located on the Pretorius fault that is exposed at a depth of 3.6 km in TauTona mine, about 80 km west of Johannesburg, South Africa (Fig. 1.1). The Pretorius fault, one of the major faults within the Witwatersrand Basin, was formed ~2.7 Ga ago and has been inactive during the last 2.0 Ga. Currently, it is being reactivated by the active mining in TauTona mine (van Aswegen and Butler, 1993). Future mining development at deeper levels is likely to increase its seismic hazards. The NELSAM project includes a series of studies at this site, including seismological, geochemical and geo-biological analyses (Ch. 1) (Reches, 2006). The main objective of the present study is to analyze mechanisms of fault reactivation. The study focuses on the rupture zone of the M2.2 event of December 12, 2004 along the Pretorius fault, described in Ch. 3 and Ch. 4. An essential part of the study is structural characterization of the fault zone, which is the topic of this chapter.

The analysis of the Pretorius fault is based on 3D observations at 3.6 km depth and includes 3D mapping within tunnels, at a scale of 1:100 and 1:50, accompanied by mapping at a scale of 1:10. In addition, borehole data were analyzed from drilling across and near the Pretorius fault. The boreholes range in length from 10 to 50 m with

inclinations of 20° to vertical. In addition, microscopic work on the common fault rocks is incorporated (Zechmeister et al., 2005).

PRETORIUS FAULT-ZONE

This chapter discusses the structural characteristics of the Pretorius fault. First, the geological setting of the study area is outlined. Next, large and small scale features of the fault-zone are described from underground observations, followed by analysis of brittle fractures within and near the Pretorius fault that were found in borehole image logs. Finally, the nature of fault rocks from both field and microscopic observations is presented. The structural development of the fault zone is discussed, followed by the origin of the fault rocks.

GEOLOGICAL SETTING

The Pretorius fault is located in the Western Deep Levels of the Achaean Witwatersrand Basin, South Africa (Fig. 1.1). The basin contains the world's largest known gold province. Gold mineralization is mainly concentrated within conglomerate horizons of the West Rand and Central Rand Groups, often within hydrocarbon seams of a few cm thickness (Frimmel and Minter, 2002). The Witwatersrand Basin is a 350 × 200 km NE trending basin that developed in a foreland thrust setting during the convergence of the Zimbabwe plate and the Kaapvaal Craton, during the later stage of the West Rand, about 2.9 Ga ago (Gibson et al., 2000b; Robb et al., 1997). The basin accumulated the Witwatersrand Supergroup sediments of 2.71 – 2.97 Ga age, a 7-10 km thick sequence of terrigenous sedimentary rocks, comprising mainly of sandstones and mudrock, together with minor conglomerate horizons (Armstrong et al., 1991; Gibson et al., 2000b; Robb et

al., 1997). The region experienced continuous thrusting into the Central Rand stage until 2.7 Ga BP (Gibson et al., 2000b). The sedimentation was followed by up to 3 km thick tholeiitic flood basalts from the Ventersdorp Supergroep during the Platberg rifting. This was followed by up to 2 km of local rift sediments (Gibson et al., 2000b). Most of the Kaapvaal Craton was covered by a shallow sea 2.6 Ga ago, after which a period of slow subsidence was followed by deposition of the 2-3 km thick Pretoria Group. At the later stage of the Platberg rifting, the basin underwent low-grade burial metamorphism up to lower greenschist grades (Robb et al., 1997). Peak metamorphism coincided with the emplacement of the mafic and ultramafic Bushveld intrusion at 2050 Ma (Robb et al., 1997). This resulted in major thermal perturbations of the basin. The Vredefort meteorite impact at 2024 Ma (Kamo et al., 1996) was followed by a significant uplift of the basin and a retrograde overprint of the metamorphism. Eroded and uplifted structures gave rise to the younger (~200 Ma) Karoo sequence, composed mainly of interbedded shale and sandstone layers, only a few hundred meters thick (Ward et al., 2004). Since the Vredefort impact, the Witwatersrand Basin has been tectonically inactive, and subjected to extensive erosion that is estimated to between 5 – 10 km (McCarthy et al., 1990).

The TauTona mine is located on the northern margin of the Witwatersrand Basin (Fig. 1.1) where the metamorphosed sedimentary rocks of the West and Central Rand Group are tilted 20° - 25° to the SSE. The mining horizons in the TauTona mine, are in the Carbon Leader Reef, at a depth of 3.6 km and are overlapped by the Mponeng mine that is active in the Ventersdorp Contact Reef about 800 m above the TauTona mine (Fig. 2.1). The mining horizons, in general, follow the bedding horizons leaving unmined areas (pillars in Fig. 2.1) for support. The NELSAM site is located on the south side of the

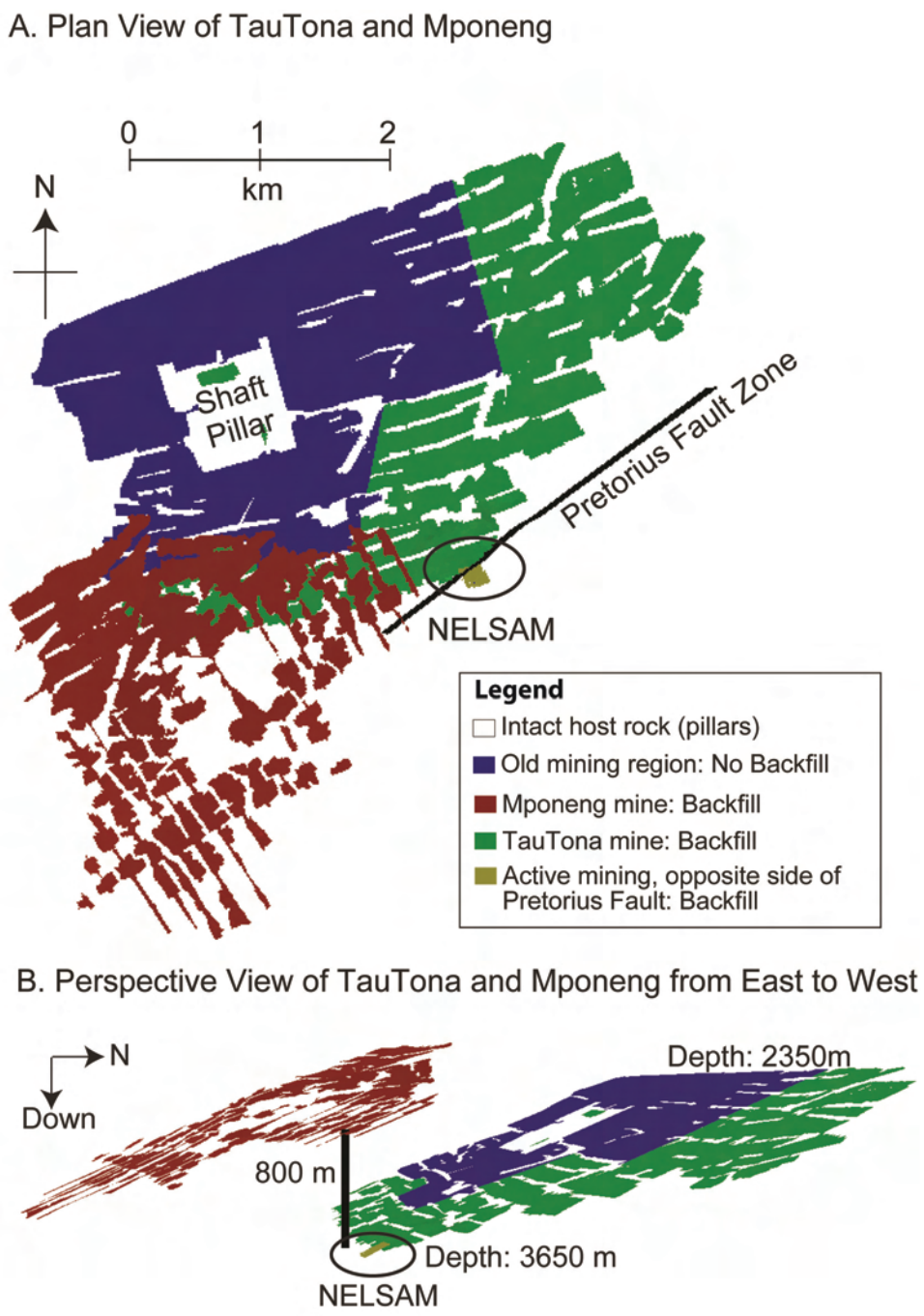

Figure 2.1: Layout of the TauTona mine, South Africa. (A) Plan view of the mining at Mponeng mine (red) and TauTona mine (blue, green and yellow) and the Pretorius fault (black). The white area represents intact rock, the colored regions indicate areas that have been mined. The NELSAM research site is in the south eastern part of TauTona mine. (B) Perspective view of the mining reef from the east without the Pretorius fault. The NELSAM site is located in the deepest part of TauTona mine. Mponeng is about 800 m shallower than TauTona mine.

TauTona mine, where the mining horizon is displaced vertically ~30 m by the Pretorius fault (Fig. 2.2). Most of the area north of the fault was mined in the long-wall method (Brady and Brown, 1993) with backfill for support (Grice, 1998). The unmined areas south of the Pretorius fault are future reserves to be mined down to depth of more than 4 km. Fig. 2.3 is a map view of the tunnel layout within the NELSAM area illustrating tunnels at all levels projected on top of each other on a horizontal map view. The red tunnels are of level 118 (11,800 ft depth), the blue tunnels are of level 120 (12,000 ft depth). The mined area, referred to as "reef", follows an inclined surface that dips to the SSE (gray in Fig. 2.3). Finally, a map view of the dikes and the trace of the Pretorius fault at reef elevation are projected on top. The mining reef is displaced by the Pretorius fault-zone, which is traced in red.

STRUCTURE OF THE PRETORIUS FAULT

Large scale features

The Pretorius fault is about 10 km long, trends in ENE direction, forms a sub-vertical fault-zone that extends from about 1 km to at least 5 km below the surface and exposed in TauTona mine at a depth of 3.6 km and Mponeng mine, at depth of 2.8 km (Gibson et al., 2000a). Underground mapping suggest that the fault is an oblique right-lateral fault with horizontal displacement of about 200 m and vertical displacement, south side thrown up, up to 100 m (Kershaw, personal communication, 2005) and up to 30 m at the NELSAM site. In TauTona mine, the Pretorius fault crosscuts quartzitic rocks of the Lower Johannesburg Subgroup of the Lower Central Rand Group (Frimmel and Minter, 2002), a range of light gray to dark gray, fine to very coarse grained quartzite. In the NELSAM site a mafic dike, referred to as the Swannie dike, with a thickness up to 60 m, is exposed

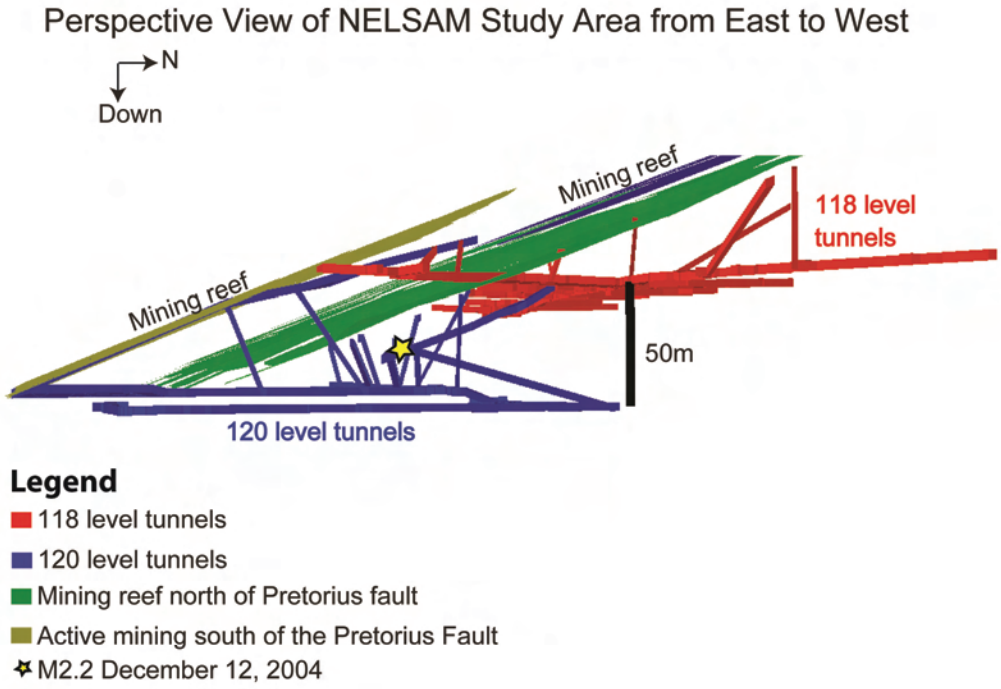

Figure 2.2: Perspective view of the NELSAM area. The active mining (yellow) is offset by the older mining (green) by ~30 m throw along the Pretorius fault. The level 118 (red) and level 120 (blue) tunnels are separated by 50 m. The M2.2 rupture of December 12, 2004 (yellow star) is located ~20 m below the mining reef.

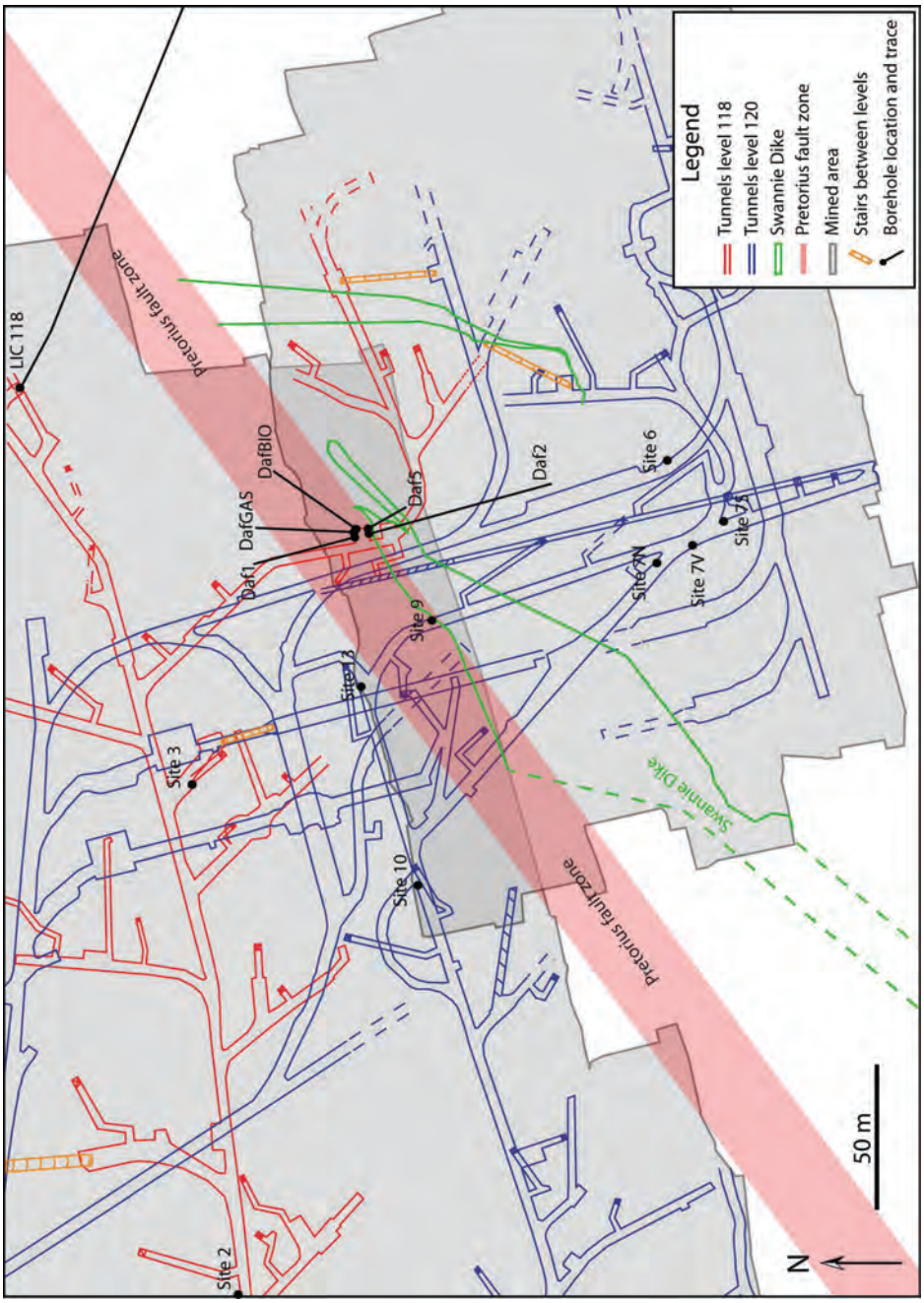

Figure 2.3: Map view of the NELSAM area, TauTona mine, South Africa. Tunnels of level 118 (red) and level 120 (blue) are projected on top of each other. The currently mined area dips 20-25° to the SSE and is offset by the Pretorius fault. The borehole locations at different NELSAM sites are illustrated. Site 2 and 3 are vertical boreholes at level 118, site 6, 7V, 9, 10 and 13 are vertical boreholes at level 120. Daf1, Daf2, DafGAS, DafBIO and Daf5 are inclined boreholes, drilled at level 118. LIC118 is a sub-horizontal borehole, drilled at level 118, which continues far away from active mining activities.

along the south side of the fault-zone. In the Mponeng mine, the Pretorius fault crosscuts quartzitic rocks from the Venterspost Formation at the bottom of the Ventersdorp Supergroup, overlain by metabasalt of the Klipriviersberg Group (Frimmel and Minter, 2002).

Small scale features

The Pretorius fault-zone is a complex structure with tens of fault segments that form a 25 – 35 m wide, sub-vertical zone. The segments form an anastomosing network of dominantly east-west striking, steeply dipping (40°-90°), quasi-planar faults that crosscut and intersect each other. The majority of these segments contain a quartzitic cataclastic fault rock that varies in thicknesses from a few millimeters up to tens of centimeters.

Mapping of the exposed structure of the Pretorius fault was conducted in seven tunnels that cut through the fault at depth of 3.5 - 3.6 km in TauTona mine. The height and width of most of the tunnels is about 3 x 3 m and the tunnels are mostly horizontal or inclined about 20°, parallel to the bedding. The tunnels were mapped at a scale of 1:100 and 1:50, accompanied by local mapping at a scale of 1:10. Mapping methods include the generation of tunnels maps (Fig. 2.4 and 2.5) in which 3D structures, mapped in the roof and both sidewalls, are represented with the sidewalls unfolded to be parallel to the roof. A mapping grid was used by marking the tunnel sidewall every 4 m. The 1:10 maps were made by using an aluminum frame with a 10x10 cm wired grid.

The complexity of the intersecting fault segments of the Pretorius fault-zone is presented in tunnel maps [three north-south trending tunnels that cross the fault-zone (Fig. 2.4) and three oblique tunnels within the fault-zone (Fig. 2.5)]. The tunnels are labeled according to their depth and their function with regard to the mining operations.

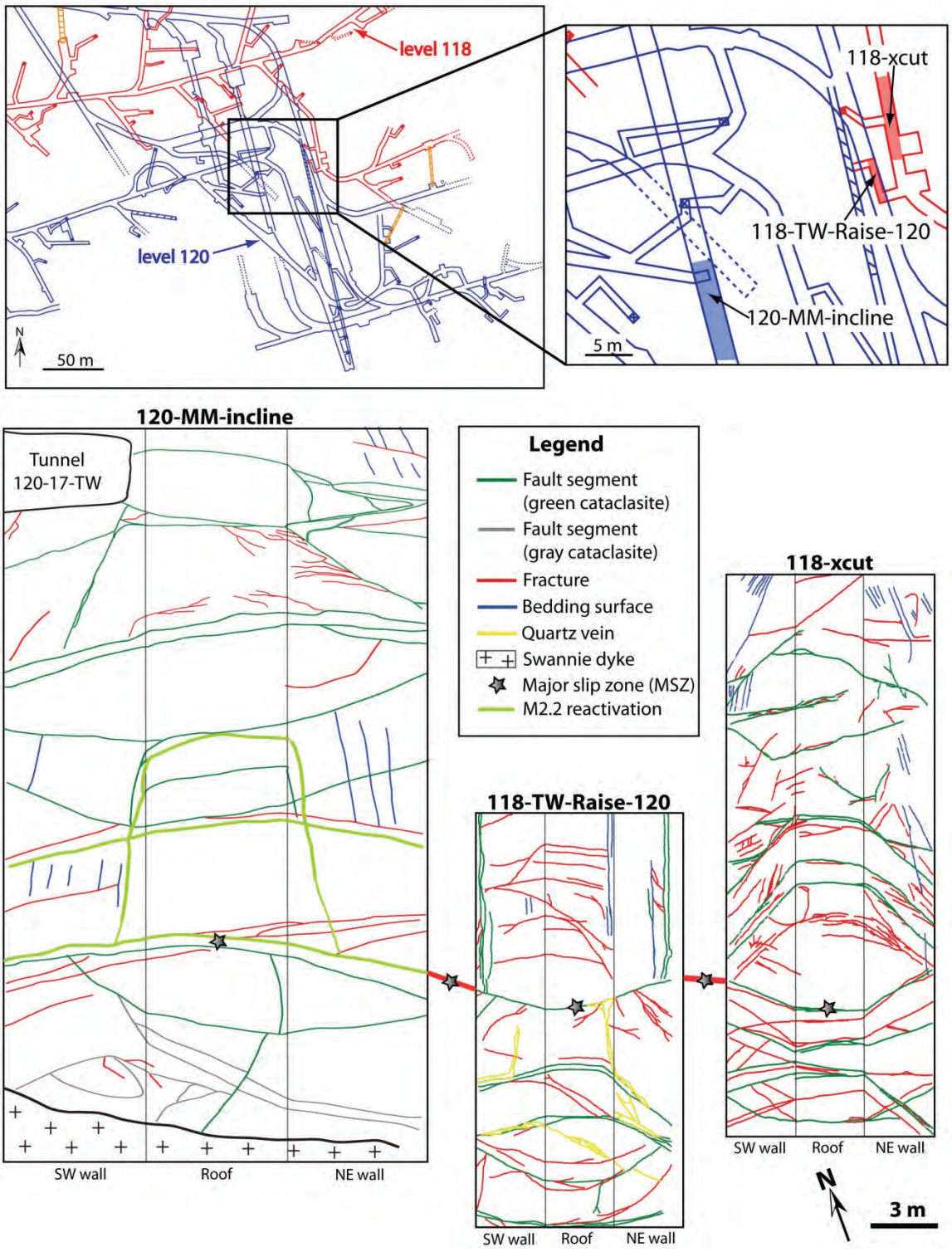
level 118
level 120
N
50 m
118-xcut
118-TW-Raise-120
120-MM-incline
5 m
120-MM-incline
Tunnel
120-17-TW
SW wall
Roof
NE wall
Legend
Fault segment
(green cataclasite)
Fault segment
(gray cataclasite)
Fracture
Bedding surface
Quartz vein
Swannie dyke
Major slip zone (MSZ)
M2.2 reactivation
118-TW-Raise-120
SW wall
Roof
NE wall
118-xcut
SW wall
Roof
NE wall
N
3 m

Figure 2.4: Structural tunnel maps of the Pretorius fault. The tunnel maps are generated by mapping the 3D structures in the roof and sidewalls of the tunnels, presented with the sidewalls unfolded parallel to be parallel to the roof. The 120-MM-incline is inclined ~20° to the S, 5 m wide and 5 m high and mapped at a scale of 1:100. The 118-TW-Raise-120 is inclined ~20° to the N, the 118-xcut tunnel is horizontal. Both are 3 m wide and 3 m high, and mapped at a scale of 1:50. Cataclasite bearing fault segments are illustrated in green and gray, fractures in red, bedding surfaces in blue and quartz veins in yellow. The main fault segment of the Pretorius fault (see text for explanation) is linked between the 3 tunnel maps. The segments that are reactivated by the M2.2 of December 12, 2004 are illustrated in light green.

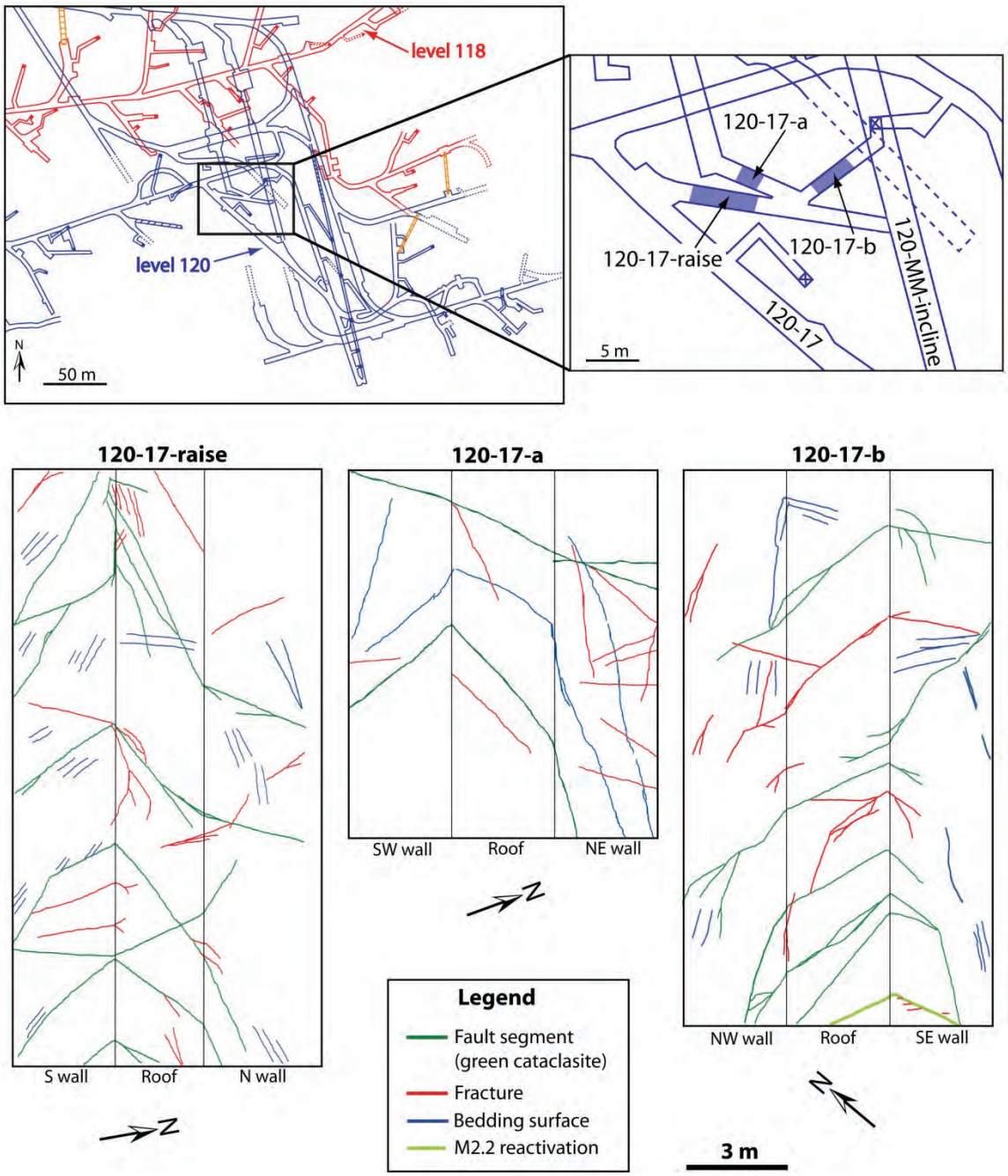

Figure 2.5: Structural tunnel maps of the Pretorius fault (see text for explanation). The 120-17-raise tunnel dips ~25° to the E, the 120-17-a and 120-17-b tunnels are horizontal. All three tunnels are 3 m high and 3 m wide and mapped at a scale of 1:50. Cataclasite bearing fault segments are illustrated in green, fractures in red and bedding surfaces in blue. The segment that is reactivated by the M2.2 of December 12, 2004 is illustrated in light green.

For example, tunnel 120-MM-incline (Fig. 2.4) represents an inclined tunnel at depth of 12,000 ft, designed for the new shaft that will transport men and material. In Fig. 2.4, the 120-MM-incline tunnel dips about 10° S, the 118-TW-Raise-120 dips about 25° S, parallel to the bedding, and the 118-xcut is a horizontal tunnel. In Fig. 2.5, the 120-17-raise tunnel dips ~25° to the E, the 120-17-a and 120-17-b tunnels are horizontal.

Three main types of structures in the Pretorius fault-zone were indentified; cataclasite-bearing segments, fault-associated fractures and bedding surfaces. Fault-associated fractures were distinguished from fractures related to the tunnel geometry or blasting, by their continuation throughout the tunnel. Many of the individual segments in the 25-35 m wide Pretorius fault-zone contain green to gray cataclastic rock that is described below. The width of the cataclasite in the individual segments varies significantly from a few mm to a few tens of cm over a distance. along the strike of the segments, of just a few m or less (Fig. 2.6). Fig. 2.6a illustrates two steep fault segments that dip in opposite direction (S1 and S2) together with a third segment that is parallel to the bedding (S3). The cataclasite in these three segments is only a few mm thick. An injection vein up to 15 cm thick is injected from the bedding-parallel segment into the quartzite (Fig 2.7b). Fig. 2.6c and d illustrate thickness variations of the cataclasite along strike of the fault segment; from 1-2 cm at A to 11-18 cm at B. The thick zone of cataclasite is composed of sub-rounded quartz grains up to 12 cm in diameter (C in Fig. 2.6c). Intense variations in thickness of the cataclasite suggest mobilization of the incohesive gouge during the formation of the Pretorius fault, into local zones of relatively low fault-normal effective stress.

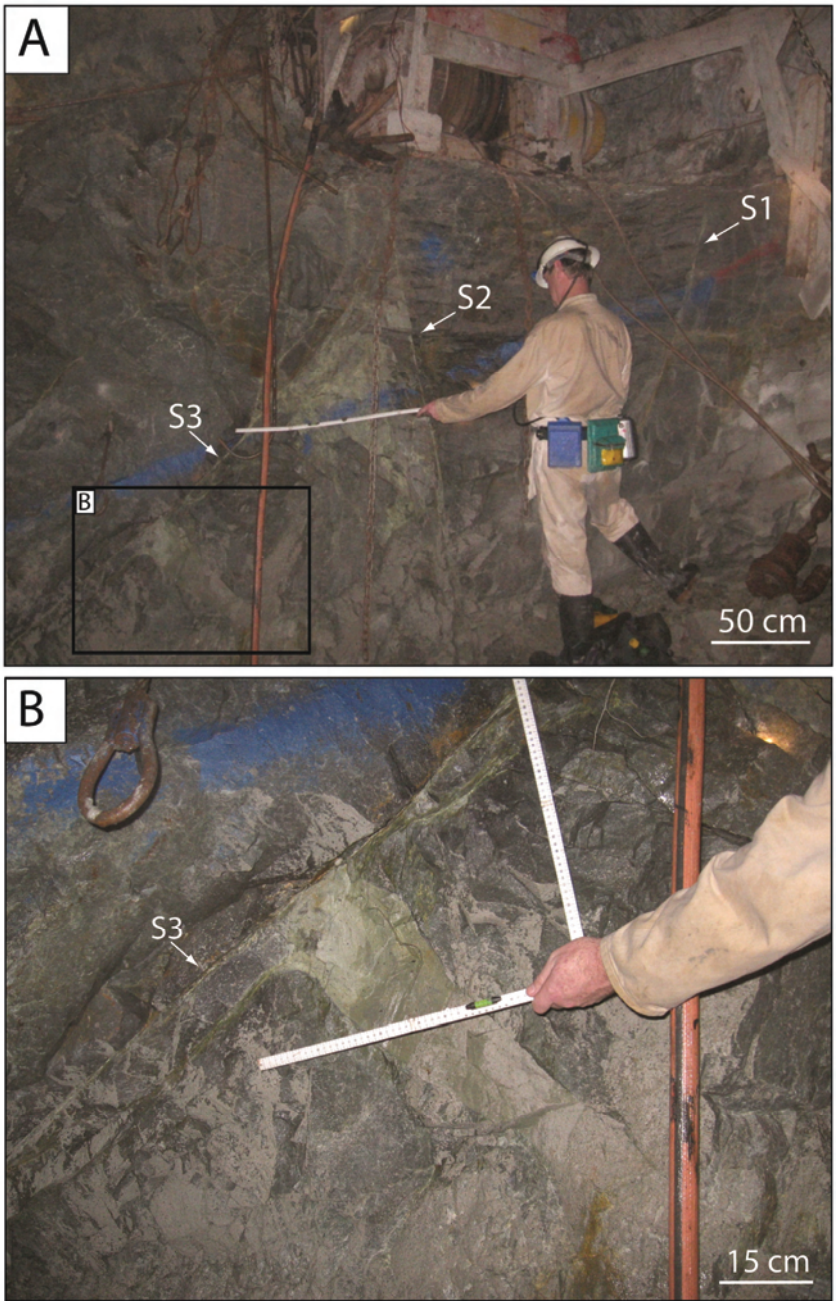
A
S1
S2
S3
B
50 cm
B
S3
15 cm

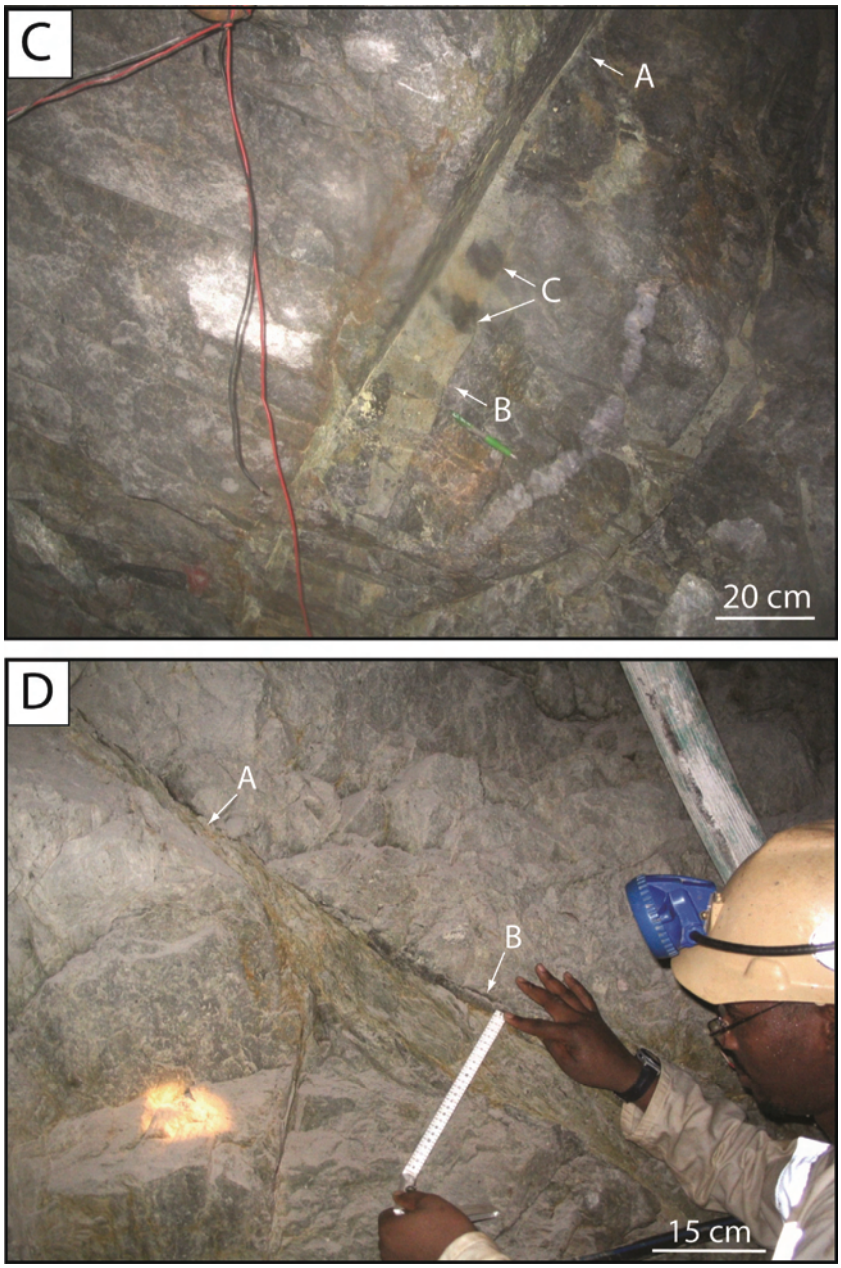

Figure 2.6: Characteristic fault segments in the NELSAM area. (A) Two steep fault segments with cataclastic zone up to only a few mm, both dipping in opposite direction (S1 and S2), and a bedding-parallel fault segments (S3). (B) An injection vein up to 15 cm thick injected into the quartzite, from the S3 fault segment, with a cataclastic zone of just a few mm. Location is at the SW-wall of 120-MM-incline, at the intersection with the 120-17-TW (see Fig. 2.5). (C) Thickness variation of the cataclasite zone, from q cm at A to 18 cm at B. The cataclasite displays quartz clasts up to 12 cm in diameter at C. Location is at the NE-wall of 118-xcut (D) Thickness variations of the cataclasite zone from 2 cm at A to 11 cm at B. Location is at the NE-wall of 118-xcut.

The tunnel maps (Fig. 2.4 and 2.5) illustrate the individual segments that contain cataclasite in green, fault-zone associated fractures in red and bedding surfaces in blue. The maps dominantly show steeply, north and south dipping segments with minor bedding parallel fault segments. The color of the cataclasite changes from green to gray towards the Swannie dike that bounds the Pretorius fault-zone on the south (see Fig. 2.4 120-MM-incline tunnel). Crosscutting relationships with offset between individual fault segments were not observed. Dominantly south dipping fault segments with abundant bedding surfaces are observed within the three tunnels (Fig. 2.5), most of which are on the northern side of the Pretorius fault-zone.

Fault segments within the 118-xcut tunnel (Fig. 2.4) contain two dominant orientation groups; south and north dipping segments with mean values of 69°/170° ± 17° (T1 in Fig. 2.7) and 72°/346° ± 9° (T2 in Fig. 2.7). The angle between these two groups is 39°, suggesting that they are conjugate sets. However, evidence for slip along any of these segments was not found.

A distinct structural difference between the north and the south side of the Pretorius fault-zone exists (Fig. 2.4). Within the north side of the fault-zone, bedding surfaces are abundant and the quartzitic host rock is light gray. On the south side, no bedding surfaces are observed and the density of cataclasite-bearing segments significantly increases. Occasionally quartz veins (yellow in Fig. 2.4) are observed within the south section of the fault-zone. The quartzitic host rock on the south side of the fault is dark gray, most likely representing up-thrown quartzites from lower stratigraphic horizons (Rob Barnett, personal communication, 2007).

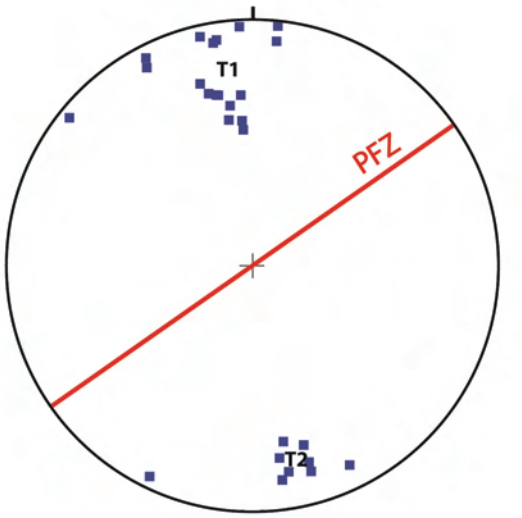

Figure 2.7: Stereographic projection of poles of fault segments mapped within the 118-xcut tunnel. Two groups of fault segments are recognized, with mean values of T1 69°/170° ± 17° and T2 72°/346° ± 9°.

This structural transition between the north and south side of the Pretorius fault-zone occurs along a dominant fault segment (Fig. 2.4). It is believed that most of the ancient slip of the Pretorius fault was localized along this segment, referred to as the "main slip zone" (MSZ). This zone is best characterized in the 120-MM-incline tunnel (Figs. 2.4 and 2.8) where its characteristics are:

1) Sub-vertical segment, dipping 81° to the south, with a dark green cataclasite zone of 30 – 50 cm thick (Fig. 2.8).
2) Structural transition, with abundant bedding surfaces and light gray quartzitic host rock north of the MSZ, and higher density of cataclasite-bearing fault segments, lack of bedding surfaces and dark gray quartzitic host rock south of the MSZ (Fig. 2.4).
3) Light green – yellow cataclasite distributed dominantly at the edge of the MSZ, during ancient reactivation of the MSZ (Fig. 2.8 and text below).
4) Recent reactivation during the M2.2 event on December 12, 2004, characterized by white fresh rock powder that dominates along the contact between the cataclasite and quartzite (Fig. 2.8 and Ch.3).

Similar characteristics along one segment are observed in the 118-TW-Raise-120 and 118-xcut tunnels, with the addition of quartz veins, observed on the south side of this segment (Fig. 2.4). The cataclastic zone for these dominant segments is up to 30 cm thick, and bedding-parallel injection are observed from this segment (118-TW-Raise-120 Fig. 2.4), with the injected material being up to 20 cm thick and continuous for several meters. Based on these observations, these segments are interpreted to link to the MSZ in

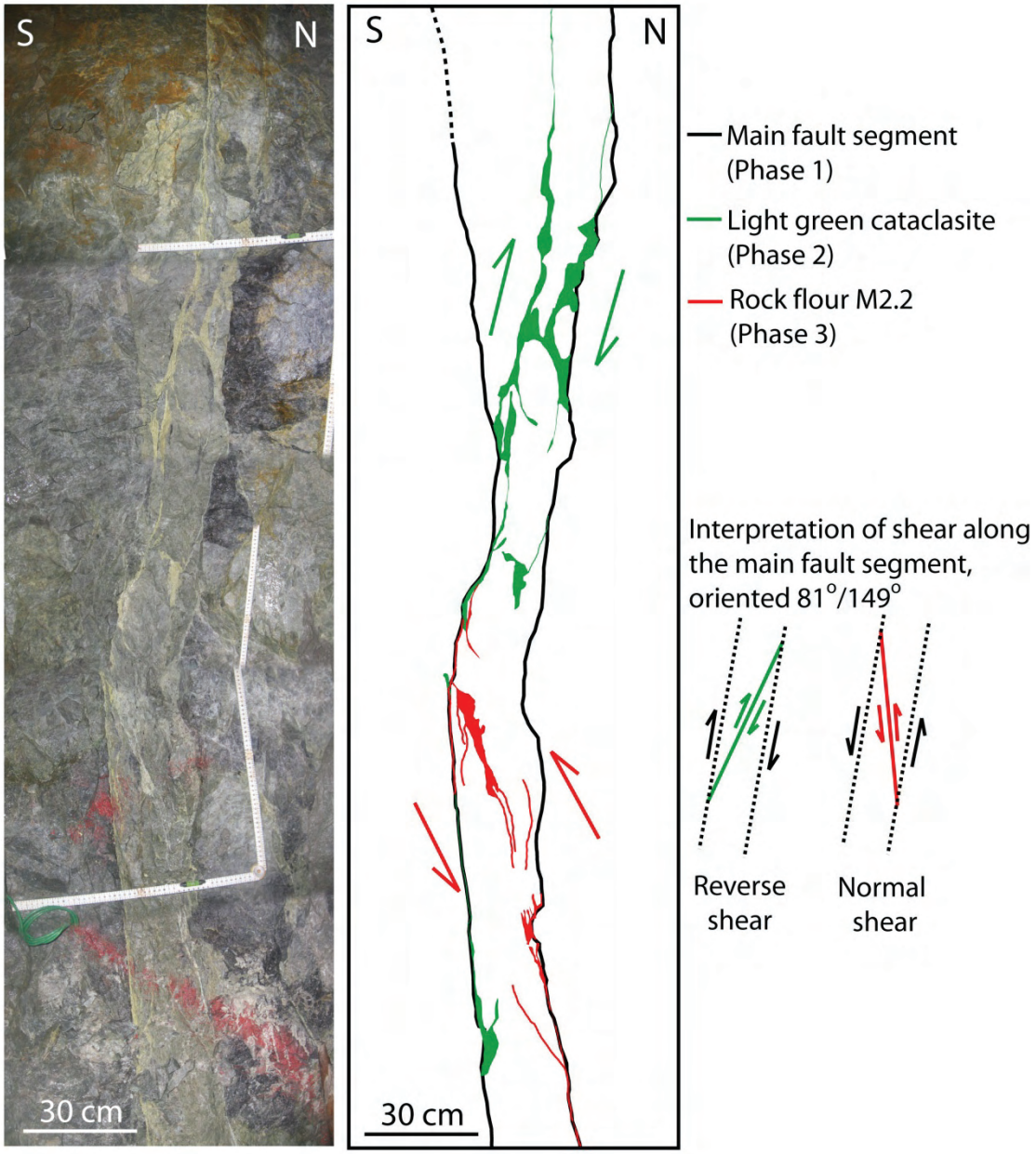

Figure 2.8: The main slip zone of the Pretorius fault, at the SW-wall of the 120-MM-incline. Three phases of activity are recognized; Phase 1 generated the dark green cataclasite during the formation of the Pretorius fault; Phase 2 generated the light green cataclasite that cuts the cataclasite of the first phase following right-lateral Riedel shear structures, indicating reverse shear along the main fault segments; Phase 3 generated fresh rock flour during the M2.2 event that reactivation of the main fault segment. The reactivation cuts the cataclasite following left-lateral Riedel shear structures, indicating normal shear along the main fault segment.

the 120-MM-incline (Fig. 2.4), indicating alternating N and S dips of this overall steep segment.

Two sets of slickenside striations were observed in several segments of the Pretorius fault. The most dominant and best developed set indicates a sub-horizontal right-lateral strike slip motion. This slickenside set likely corresponds with the initiation of the Pretorius fault. A second slickenside set forms a poorly developed, sub-vertical group of slickensides. The existence of two distinct sets of slickensides suggests that the total oblique right lateral slip along the Pretorius fault is composed of either two separate slip phases or slip-partitioning between lateral and vertical motion.

Ancient fault reactivation

Certain segments of the Pretorius fault display evidence of multiple slip events that occurred along the same fault segment. The MSZ of the fault-zone displays two stages of cataclasite development (Fig. 2.8) based on their color difference. One group is a dark green cataclasite, interpreted to belong to the early phase. A second group is the lighter green cataclasite, interpreted as the second phase, which concentrates along the edges of the dark green cataclasite and cuts the cataclasite of the first phase in Fig. 2.8. Following the geometrical relation of Riedel shear structures with respect to the main shear zone, discussed by Katz et al. (2004), the lighter green cataclasite is interpreted to have been developed during a right lateral shear, as the south block of the fault moved up with respect to the north block. The orientation of the MSZ (81°/149°) along with Riedel fractures suggest a reverse shear along this segment. The south side moved up, during the second phase (Fig. 2.8). Gibson et al. (2000a) suggested that the Pretorius fault was reactivated by gravitational collapse and extension during the Platberg rifting and / or the

Vredefort impact. The reactivation in Fig. 2.8 could be the result of one of these events. Recent reactivation event along the MSZ, associated with the M2.2 event of December 12, 2004, is described in details in Ch. 3.

Fractures in the Pretorius fault

The fractures in the Pretorius fault were analyzed in image logs in 11 boreholes drilled at the NELSAM site (Reches, 2006). The boreholes were logged with a slim borehole Digital Optical Televiewer (DOPTV) made by Robertson Geologging, UK. Eight of the boreholes are 10 m deep, located within, or close to, the Pretorius fault-zone (borehole locations Fig. 2.3). Six of the boreholes are vertical (site 2, 3, 7V, 9, 10 and 13) and two are inclined 45° to azimuths 152° (site 7N) and 323° (site 7S), all 75 mm in diameter. Three holes, Daf2, Daf5 and DafBio, are 20 - 50 m deep, drilled at 20° and sub-parallel to bedding, at azimuths of 165°, 150° and 36° respectively, 96 mm in diameter, and cross the Pretorius fault-zone. The boreholes are drilled from TauTona mine tunnels at levels 120 and 118. Some of these boreholes are used to install NELSAM instrumentation. The different inclinations and range of azimuths of the boreholes probably eliminated a bias in fracture orientation sampling.

The Digital Optical Televiewer records an oriented image of the borehole wall with a radial resolution of 720 pixels / 360° and a vertical resolution up to 1 mm. Borehole features were identified with RG-DIP interpretation software version V6.2 provided by Robertson Geologging, UK (http://www.geologging.com). The software was used to calculate the true fracture orientations, corrected for the borehole orientation and magnetic declination. The overall quality of the images is good to excellent, with the

exception of Daf2, DafBio and hole 13, which are of poor quality due to logistical problems with the power supply.

Results

Three types of features mapped in the borehole images are; bedding, continuous fractures that can be traced with a complete sine curve and discontinuous fractures that can only be traced by parts of a sine curve (Fig. 2.9). Bedding-parallel fractures are distinguished from bedding surfaces by the presence of an apparent roughness, where contacts between bedding surfaces appear as smooth, dark gray features (Fig. 2.9). A cataclasite layer along the fracture could be recognized in some cases.

There exists a synthesis of orientations for continuous and discontinuous fractures and bedding surfaces in all 11 boreholes. The discontinuous fracture orientations are more scattered but they belong to the same fracture population as do the continuous fractures (Fig. 2.10a and 2.10b). Density contours on the continuous fracture dataset indicate three dominant sets of fractures, marked group A, B and C in Fig. 2.10c. These fracture groups are oriented 66°/139° ± 12°, 30°/169° ± 14°, and 09°/087° ± 12° respectively. Fracture set B is interpreted as bedding-parallel fractures, as bedding surfaces from all 11 boreholes (Fig. 2.10d) have an average orientation of 28°/171° ± 12°.

The fracture orientations for each borehole are shown separately and grouped according to the location with respect to the fault-zone (Fig. 2.11); including the number of fractures per drilling length, f, and the distance of the borehole from the fault-zone, d. The borehole map locations in relation to the Pretorius fault are illustrated in Fig. 2.3. Boreholes north of the fault-zone (Fig. 2.11a) display dominant development of the bedding-parallel fracture set B. This set is poorly developed south of the fault zone

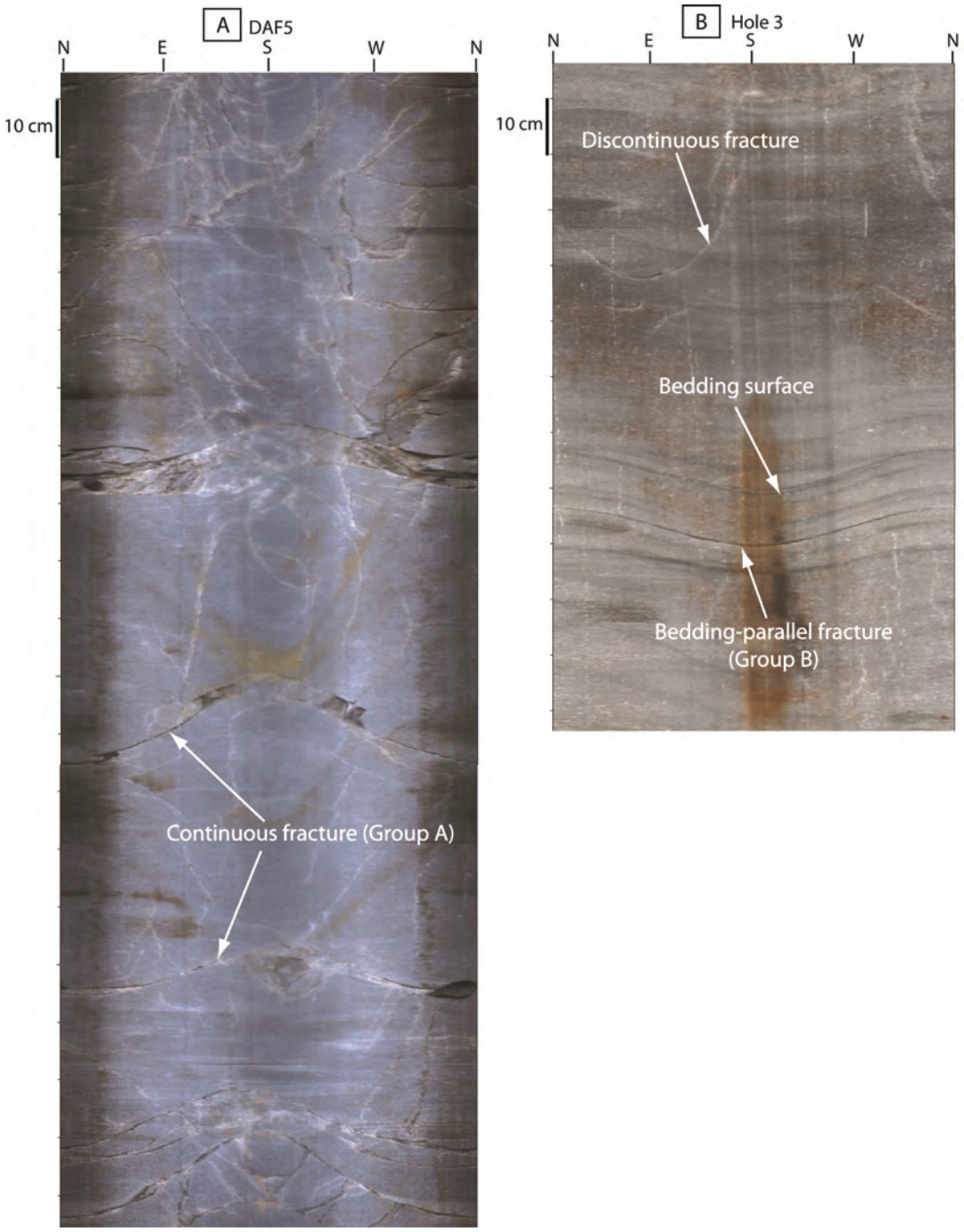

Figure 2.9: Borehole image logs of DAF5 (A) and Hole 3 (B). (A) The image log of DAF5 displays high fracture density with dominant development of fractures belonging to set A. The borehole is inclined 20°, sub-parallel to bedding, towards azimuth 150°. (B) Image log of Hole 3 displays clear bedding surfaces as smooth dark curves, while continuous fractures developed parallel to the bedding, recognized by an apparent roughness. Discontinuous fractures are defined by partial sine-curves.

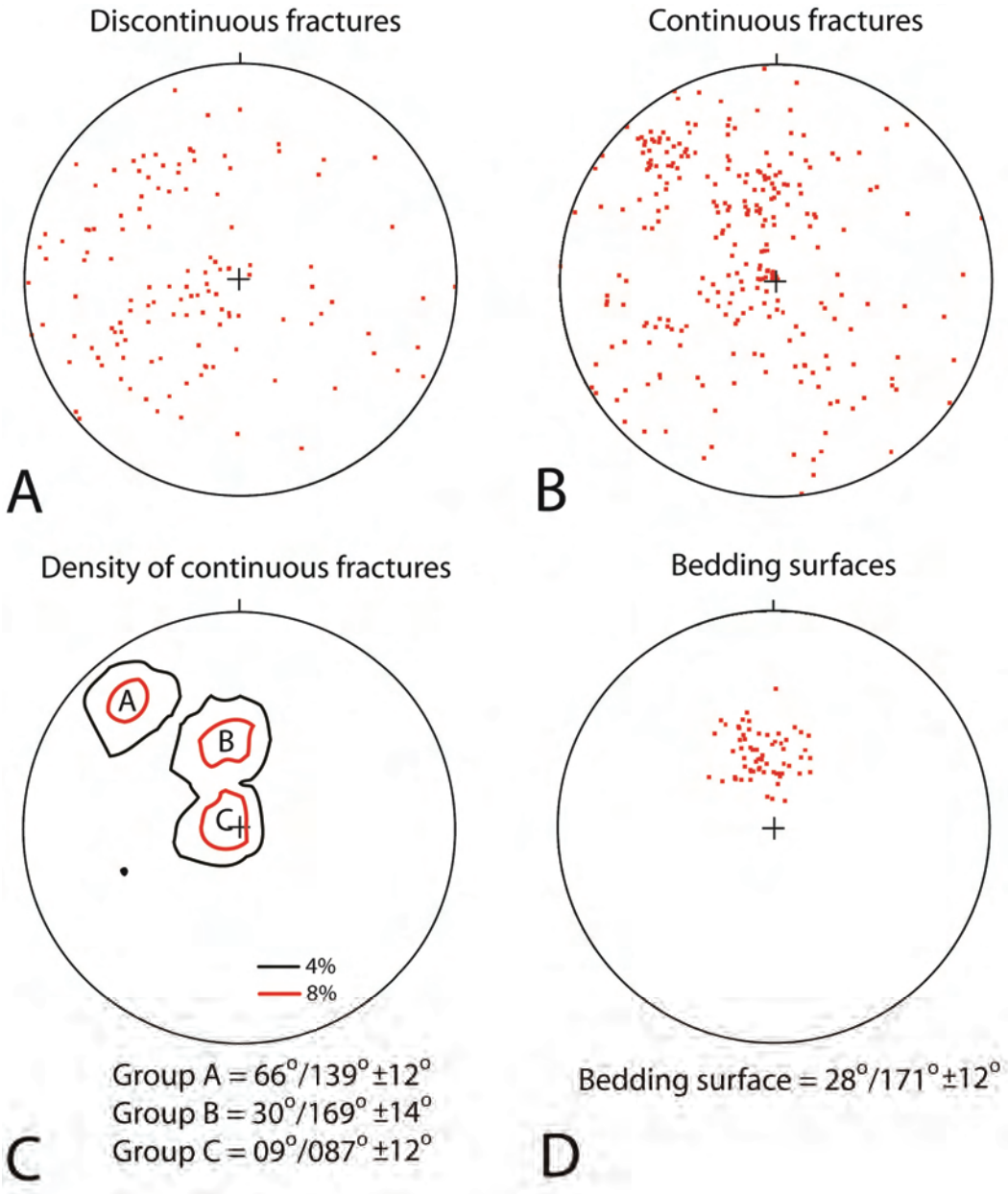

Figure 2.10: Stereographic projection of fractures and bedding surfaces from image logs of 11 boreholes within the NELSAM area. (A) Orientations of discontinuous fractures. (B) Orientations of continuous fractures, suggesting that the discontinuous fractures belong to the same fracture set as the continuous fractures. (C) Density contours of all continuous fractures display 3 fracture sets A, B, and C. (D) Orientations of bedding surfaces display mean orientation that indicates that fracture set B is parallel to the bedding.

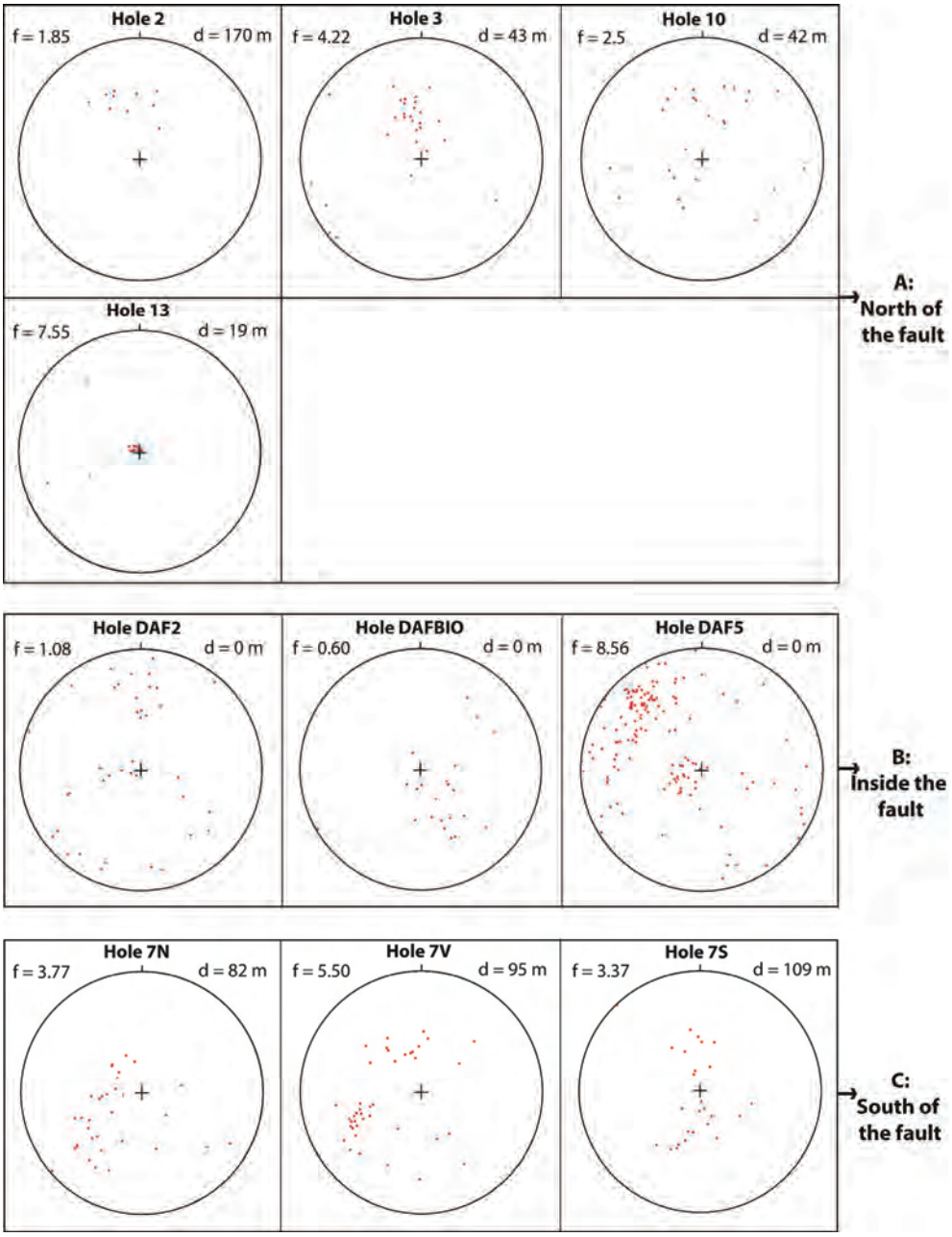

Figure 2.11: Stereographic projection of the fractures for each individual borehole. The number of fractures per drilling length, f, and the distance to the borehole from the center of the Pretorius fault, d, are displayed for each plot. (A) Fracture orientations on the north side of the Pretorius fault (Hole 2, 3, 10 and 13) display dominantly set B. (B) Fracture orientations within the fault-zone (Hole DAF2, DAFBIO and DAF5). DAF2 and DAFBIO are not representable due to poor quality. DAF5 displays high fracture density of dominantly fracture set A. (C) Fracture orientations south of the fault-zone display scattered fracture orientations with development of fracture set B.

(Fig. 2.11c), and absent in boreholes within the fault-zone (Fig. 2.11b). Fracture set A are dominantly within DAF5, inside the fault-zone but are not observed outside of DAF 5. Fractures of set C is only present in boreholes DAF 5 and hole 13. The data quality of image logs DAF2 and DAFBIO is poor, therefore the fracture density and orientations for these image logs are not represented.

In summary, three fracture sets characterize the NELSAM research area. Within the fault-zone the fracture density is high and characterized by fracture set A. The bedding-parallel set B occurs mainly outside and dominantly north of the Pretorius fault, where no other fracture sets are present. Fracture set C occurs both inside and outside the fault-zone. Our interpretation of the origin of the three fracture sets is discussed below.

THE FAULT ROCK

Many of the segments in the Pretorius fault-zone contain a highly cohesive cataclasite (Figs. 2.7 and 2.8) that is distributed along fault segments in planar zones with sharp, planar contacts within the host rock. The thicknesses of the zones range from a few mm to tens of cm and vary significantly along the strike of individual segments (Fig. 2.6c and 2.6d). Abundant injection veins can be observed, ranging in thickness from a few cm to tens of cm thick. The majority of the injection veins are injected sub-perpendicular to fault segments (Figs. 2.7b and 2.12). Fig. 2.12 represents a detailed map (scale 1:10) of an injection vein on the south side of the fault-zone. The injection has a maximum thickness of ~15 cm and originated from a fault segment only ~10 mm thick. Several large injection veins with thicknesses up to tens of cm have been injected along bedding surfaces. An example of this appears on the north side of the fault-zone (Fig. 2.4, tunnel

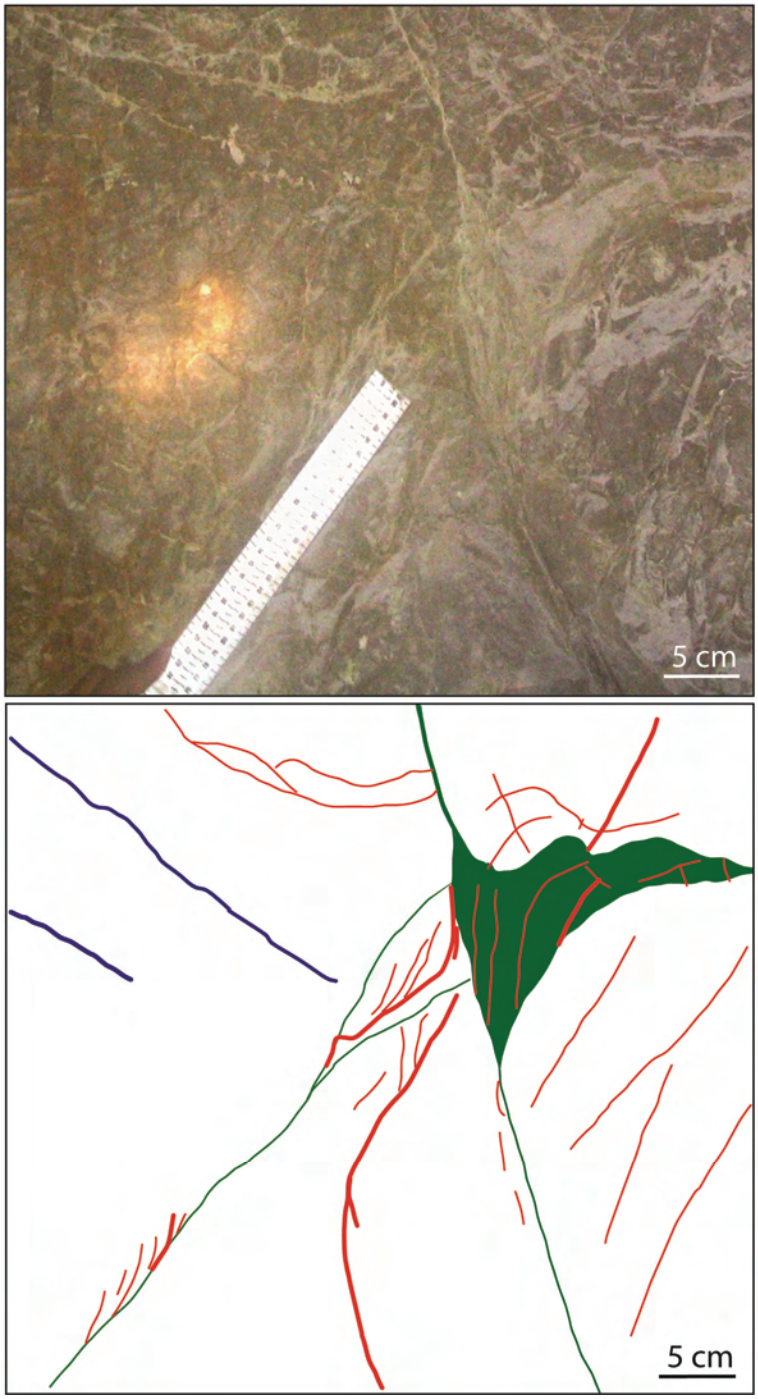

Figure 2.12: Detailed map, mapped at a scale 1:10 of an injection vein on the NE-wall of the 118-xcut tunnel. The cataclasite is illustrated in green, fractures in red, bedding surfaces in bleu. The vein with a thickness of ~15 cm was injected from a fault segment with a cataclasite zone of only 1 cm thick.

118-TW-Raise-120). These bedding parallel injection veins are abundant and laterally continuous for several meters, suggesting macroscopic flow of the cataclasite.

During the mapping three different types of cataclasite, each with distinct color, were recognized: (1) a dark green cataclasite, (2) a light green-yellow cataclasite and (3) a gray cataclasite, found in the vicinity of the Swannie dike on the south side of the Pretorius fault-zone (Figs. 2.4 and 2.5). The micro-structural features of the cataclasite were examined in thin sections and SEM images (Zechmeister et al., 2005). It was found that the dark green cataclasite is predominantly composed of ultra-fine grained matrix of quartz, mica, and opaque minerals and abundant angular to rounded clasts of quartz (Fig. 2.13). The clasts range from less than mm to tens of cm. An anastomosing cleavage is rarely developed within the matrix, surrounding the clasts (Fig. 2.13b). Some quartz clasts are dynamically re-crystallized (see clasts P and D in Fig. 2.13c). Microscopic flow structures within the cataclasite include flow banding parallel and close to the fault segment wall, dominantly found within injection veins (Figs 2.14a and 2.14e). Dark bands are composed of high concentrations of mica while lighter bands are composed of predominantly quartz and brown bands due to oxidation (Figs. 2.14c and 2.14d). SEM images of the dark green cataclasite display significant small grains within the cataclasite down to nano-scale, which reveal “hour glass” contacts between quartz grains (Fig. 2.15). This observation suggests sintering at grain contact, under elevated temperature, of a granular material after granulation (Zechmeister et al., 2005). The light green cataclasite is less abundant, generally forms thin zones up to tens of mm thick, along the edge of the dark green cataclasite, and rarely crosscuts (Fig. 2.8). Its general composition is similar, with less abundant and smaller quartz clasts, ranging from less than mm to several cm.

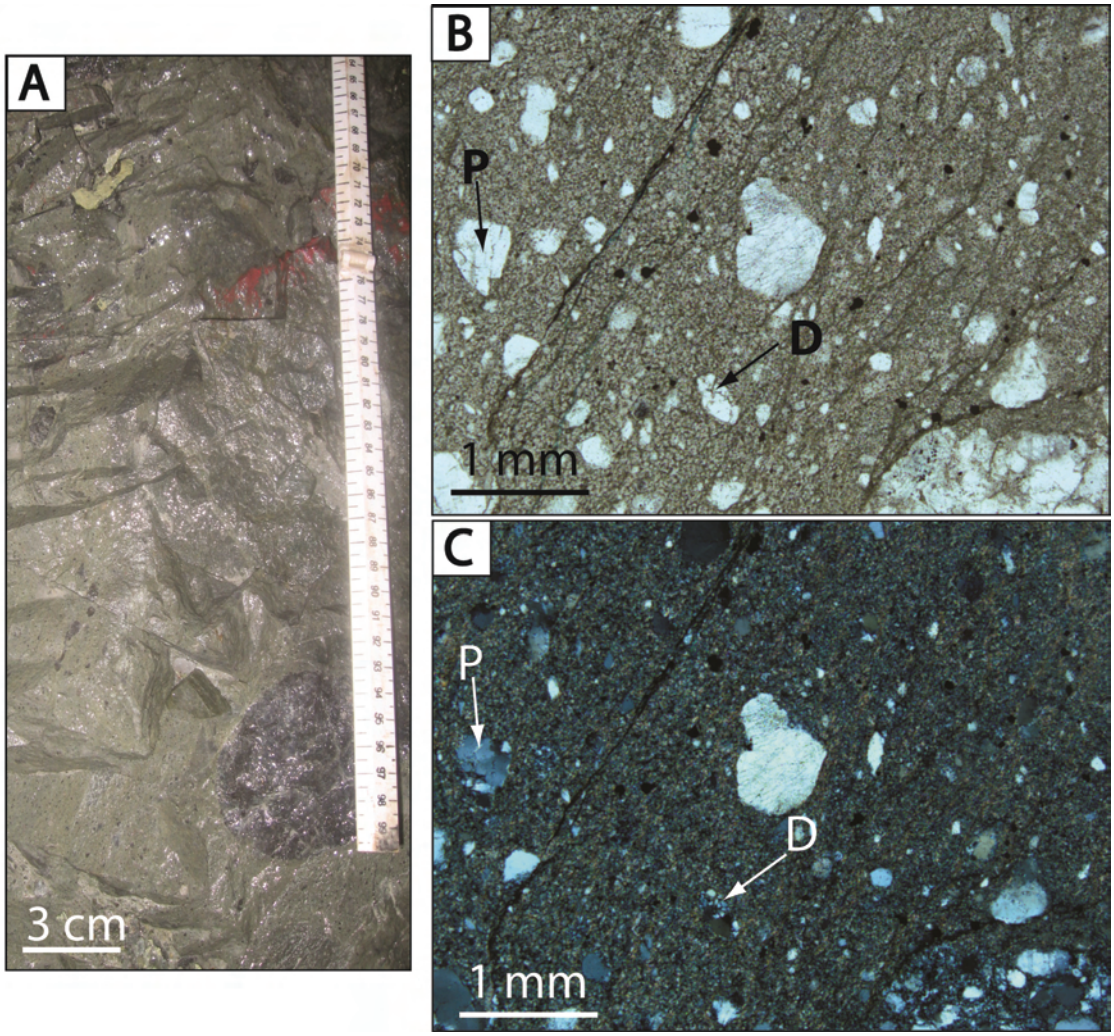

Figure 2.13: Dark green cataclasite of the Pretorius fault. (A) Field appearance displays a wide range in size of quartz clasts that angular to rounded. (B) Thin section (plane polarized) displays ultra-fine grained matrix with anastomosing cleavage around the quartz clasts. (C) Thin section (cross polarized) displays dynamic re-crystallization of several quartz clasts (see P and D).

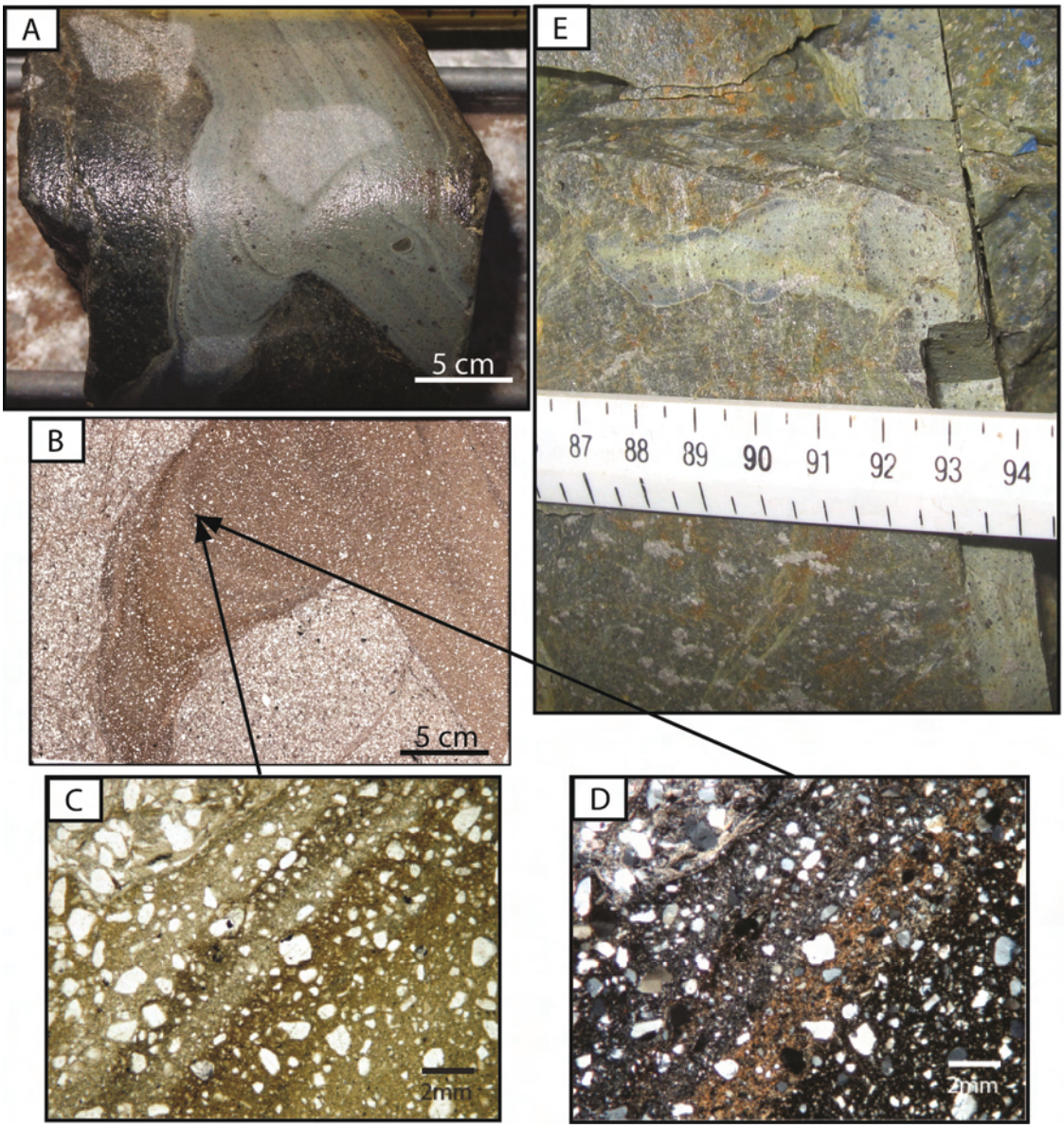

Figure 2.14: Injection veins of the Pretorius fault. (A) Injection vein within a core sample, displays significant flow banding parallel to the fault edge and within the injection vein. (B) Thin section of the injection vein in A. (C and D). Close-up of the injection vein in plane and cross polarized light, display dark bands composed of high concentrations of mica and lighter bands composed of high concentrations of quartz grains. (E) Field example of an injection vein, displaying significant flow banding similar to the core sample (Zechmeister et al., 2005).

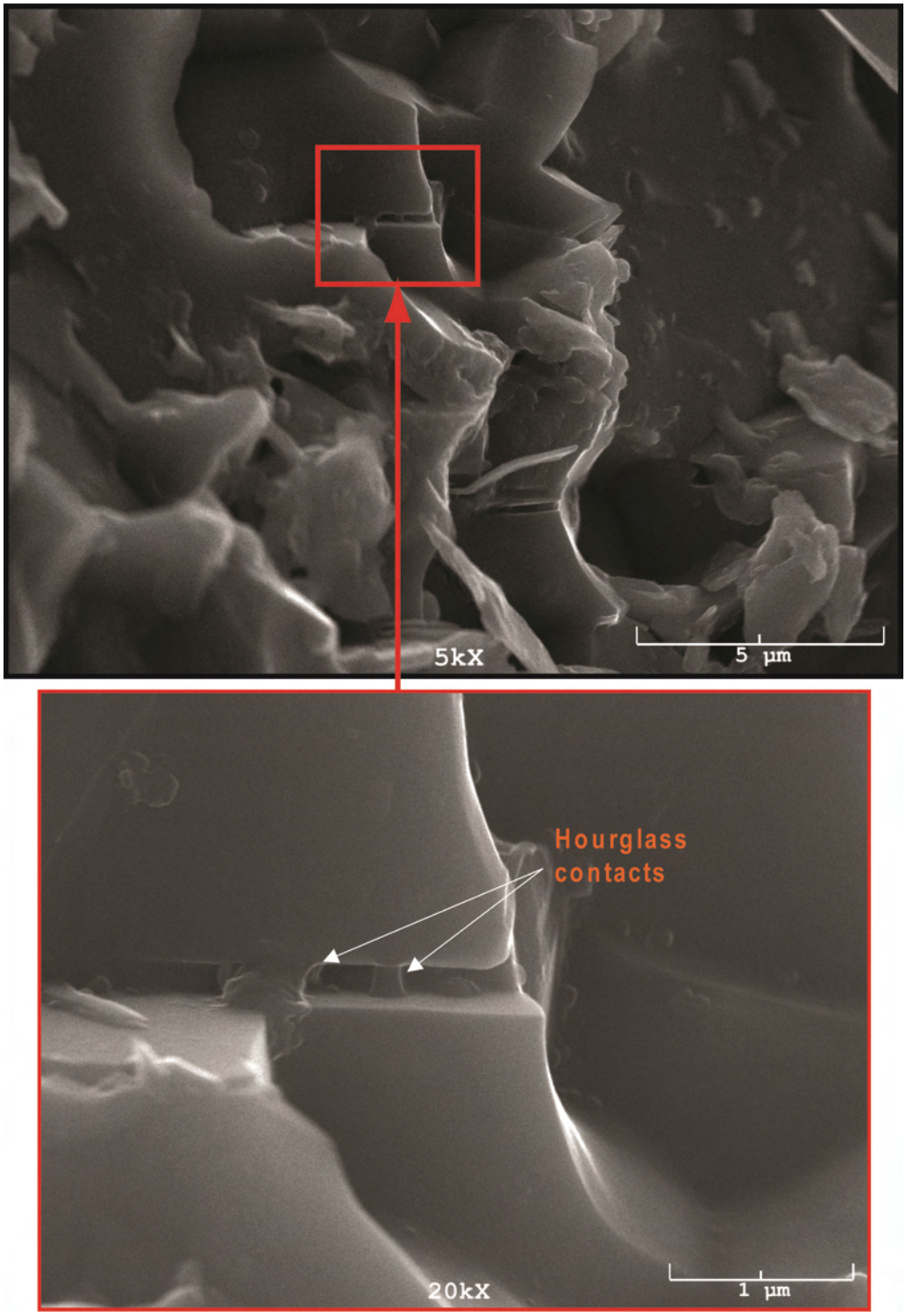

Figure 2.15: SEM image of the cataclasite displays grains down to the nano-scale and hourglass contacts suggestive of sintering of the granular material (Zechmeister et al., 2005).

The gray cataclasite is composed of a gray ultra-fine matrix that is dominantly grain supported (Fig. 2.16). The grains are predominantly quartz with opaque minerals, ranging from 0.005 – 1 mm. A brown oxidation is observed between the grains. The grain size is reduced towards the contact of the cataclasite with the dike. Cathodeluminescence images indicate the development of microlitic textures ('snow flakes') around quartz grains (Figs. 2.16c and 2.16d) (Zechmeister et al., 2005), which is suggestive of a super-cooled melt (Lin, 1994; Swanson and Fenn, 1986).

In summary, the cataclasite of the Pretorius fault-zone consists of gray-green-yellow cataclasite that varies significantly in thickness. Its ultra-fine matrix is poorly sorted, with coarse and angular to rounded clasts. Although rarely a foliation is developed, the cataclasite lacks a shear fabric of the coarse clasts. Abundant flow features on macro- and micro-scale consist of injection veins and flow banding. The gray cataclasite displays rare evidence for the development of melt in the vicinity of the Swannie dike. The origin of the fault rocks is discussed below.

DISCUSSION

STRUCTURAL DEVELOPMENT OF THE PRETORIUS FAULT

The multiple fracture sets, segments and faults in the vicinity of the fault-zone are described above. The origin of fractures and their relations to the fault-zone are discussed in this section. There are three sources for the fracture data (Table 2.1): (1) tunnel mapping (Figs. 2.4, 2.5 and 2.7) that reveal two sets of steep, large fractures noted by T1 dipping 69° and T2 dipping 72°; (2) borehole mapping (Figs. 2.9, 2.10 and 2.11) that reveal three sets of fractures noted as set A (dip 66°), set B (dip 30°), and set C (dip 09°);

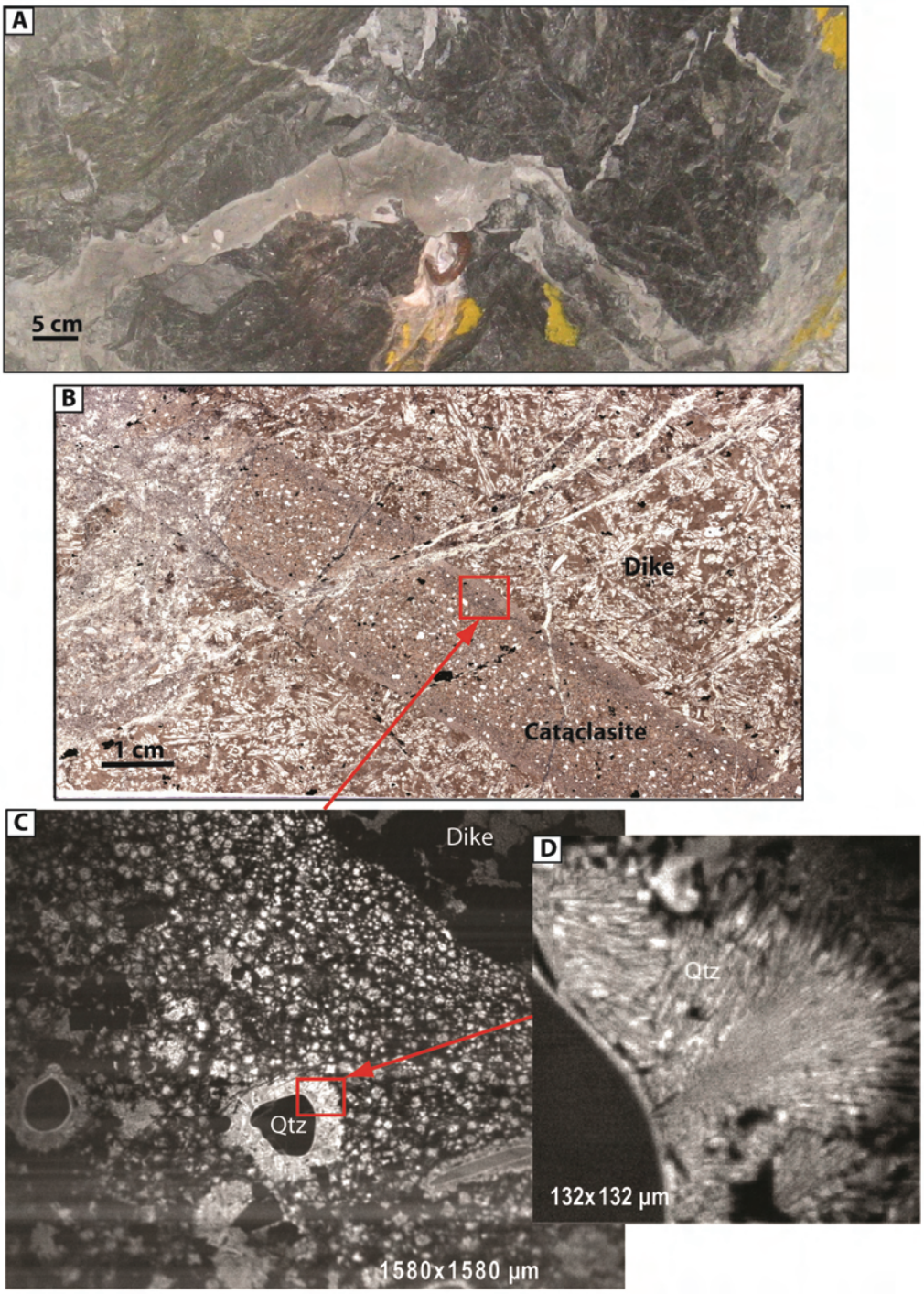

Figure 2.16: Microlitic structures within gray cataclasite. (A) Field appearance of gray cataclasite in the vicinity of the Swannie dike, 120-MM-incline. (B) Thin section of a segment with gray cataclasite within a dike. (C and D) Cathodeluminescence images of the gray cataclasite display microlitic textures (‘snow flakes’) around quartz grains (Zechmeister et al., 2005).

and (3) faults mapped by TauTona mine geologists in the reef surfaces (Fig. 2.17) that have a mean strike direction of 050°. A summary of features associated with these fractures is presented in Table 2.1 and Fig. 2.18. During the tunnel mapping, cataclasite zones of various thicknesses were found along many fractures (Figs. 2.4, 2.5 and 2.6).

Mapping sites	Set notation	Mean attitude	Structural interpretation	Comments	Fig.
Tunnels (levels 118 and 120)	T1	69°/170° ± 17°	Fault surfaces within Pretorius fault-zone	May contain cataclasite	2.7
	T2	72°/346° ± 9°			
Borehole image analyses	A	66°/139° ± 12°	Fault surfaces within Pretorius fault-zone	Found only in borehole Daf5	2.10 2.11b
	B	30°/169° ± 14°	Bedding and fault surfaces	Found in most boreholes	2.10 2.11
	C	09°/087° ± 12°	Mining related fractures	Relief of vertical load	2.10 2.11
Reef mapping	R	050° ± 14°	Faults related to the Pretorius fault	Faults, dip to north and south	2.17

Table 2.1: Different data sets used to analyze fractures in and near the Pretorius fault.

Our interpretation of the relationships between the fracture sets and the Pretorius fault is as follows (Table 2.1 and Fig. 2.18):

1. The faults of set R are sub-parallel to the Pretorius fault, that displace the reef layer up to 3 m, and form a ~100 m wide zone south of the fault (Fig. 2.17). These features suggest that the faults of set R are part of the Pretorius fault system. These faults probably represent the distributed brittle deformation during the early stages of the Pretorius fault development.
2. Fractures of sets T1, T2 and A strike generally parallel to the Pretorius fault and occur only in the Pretorius fault-zone (Fig. 2.11), and, where observed, in tunnels

Figure 2.17: Map view of fractures mapped within the mined reefs in the NELSAM area. Mapping was conducted by geologists of the TauTona mine. The fractures are projected on top of the tunnel network of level 120 (blue).

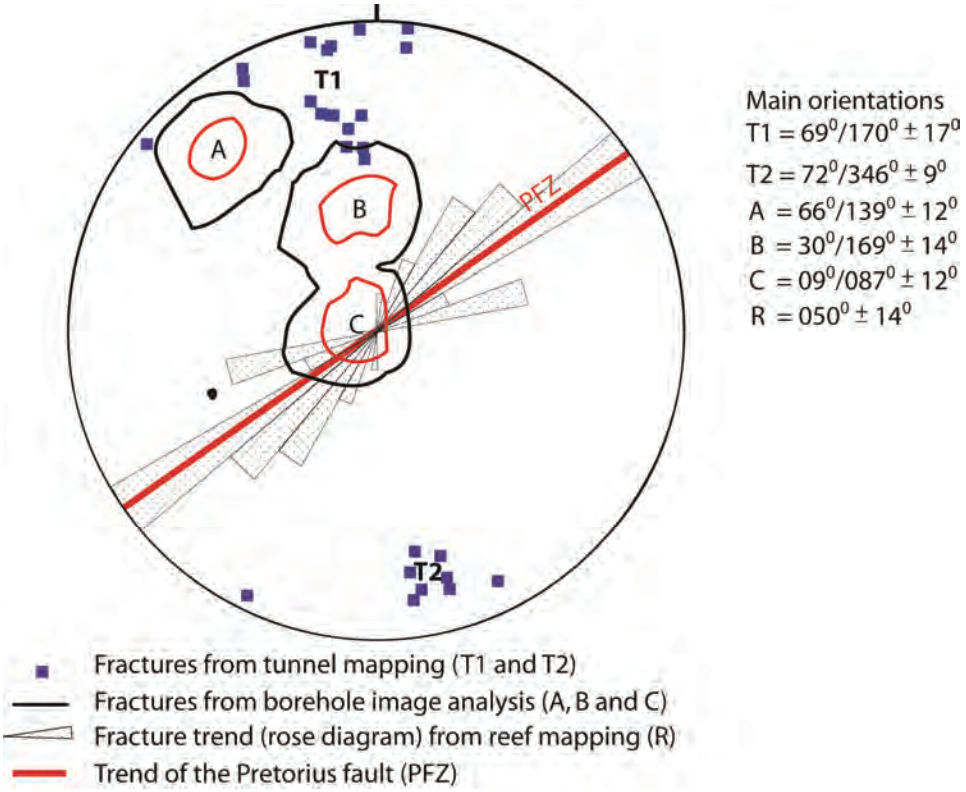

Figure 2.18: Compiled fracture orientation data. Fracture sets from tunnel mapping (T1 and T2), set A from borehole image analysis and fractures from reef mapping are sub-parallel to the trend of the Pretorius fault, suggesting a structural relation. Fracture set B formed as preexisting, weak sedimentary surfaces that may be activated during motion of the Pretorius fault. Fracture set C is interpreted to be tensile fractures induced by relaxation of vertical, gravitational load due to mining.

3. (T1, T2). Many of these features carry cataclasite zones (Figs. 2.4, 2.5 and 2.6) or slickenside striations. Evidence of displacement was found in only one case. This is probably due to the lack of markers in the tunnels (unlike mapping in the reef where displacement of the gold-bearing conglomerate layer is clearly detectable). These sets (T1, T2 and A) are interpreted as fault segments and fractures that form the Pretorius fault-zone.

4. Set B, which is sub-parallel to the bedding surfaces, is a special case. On one hand, they are found almost exclusively in boreholes away for the Pretorius fault-zone (boreholes 2, 3, 10, 7V and 7S, in Fig. 2.11), and this distribution suggests that they are not related to the Pretorius fault. However, in several locations, cataclasite zones are found along bedding surfaces (Fig. 2.4, 118-TW-Raise-120 tunnel), and even a recent rupture (Ch. 3) that occurs along a bedding surface. Hence, fractures of set B are interpreted as pre-existing, weak sedimentary surfaces that may be activated during motion of the Pretorius fault.

5. Set C (sub-horizontal fractures) is enigmatic. It is found in only two boreholes (Daf5 and hole 13 in Fig. 2.11), it is not observed in the tunnels, and its orientation has no simple relations to the Pretorius fault (e.g., a Riedel shear). The fractures in set C are suspected to be tensile fractures induced by relaxation of vertical, gravitational load that is due to mining in the reef. In this respect, they are analogous to sheet fractures in granite bodies that form sub-parallel to the ground surface due to stress relaxation (Johnson, 1970).

The above discussion raises an important question: why does the Pretorius fault display such a complicated structure with a network of anastomosing faults and fractures

(Figs. 2.4 and 2.5)? One possible reason is that the Pretorius fault, in spite of being fairly large (~10 km long, up to 200 m displacement), is still an immature fault. It is proposed that the complexity of a fault-zone decreases with increase of cumulative displacement along the fault. Wesnousky (1988) showed that the number of steps per unit fault length form a monotonically decreasing function with increasing cumulative offset. Chester et al. (1993) analyzed the San Gabriel fault, a large displacement fault of the San Andreas Fault system, and showed that the ultra-cataclasite within the core of the fault-zone displays extreme slip localization by repeated reworking, reflecting a mature internal fault-zone structure. Following these and other studies, it is commonly viewed that large crustal scale faults that accumulated large amount of displacement mostly form smooth narrow slip surfaces that may accommodate several km of slip. Aydin and Johnson (1978) showed that faults in porous sandstone evolve in stages. In the early stage, displacement is accommodated by increasing number and complexity of deformation bands (≈small faults), whereas in the later stage the displacement is only localized along a narrow slip surface, which typically develops on one side of a zone with dense deformation bands. Similar evolution processes have been observed in wet clay experiments (An and Sammis, 1996; Reches, 1988).

The Pretorius fault displays structural features that resemble the fault evolution described in the previous paragraph. The structural complexity of the Pretorius fault is attributed to its early stage of evolution, and it was found that the fault has already passed into the localization stage. A MSZ is recognized within the Pretorius fault that divides the fault-zone into a northern and southern block. This is based on structural transitions. The combination of the structural transition, thickness of the cataclasite zone and lateral

continuation of this segment, suggest that this is the most mature segment within the fault zone, and likely accommodated the majority of the slip along the Pretorius fault. The observations of ancient reactivation of the MSZ (Fig. 2.8), as well as recent reactivation during the M2.2 event (Ch. 3) support the hypothesis that the Pretorius fault has passed into a stage of localization of slip along the MSZ.

ORIGIN OF THE FAULT ROCKS

Many of the fault segments in Pretorius fault-zone contain cataclasite zones that are described in detail above (Figs. 2.6, 2.8 and text). The properties of this cataclasite are: (1) ultrafine grain matrix with poorly sorted, coarse angular to rounded clasts (Figs. 2.13, 2.14 and 2.15); (2) intense thickness variations (Fig. 2.6); (3) flow structures on macro- and micro-scales (Figs. 2.6, 2.12 and 2.14); (4) rare occurrence of fabric in the ultra fine matrix (Fig. 2.13); (5) lack of shear fabric in the coarse clasts; (6) rare evidence of melting; (7) composition similar to the host rocks; and (8) coloring in the gray-green-yellow range that differentiate them from host rocks. The estimated burial depth to form such fault rock is estimated to be within the brittle upper ~5 km of the crust. Faulting along the Pretorius fault at 2.7 Ga occurred before peak metamorphism within the Witwatersrand Basin that coincides with the emplacement of the Bushveld intrusion at 2050 Ma (Robb et al., 1997). Therefore it is anticipated that the cataclasite is a product of faulting within sandstone, later to be metamorphosed to quartzite.

Similar cataclasites have been observed in South Africa. Killick et al. (1988) studied a large, bedding-parallel fault-zone in mines and boreholes in the West Rand area, about 40 km east of TauTona mine. They found that pseudotachylytes are the prevailing fault rock in their study area. The authors did not provide evidence that these pseudotachylytes

underwent melting, and commented that pseudotachylytes could form by melt (e.g., Sibson, 1975) or cataclasite (Wenk, 1978). The field and thin-section descriptions in Killick et al. are very similar, if not identical to the cataclasite observed in TauTona mine. Here however, these fault rocks are not referred to as pseudotachylytes because the common use of the term 'pseudotachylyte' is for rocks that formed from a melt, either by shear along faults (Sibson, 1975) or by impact (Reimold, 1995; Spray, 1995). Pseudotachylyte may be in a glass form (no crystals), or in a devitrified form with evidence for melting (Lofgren, 1971) (e.g., 'snow flakes' in Fig. 2.16), however, without evidence for melt, to use the term 'pseudotachylyte' for any ultrafine grain, cohesive, dark fault rock is not justified.

Above it was proposed that the cataclasite formed as a granular material that was fluidized to form abundant flow features observed on both macro- and micro-scale. Subsequently, the granular material sintered at grain contacts under elevated temperature. This is based on observations of "hour glass" contacts in Fig. 2.15. The sintering process likely occurred during the later stage of the Platberg rifting, as the Witwatersrand Basin underwent low-grade burial metamorphism up to lower greenschist grades, with peak metamorphism during the emplacement of the mafic and ultramafic Bushveld intrusion at 2050 Ma that resulted in major thermal perturbation of the basin (Robb et al., 1997). The following 2.0 Ga period of inactivity on the Pretorius fault is likely to contribute to strengthening of the cataclasite to the current massive, cohesive state.

SUMMARY AND CONCLUSIONS

The structural characteristics of the Pretorius fault, South Africa, is described based on 3D underground mapping at a depth of 3.6 km, and borehole fracture analysis of 11 boreholes within the NELSAM site, TauTona mine. The Pretorius fault is a 10 km long, oblique strike slip fault with right lateral displacement up to 200 m and 60 m vertical displacement. The fault-zone consists of a 30 m wide zone containing tens of anastomosing segments that form conjugate sets of steeply N and S dipping segments, and minor bedding-parallel segments. The N-side of the Pretorius fault is characterized by light gray quartzitic host rock with abundant bedding surfaces, while at the S-side bedding surfaces are absent within dark gray quartzite, but quartz-veins are observed. This structural division occurs at a major segment, with a cataclasite zone up to 50 cm thick, and is interpreted to be the main slip zone (MSZ) of the Pretorius fault.

Three distinct fracture groups are distributed in and around the Pretorius fault (Table 2.1 and Fig. 2.18); (1) Fracture sets T1, T2 and A are fault segments and fractures that form in the Pretorius fault-zone, (2) Set B are bedding-parallel fractures that formed as pre-existing, weak sedimentary surfaces that may be activated during motion of the Pretorius fault, (3) Set C are tensile fractures induced by relaxation of vertical, gravitational load due to mining.

Many of the fault segments in Pretorius fault-zone contain cataclasite zones. The main properties of the cataclasite are: (1) ultrafine grain matrix with poorly sorted, coarse, angular to rounded clasts (Figs. 2.13, 2.14 and 2.15); (2) intense thickness variations (Fig. 2.6); (3) flow structures on macro- and micro-scales (Figs. 2.6, 2.12 and 2.14); (4) rare occurrences of fabric in the ultra fine matrix (Fig. 2.13); (5) lack of shear fabric of the

coarse clasts; (6) rare evidence of melting; (7) composition similar to the host rocks; and (8) coloring in the gray-green-yellow range that differentiates them from the host rocks. The massive, cohesive cataclasite probably formed by sintering of granular material.

The structural complexity of the Pretorius fault reflects its immaturity. However, it was found that the Pretorius fault passed into the stage of localization of slip along the MSZ that displays evidence of ancient as well as recent fault reactivation. This suggests that, despite a long period of inactivity leading to significant fault strengthening, its structural complexity is due to fault-zone immaturity and different fault loading conditions caused by nearby mining, the settings and accessibility of the Pretorius fault provide a unique opportunity to study earthquake and reactivation processes of single events at focal depths.

Chapter 3:

Earthquake Rupture at Focal Depth: The M2.2 Event Along the Pretorius Fault, TauTona mine, South Africa

INTRODUCTION

The M2.2 of December 12, 2004, reactivated several segments of the Pretorius fault-zone. Chapter 3 analyzes the rupture zone and investigates its mechanism of reactivation along the fault. This study provides one of the very few cases in which the structure of a rupture zone along a major fault can be studied at focal depth. There are several studies of ruptures associated with the formation of a new fault zone during rockbursts in a deep mine. McGarr et al. (1979) presented the first case in a Western Deep mine, South Africa. They mined and mapped in 3D the structure of the new fault and found a complex network of fractures formed in a previously unfaulted region, and documented a complex shear zone of fracture segments of various lengths (1 cm up to 5 m) at roughly 30° to the local direction of σ_1. These fractures form en échelon offsets to form a shear zone parallel to the maximum shear stress. While these studies demonstrated the complexity of the development of new faults in intact rock, they did not analyze the nature of rupturing along an existing, large fault. The only study that address this issue, is the analyses of the M4.6, Matjhabeng earthquake, 1999, along the Dagbreek fault, Welkom, South Africa (Dor et al., 2001). This event, mapped in three tunnels at 1660 m below surface, displaced rail tracks within a tunnel for 44 cm vertically. Displaced rock bolts were found up to a distance of 30 - 45 m from the main Dagbreek fault, showing the width of the rupture zone. This zone is characterized by several fine grained and/or clayey, soft fresh

gouge zones of 0.5 – 5 cm thick that characterize individual slip surfaces of the M4.6 rupture.

Fault-zones are generally weaker than the surrounding rocks and thus tectonic loading in the upper crust leads to localization of shear along the weaker faults. The activity period of a fault is determined by the duration of the regional tectonic activity, and faults become dormant when the latter stops (Scholz, 2002; Thatcher, 1983). During periods of activity, faults do not slip at a constant rate but typically move by infrequent earthquakes, that are separated by tens to thousands of years. Even after becoming dormant, faults may be reactivated by a younger tectonic phase, frequently with inversion of the sense of motion along a given fault. For example, Reches (1978) describes the Palisades fault, the major structure in the Palisades Creek branch of the East Kaibab monocline, in the Grand Canyon, Arizona. They discuss that the first phase of normal faulting during the late Precambrian is overprinted by reverse faulting during the Laramide orogeny, which formed the present monocline in the Palisades Creek. Similar reversal of slip has been reported on the Colorado Plateau (Huntoon, 1974), as well as within the North Sea basin, e.g. Oudmayer and de Jager (1993) and Wiprut (2000), and in many other locations around the world, at multiple scales (Lowell, 1995). Thus one can establish two timescales of fault reactivation: a short term of $10^2 – 10^4$ years, and a long term of $10^6 – 10^7$ years between tectonic phases. The central question of this study is the mechanisms of fault reactivation after a very long period of inactivity. The Pretorius fault in TauTona mine, South Africa, provides another site for such a study as it has been reactivated by mining activity after a dormant period of ~2.0 Ga.

The study of the rupture of the M2.2 event is approached from several directions. First, the exposed rupture zone was mapped at its focal depth in 3D. Second, mechanical properties of the fault rocks along the Pretorius fault were determined from rock mechanics experiments. Third, the effects of the measured mechanical heterogeneities on reactivation processes were analyzed by the finite element method. Later, in Ch. 4, the stresses associated with the rupture are discussed, as well as the earthquake energy balance.

SETTING OF THE RUPTURE ZONE

The NELSAM (Natural Earthquakes Laboratory in South African Mines) project was designed to conduct studies on earthquake ruptures at their focal depths (Reches, 2006). The main site of the project focuses on the Pretorius fault within the TauTona mine (Ch. 1). This chapter focuses on the analysis of the rupture of the M2.2 event of December 12, 2004, that is exposed within a few tunnels in the Tautona mine at a depth of 3.6 km. This event reactivated several quasi-planar segments of the Pretorius fault-zone that formed ~ 2.7 Ga ago and has been inactive during the last 2.0 Ga. The structural details of the Pretorius fault were described in Chapter 2. The objective of the present chapter is to analyze the rupture zone and to investigate the mechanisms of reactivation.

STRUCTURE OF THE PRETORIUS FAULT

The present study is conducted in the TauTona mine, located in the Western Deep Levels of the Witwatersrand Basin, South Africa (Fig. 3.1). The tectonic setting of the study area and the structure of the Pretorius fault-zone were presented in Chapter 2 and only the main features are outlined here. The Witwatersrand Basin consists of about 10

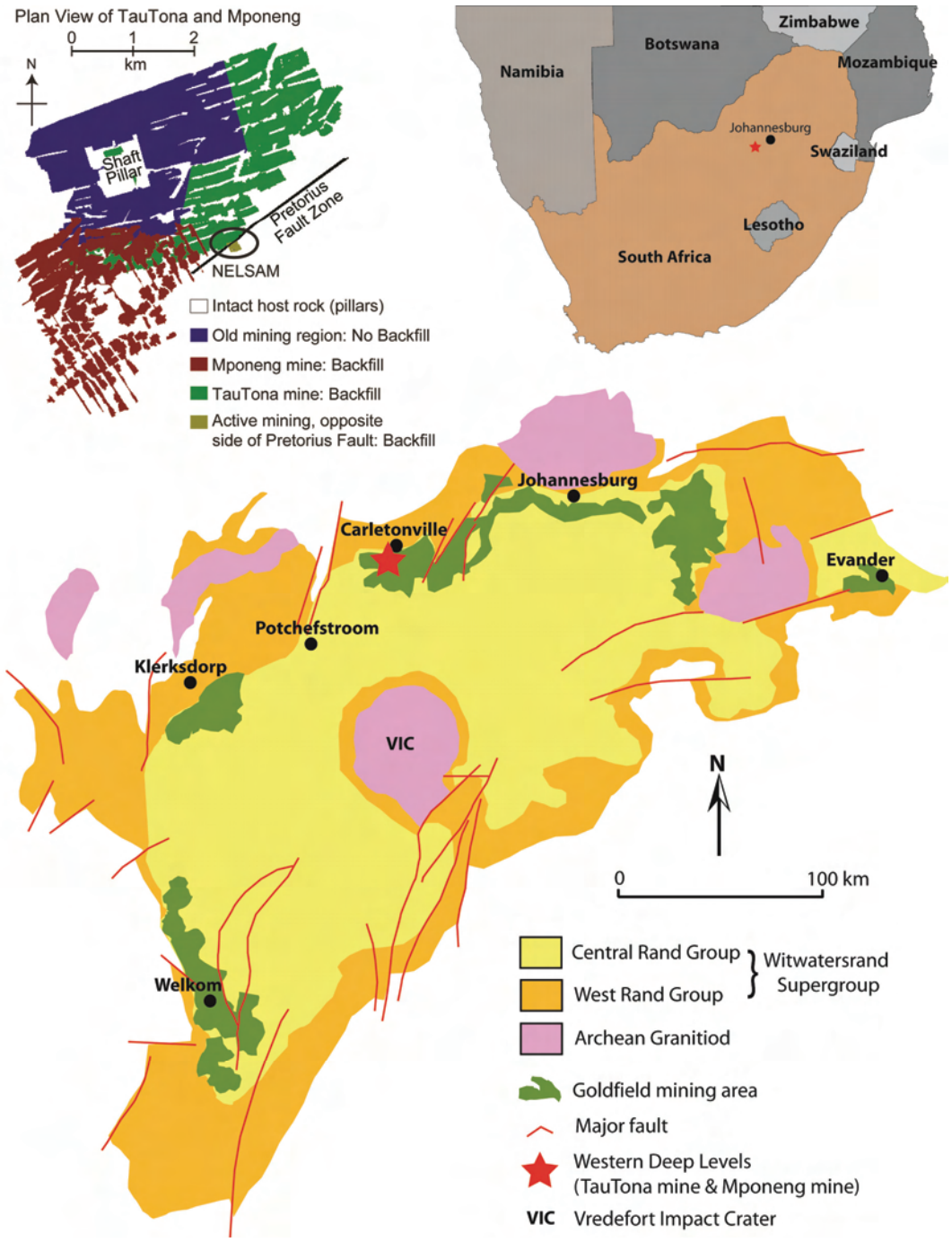

Figure 3.1: Simplified geological map of the Witwatersrand Basin, South Africa, illustrating the distribution of the Witwatersrand Supergroup and the Archean Granitoid, the major goldfields and the location of the TauTona and Mponeng mine in Western Deep Levels (after Frimmel and Minter, 2002). Upper-left corner displays the location of the NELSAM research area and the Pretorius fault within the mining grounds of TauTona and Mpeneng, in map view (after Lucier et al. (2009)). Mponeng is mining the Ventersdorp Contact Reef, ~800 m above the Carbon Leader Reef.

km thick sequence of sedimentary rocks, mainly sandstones, mudrocks, and gold-bearing conglomerates (Armstrong et al., 1991; Gibson et al., 2000b; Robb et al., 1997). The basin underwent low-greenschist grade metamorphism and was tectonically inactive for the last 2.5 Ga (Robb et al., 1997). The Pretorius fault is a 10 km long, ENE trending, oblique, right-lateral fault forming a sub-vertical fault-zone (see Ch. 2). The fault has right-lateral displacement of about 200 m, and vertical displacement of 30-100 m. It is a complex structure with tens of segments that form a 25 – 30 m wide network of cross-cutting and anastomosing faults and fractures (Ch. 2). The segments are dominantly east-west striking, steeply dipping (40°-90°), quasi-planar surfaces that crosscut, intersect and branch from each other, and minor bedding-parallel fault surfaces that dip ~22° southward. Most of the segments contain a highly cohesive, green to gray quartzitic cataclasite that varies in thicknesses from a few millimeters to tens of centimeters (Ch. 2). Its ultra-fine matrix is poorly sorted, with coarse and angular to rounded clasts. A foliation is rarely developed within the cataclasite zones and the cataclasite lacks shear fabric of the coarse clasts. Abundant flow features on macro- and micro-scale consist of injection veins and flow banding. The cohesive cataclasite possibly formed by sintering of granular material (Ch. 2).

SEISMICITY OF THE PRETORIUS FAULT REGION

The seismic activity of the NELSAM area was described in a series of recent papers (Boettcher et al., 2007; Boettcher et al., 2009; Boettcher et al., 2006; McGarr et al., 2009), that discuss the relation of seismic events with the Pretorius fault (Fig. 3.2a), after the relocation of several events of M>2. This chapter focuses on the rupture-zone of the M2.2 event of December 12, 2004.

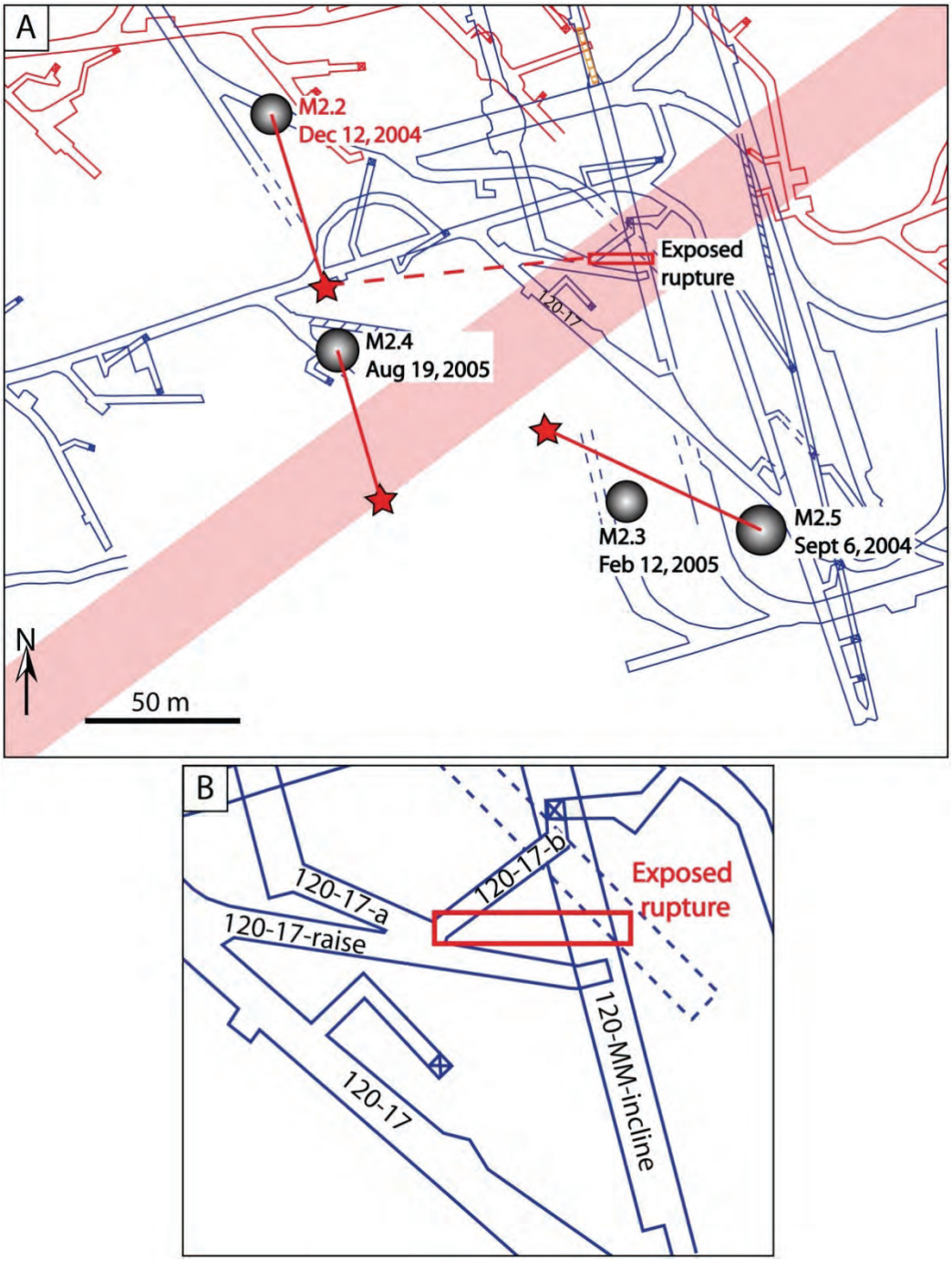

Figure 3.2: Location map of events within the NELSAM area. (A) Locations of events M>2 that occurred since January 2004. The circles represent the hypocenters as determined by the seismic network of ISS International, stars represents relocations of the events (Boettcher et al., 2006). The location of the exposure of the M2.2 event of December 12, 2004 (red box) is 120 m away from the locations suggested by the seismic records. (B) Close up of the pre-rupture tunnels of 120-17-TW, consisting of 120-17-raise, 120-17-a and 120-17-b tunnels, and the 120-MM-incline that was developed six months after the rupture of the M2.2 event. The location of the exposure of the rupture zone is given in red.

The M2.2 event triggered 16 seismometers of the ISS network in TauTona mine that was described in van Aswegen and Butler (1993). Analysis by ISS assigns a moment of 2.6×10^{12} Nm and a radiation energy of 3.0×10^{7} J to this event (Boettcher et al., 2006). The damage reported by miners and the exposed rupture-zone, analyzed by us, are located within the Pretorius fault-zone at the 120-17-Raise and 120-MM-incline tunnels (Fig. 3.2). This location is 120 m away from the hypocenter location as determined by the ISS seismic network (Fig. 3.2a); the apparent location error is probably due to the large spacing (~0.5 km) of seismometers in the TauTona mine and the quasi two-dimensional distribution of these stations (van Aswegen, personal communication).

The damage by this event is located in the 120-17-TW tunnel, consisting of 120-17-raise, 120-17-a and 120-17-b (Fig. 3.2b). Major damage occurred along 70 m in the 120-17 tunnel (Fig. 3.2b), that closed down the tunnel due to safety hazards. Several nearby tunnels suffered minor damage as reported by miners. The rupture-zone itself is exposed at the intersection of the 120-17-raise and 120-17-b tunnel (Fig. 3.2b). These exposures are regarded as the rupture-zone of the M2.2 December 12, 2004 event and mapped in detail. Six months after the event, in June 2005, a second tunnel (120-MM-incline) was developed east of the lateral extension of the rupture-zone, oblique to the 120-17-b tunnel (Fig. 3.2b). This new tunnel was excavated across the rupture-zone and allows us to extend our mapping, similar to the previous studies of McGarr et al. (1979) and Ortlepp (2000) that were conducted on different rupture zones.

STRUCTURE OF THE RUPTURE ZONE OF THE M2.2 EVENT

GENERAL STRUCTURE

The rupture-zone reactivated at least three and possibly four segments of the Pretorius fault-zone, including one bedding surface. A cross section through the rupture-zone area displays the reactivated segments (Fig. 3.3a). The figure includes the structural features of the Pretorius fault-zone (Ch. 2) and the trace of the reactivated segments as observed in the 120-MM-incline (Fig. 3.3b).

The reactivated segments can be identified by the presence of fresh white, fine grained gouge, referred to as 'rock flour' that developed along the slip surfaces (Figs. 3.4, 3.5 and 2.8). Such rock flour is typically observed for rock-burst ruptures within South African mines and evidently generated by shear (Dor et al., 2001; McGarr et al., 1979; Ortlepp, 2000; Stewart et al., 2001). The presence of this rock flour was used to locate and trace the M2.2 rupture. All reactivated segments are quasi-planer and contain cataclastic fault rock varying in thickness from a few mm to tens of cm. The reactivated segment A is oriented 43°/167° (Figs. 3.3, 3.4a), contains 1-6 cm thick zone of cataclasite. Reactivated segment B is a bedding-parallel surface (Figs. 3.3, 3.5a, 3.5b) oriented 20°/161° that branches from surface A. The third segment, marked C in Fig. 3.3 and orientated 81°/149°, is interpreted as the main slip zone (MSZ) of the Pretorius fault-zone with a cataclastic zone up to 50 cm thick (Figs. 3.3, 3.5c, 2.8). The nature of the MSZ segment was described in Ch. 2. Segments A and B can be traced horizontally for 25 m and 5 m vertically. The rupture along segment C can be traced horizontally for ~6 m and ~5 m vertically.

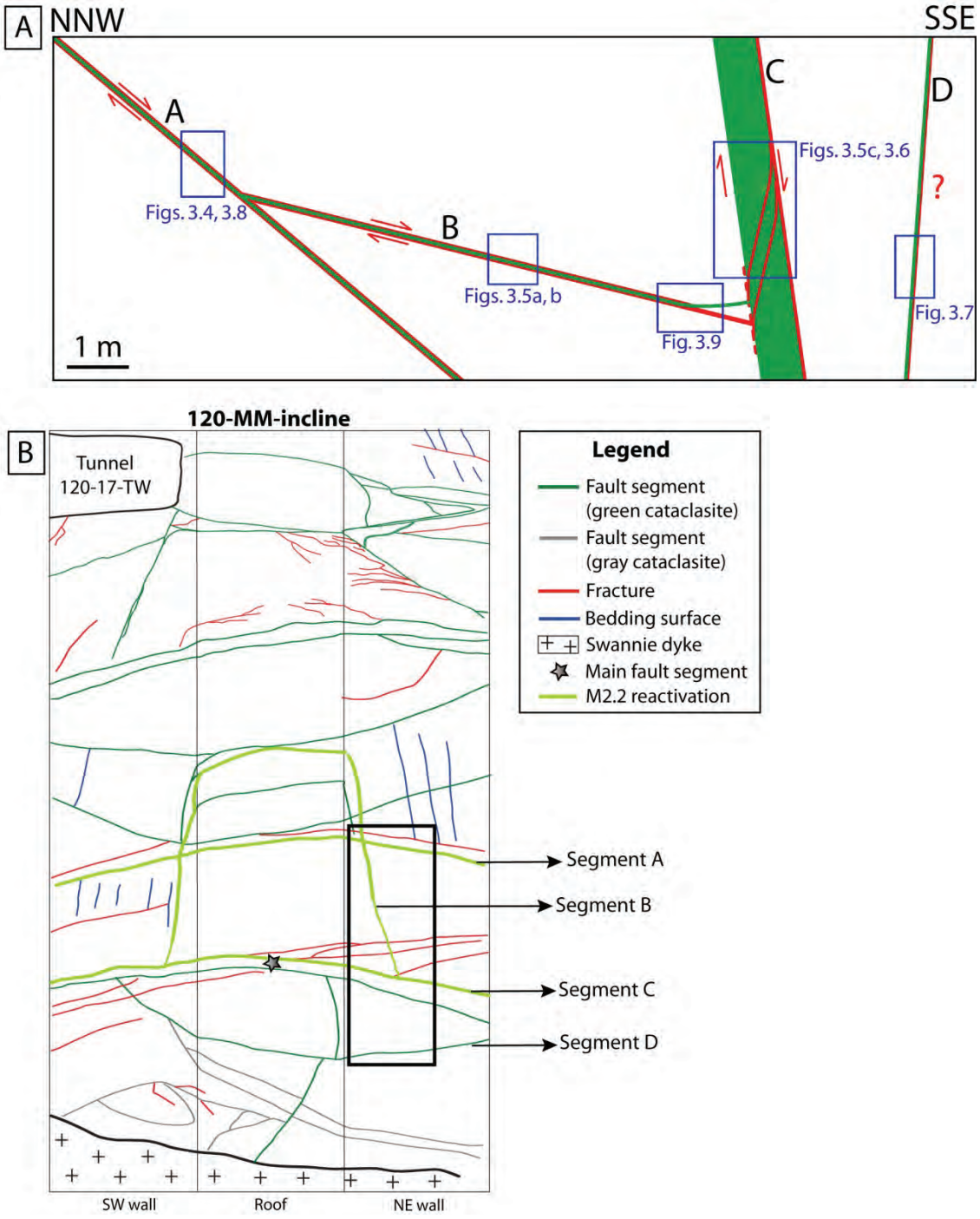

Figure 3.3: The exposed M2.2 rupture. (A) Schematic cross section of the rupture that reactivated 3, possibly four segments of the Pretorius fault (A, B, C and D). In green the cataclasite bearing fault segments of the Pretorius fault, in red the rupture of the M2.2 based on the generation of fresh rock flour. (B) The trace of the reactivated segments and the location of the cross section are highlighted in the tunnel map though the 120-MM-incline (Ch. 2).

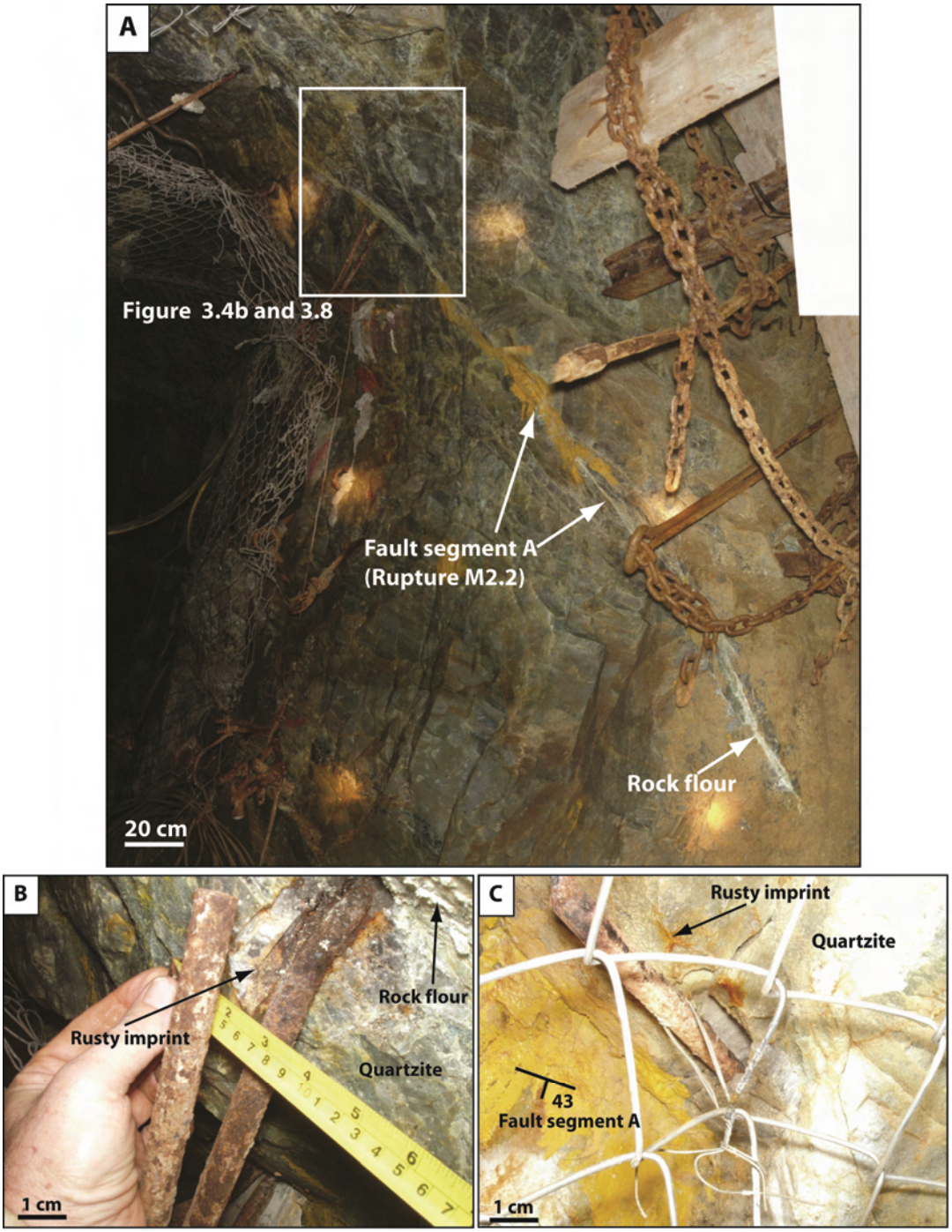

Figure 3.4: Exposed rupture of the M2.2 within the south part of the 120-17-b tunnel. (A) Rupture surface A. The rupture is recognized by the generation of fresh white rock flour. (B) Displaced rock bolt with a measured displacement of 25 mm. The rusty imprint represents the original position of the rock bolt. (C) Displaced rock bolt within the roof, cutting segment A (yellow paint), with a measured displacement of 10 mm. The rusty imprint represents the original position of the rock bolt.

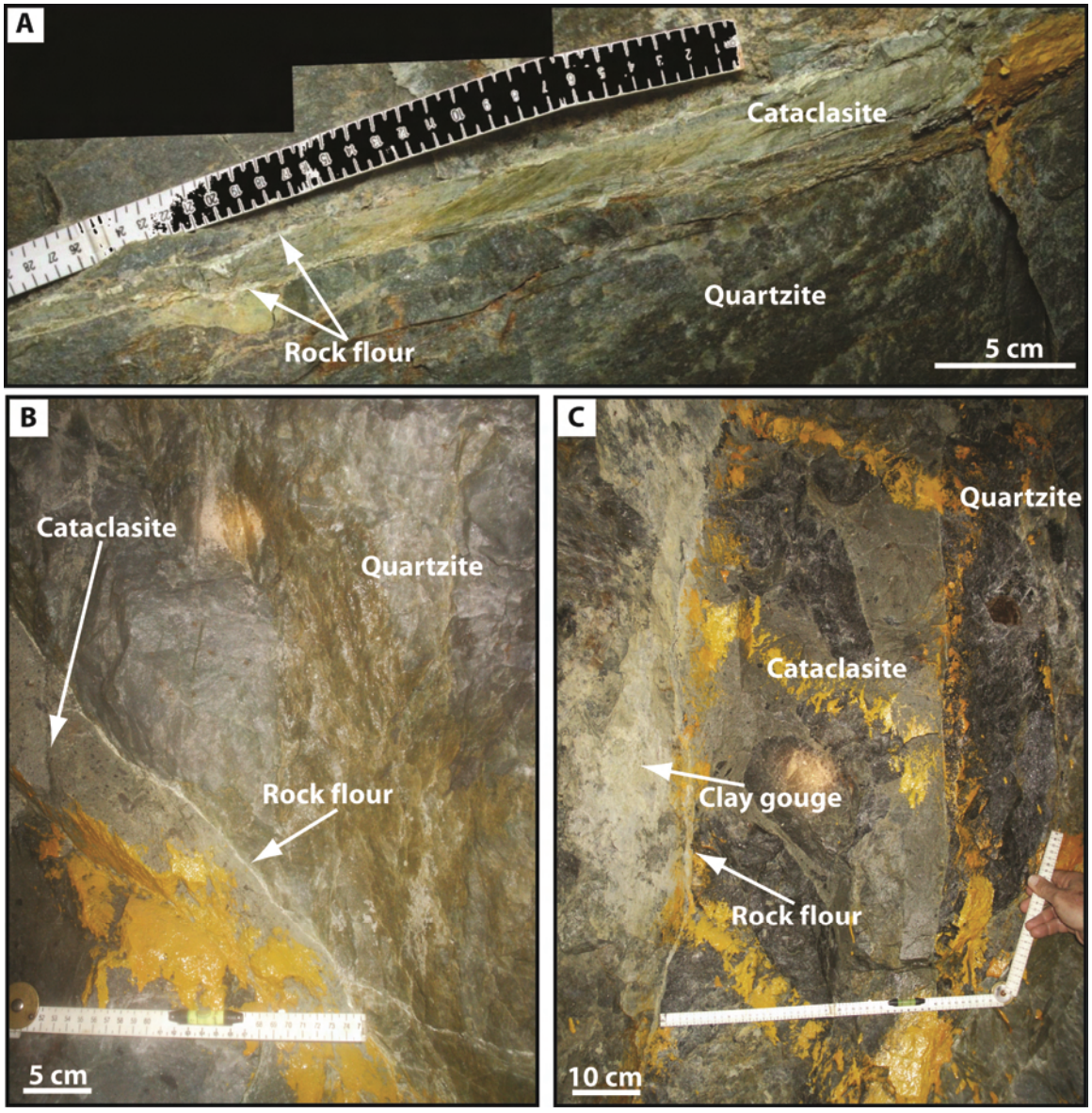

Figure 3.5: Exposures of the M2.2 rupture that reactivated the Pretorius fault and generated rock flour as slip localized along the contacts of the cataclasite and the quartzite. (A) Rock flour along segment B, a bedding-parallel fault segment, within the south wall of the 120-17-b tunnel. Rock flour occurs on both the upper and lower contact. (B) Rock flour along segment B within the NE-wall of the 120-MM-incline. (C) Fine grained rock flour and coarser grained gouge along the south contact of the main fault surface, surface C, of the Pretorius fault, within the SW-wall of the 120-MM-incline. Note the rounded quartz grains within the fault segment several tens of cm in diameter.

Surrounding tunnels east and west of the exposed rupture are separated 45 m and did not display rupture surfaces, thus bounding the extent of the rupture-zone. The mined reef is situated ~20 m above the exposed rupture surface (Fig. 2.2, Ch 2), and can be approximated as a free surface that bounds the maximum upper extents of the rupture-zone. This limits the maximum area of reactivated fault surfaces to 3,375 m^2. Continuous exposures of the rupture suggest a minimum area of at least 280 m^2. The estimated rupture area from the seismic signal of 2900 m^2 (Boettcher et al., 2006) suggests that ~10% of the rupture zone is exposed.

Slip localization

The observed slip associated with the M2.2 event along the reactivated segments described above is localized dominantly at the contacts of the cataclasite and the quartzitic host rocks (Figs. 3.4, 3.5, and 2.8). The slip generated a white, ultra-fine grained, incohesive gouge (referred to as rock flour) that is commonly observed in mines (Dor et al., 2001; McGarr et al., 1979; Olgaard and Brace, 1983; Ortlepp, 2000; Stewart et al., 2001). The rock flour is frequently distributed along both upper and lower contacts of the cataclasite and the quartzite (Fig. 3.5a). Segments A and B display rock flour of 1-5 branching zones, with a thickness of 0.5-1 mm each, observed along most of the exposure (Figs. 3.4 and 3.5). No observations were made of segment A and B, in which the rock flour cross-cut the 1-6 cm thick cataclasite zone.

The reactivated segment C, MSZ of the Pretorius fault-zone, consists of a 30-50 cm thick cataclasite and indicates two older phases of activity that resulted in the dark and the lighter green cataclasite (Ch. 2). The first phase, generating the dark green cataclasite, is interpreted to be the oldest phase of activity, during the formation of the Pretorius fault.

The second phase, generating the lighter green cataclasite, is concentrated along the edge of the dark green cataclasite. Locally the light green cataclasite crosses the dark green cataclasite following a Riedel shear that fits a right lateral shear, as the south block of segment C moved up with respect to the north block (Fig. 2.8). The slip during the reactivation of the M2.2 event is localized along the south-side contact, between the cataclasite and the quartzite (Fig. 3.5c). A zone of ~1 mm thick of fine grained rock flour developed along this contact similar to segments A and B. In addition to the rock flour, a coarser gouge zone was formed, dominantly along the south side contact (Fig. 3.5c). This gouge apparently has a coarser grain than the rock flour, and its thickness is up to 5 cm. This coarse gouge is interpreted to be gouge formed by the rupture of the M2.2 event. At one local a fracture that carries the coarse gouge crosses the cataclasite from the south contact of segments C to the north contact (Fig. 2.8). This structure appears to be a Riedel shear that fits the normal slip component during the M2.2 rupture (Figs. 3.3 and 2.8).

The third phase of activity, the reactivation during the M2.2 event that generated rock flour, displays similar characteristics as the second phase that generated light green cataclasite; in both cases the slip dominantly localized at the contact. During both phases, local Riedel shear structures transfer slip across the segment. The slip during the recent rupture, however, suggests slip in an opposite sense than the second phase (Fig. 2.8). Nevertheless, similar characteristics suggest that the recent reactivation of the Pretorius fault due to nearby mining activity occurs following similar mechanisms as the ancient slip, more than 2 Ga ago.

A fourth segment, D, oriented 85°/340°, was reactivated (Figs. 3.3 and 3.6). The segment was traced for 6 m horizontally and 5 m vertically within the120-MM-incline

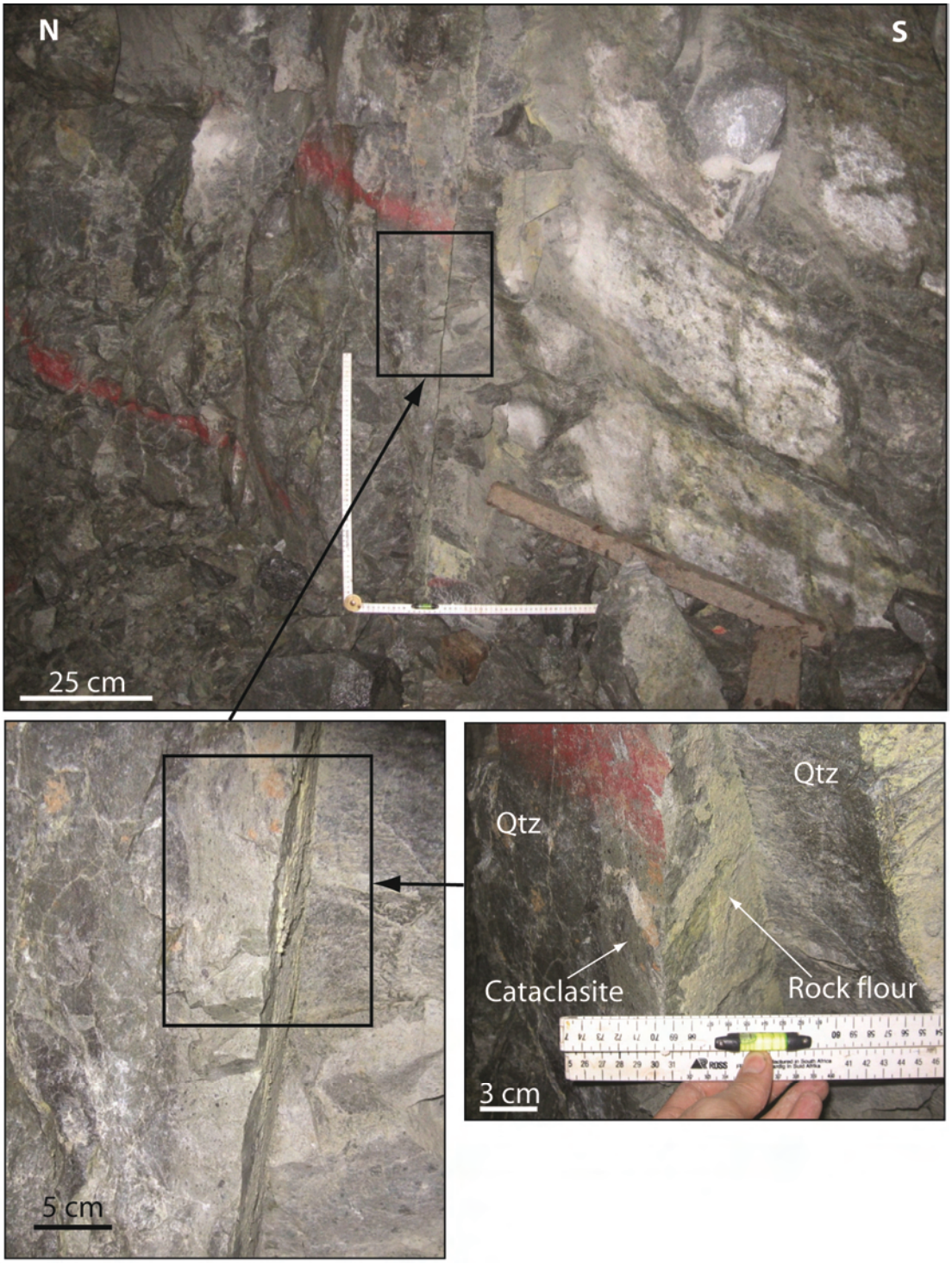

Figure 3.6: Possible reactivation during the M2.2 event of segment D, within the NE-wall of the 120-MM-incline. The south contact of this segment displays 1-2 mm thick zone of fresh rock flour, similar to the observations along segment A, B and C.

and displays a 2-10 cm thick cataclasite. The slip along this segment localized along the south contact of the cataclasite and the quartzite (Fig. 3.6), and generated rock flour in a 1-2 mm thick zone. The reactivation along segment D was discovered at a later stage of the mapping; hence it remains ambiguous whether its reactivation is associated with the M2.2 rupture or by another event.

Displacement

Evidence for displacement during the M2.2 event was found at two locations in which rock-bolts were cross-cut by segment A within the 120-17-TW (Fig. 3.4). The pre-rupture positions of the rock-bolts are recognized by a rusty imprint within the quartzite (see Figs. 3.4b and 3.4c). The measured displacement produces a normal-dextral slip with a rake of 23° and 35°, on segment A, oriented 43°/167°, with magnitudes of 10 mm and 25 mm respectively. No additional evidence of measurable displacement was found.

FRACTURES ASSOCIATED WITH THE RUPTURE

The M2.2 event ruptured distinct, pre-existing segments of the Pretorius fault, evidenced by the occurrence of rock flour along cataclasite zones. These rupture surfaces are quasi-planar and continuous but at several locations, more complex fracture systems were observed that are associated with the rupture that will be discussed later in this chapter.

The rupture-zone in the 120-17-TW tunnel is accompanied by a set of sub-vertical, secondary tensile fractures (Fig. 3.7). These fractures are interpreted as wing cracks (mode I cracks that form at the tips of a mode II fracture) at an angle that maximizes the local tensile stress acting across the incipient crack path (Reches, 1988). The wing cracks

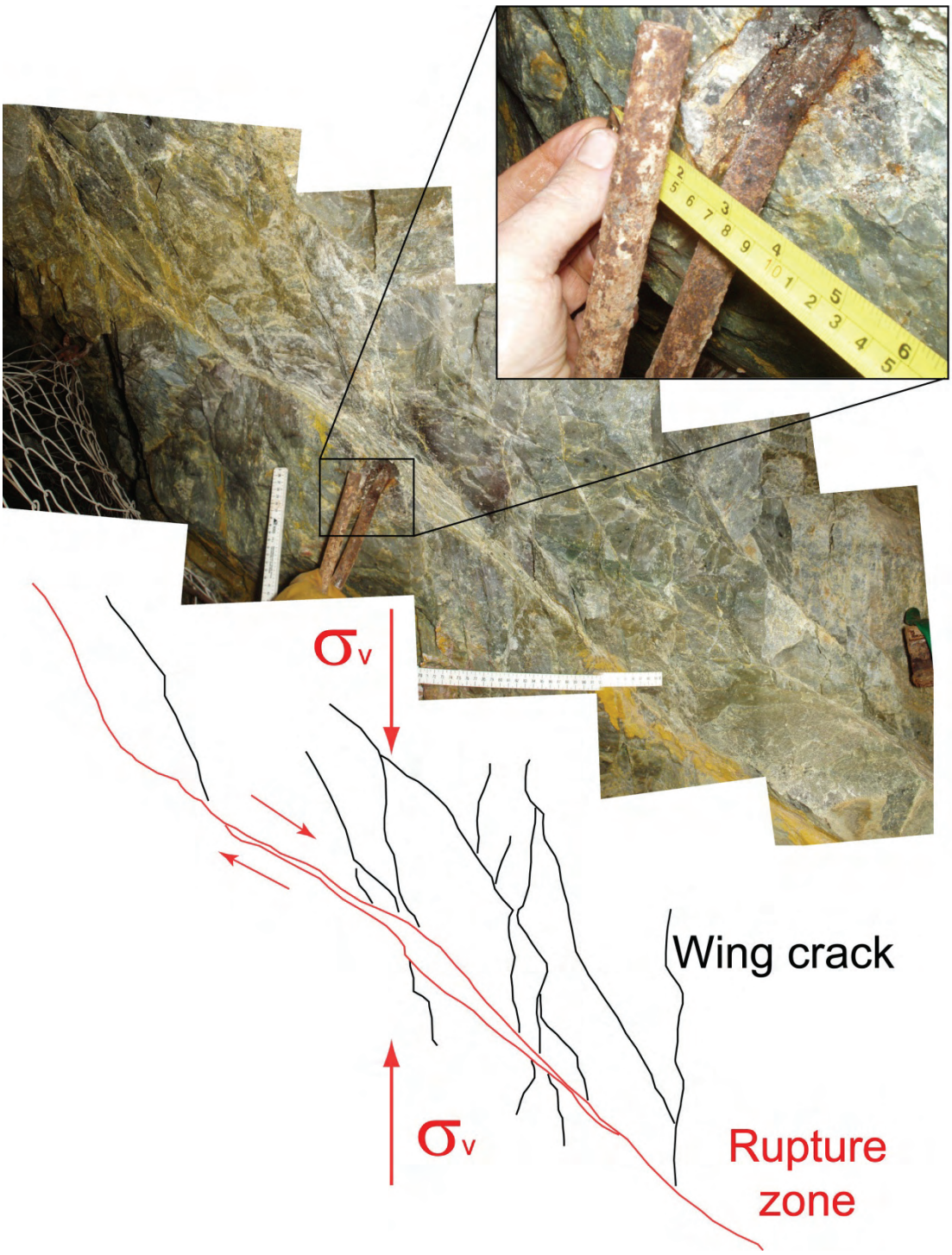

Figure 3.7: Secondary tensile fractures (wing cracks) associated with the rupture, developed in the hanging wall of segment A. Concave structure of the fractures results from propagation away from the rupture, in the direction of the major axis of compression which is sub-vertical from the overburden (σ_v). The wing cracks developed at the location of the displaced rock bolt of Fig. 3.4.

tend to propagate towards the axis of maximum compression (Germanovich et al., 1994). The wing cracks in 120-17-TW formed in the hanging wall of the rupture that reactivated segment A with development of minor amounts of fresh rock flour (Fig. 3.7). These cracks appear to nucleate at the tip of the propagating rupture, associated with a dextral-normal slip component. After nucleation the cracks eventually propagate into the direction of the maximum compressive axis which, in this extensional regime, is sub-vertical (σ_V in Fig. 3.7).

The observed normal slip component of the rupture is also in agreement with the observation of segment B and C within the120-MM-incline. Segment B deflects to become sub-horizontal, before it intersects at almost right angles with the main segment C (see Fig. 3.8). At this deflection, the rupture splits: one part continues to follow the contact between the cataclasite and the quartzite; one part continues in a straight line, cutting the quartzite until it hits segment C. The rupture widens as it cuts through the quartzite, forming a 1-2 cm wide shear zone with the development of multiple Riedel shear structures (Fig. 3.8). This suggests a normal slip component during the rupture, in agreement with to the suggested slip by Riedel shear structures within segment C and the measured rake of the displaced rock-bolts within segment A.

MAIN FEATURES OF THE RUPTURE-ZONE

The M2.2 rupture-zone is recognized by: (1) intense local damage in a few tunnels; (2) formation of fresh, fine-grained, white gouge (rock flour) along several segments in the fault-zone; and (3) displacement of rock-bolts along the slipped fault segments. The main structural features of the rupture zone are the following:

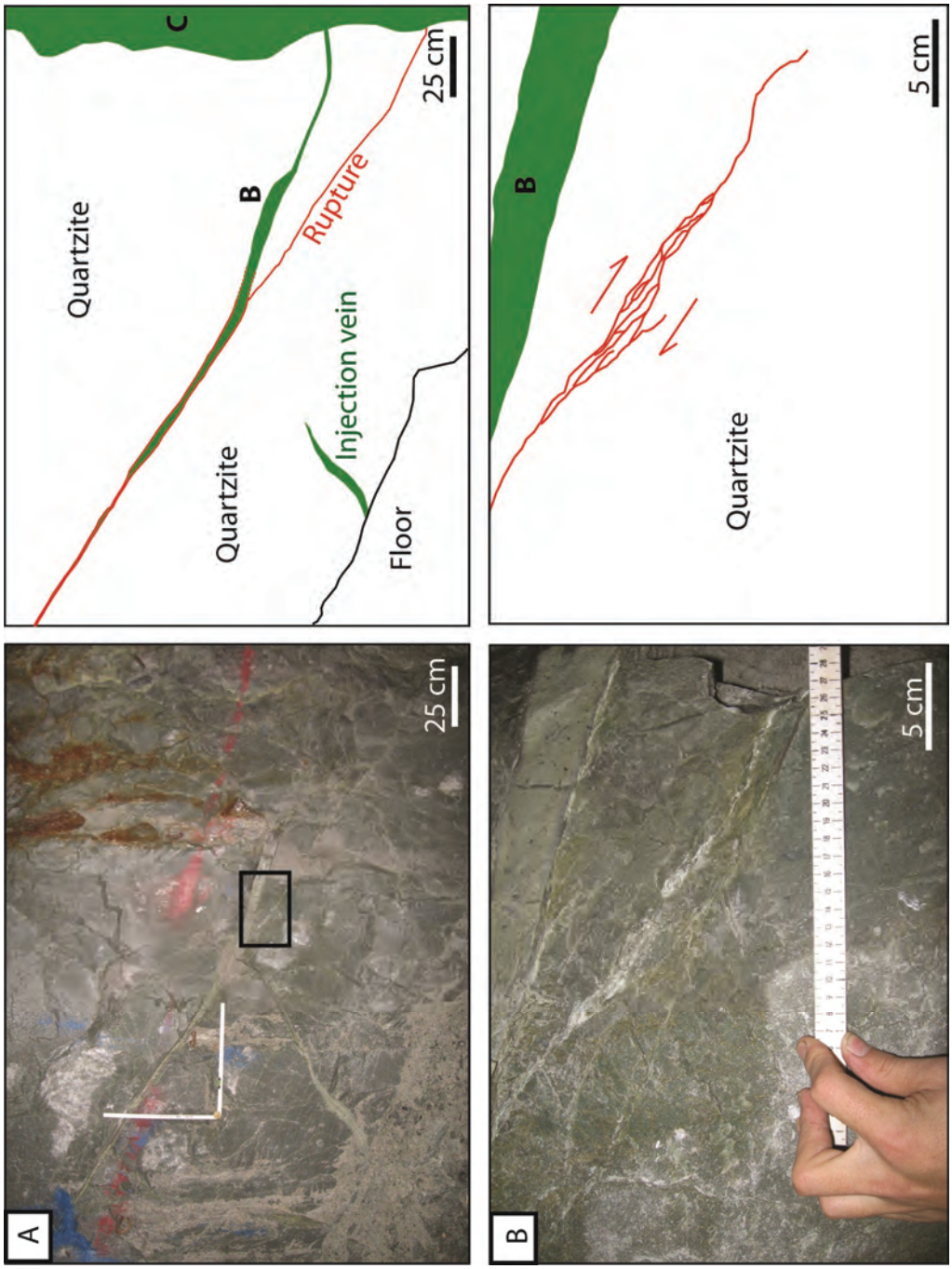

Figure 3.8: Rupture zone along segment B, bedding-parallel, near the intersection of segment C. (A) Overview of the rupture as it traced the contact of segment B. Right side represents the geological interpretation of the picture on the left. As segment B deflects to become sub-horizontal near the intersection with segment C, the rupture splits in two: one part continues to follows the contact between the cataclasite and the quartzite; one part continues in a straight line, cutting the quartzite until it hits segment C. (B) Close up of the rupture as its cuts through the quartzite. The rupture zone widens to form a 1-2 cm wide shear zone with development of multiple Riedel shear structures, suggesting a normal slip component.

1) Slip occurred along three to four, pre-existing large, quasi-planer segments of the Pretorius fault, that are not parallel to each other (Fig. 3.3).
2) Slip, as identified by the presence of the rock flour, was almost exclusively localized along the contacts between the cataclasite of the ancient fault segment and the quartzitic host rock (Figs. 3.3, 3.4, 3.5 and 3.6).
3) Locally, slipped segments display complex networks with multiple small fractures of tensile (Fig. 3.7) or shear character (Figs. 2.8 and 3.8).
4) The maximum measured shear displacement is 25 mm in oblique, normal slip.
5) Gouge zones range in thickness from ~ 1 mm to 5 mm at a given position. These values indicate wear-rates of at least 0.4 $mm^3/N{\cdot}m$. Wear-rate is calculated here by [(volume of wear products) / (area of sliding surfaces)] / [normal stress·slip distance].

ROCK MECHANICS EXPERIMENTS

The mechanical properties of rocks in the Pretorius fault-zone were determined from experiments. The samples were derived from cores of boreholes drilled during the NELSAM project, across the fault-zone. The measured properties include strength, elastic parameters and acoustic velocities under confining pressures up to 200 MPa. A total of 30 experiments were conducted in the rock mechanics lab of the USGS in Menlo Park, CA.

SAMPLE COLLECTION

Samples from within the Pretorius fault-zone were collected from three boreholes, DafBio, Daf1 and Daf2 (location Fig. 3.9). The boreholes were drilled in quartzites sub-

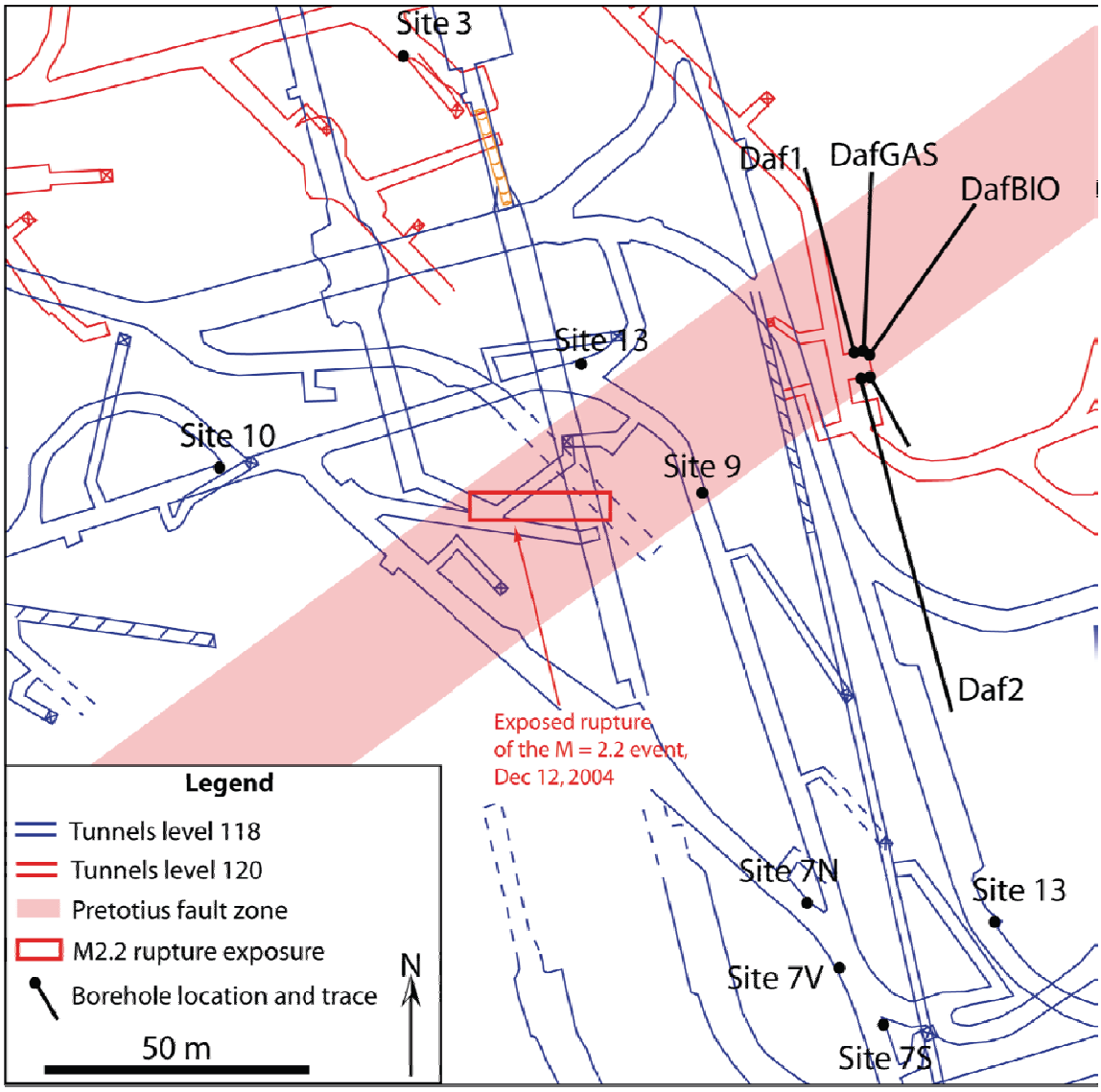

Figure 3.9: Map view of the NELSAM area, TauTona mine, South Africa. Tunnels of level 118 (red) and level 120 (blue) are projected on top of each other. The currently mined area dips 20-25° to the SSE and is offset by the Pretorius fault. The borehole locations at different NELSAM sites are illustrated. Site 2 and 3 are vertical boreholes at level 118, site 6, 7V, 9, 10 and 13 are vertical boreholes at level 120. Daf1, Daf2, DafGAS, DafBIO and Daf5 are inclined boreholes, drilled from the NELSAM cubby at level 118.

parallel to bedding that locally dip ~ 22° to the south. The host rock samples (quartzite) contain delicate bedding features, recognized by grain size differences and pyrite rich beds, oriented sub-parallel to the sample axis. Fault-rock (cataclasite) samples were taken from DafBio and contain a poorly developed foliation oriented 20° - 30° to the sample axis.

EXPERIMENTAL SETUP

A total of 22 quartzite samples and 8 cataclasite samples from within the Pretorius fault were prepared. The quartzite cores were re-drilled to 75 mm long samples, 25 mm in diameter. The more brittle cataclasite samples were cut into rectangular prisms of 55 x 18 x 18 mm. A two component strain gage was mounted on seven quartzite samples and three cataclasite samples to record axial and traverse strain. The quartzite samples were jacketed with a polyurethane jacket, and the cataclasite samples were jacketed with heat shrink plastic. All experiments were conducted in a standard non servo-controlled triaxial test apparatus with oil confining medium, external load cell and under room-dry conditions at room temperature. Sixteen quartzite experiments were run, with duplicates, at 0, 20, 60, 90, 120 and 200 MPa confining pressure, and five cataclasite experiments were run at 0, 20, 60 and 120 MPa confining pressure. Strain gages were used on both rock types samples at 20, 60, 120 and 200 MPa confining pressure. An axial strain-rate of 3×10^{-6} s^{-1} was typically applied by an axial piston velocity of 0.2 μm/sec. Most experiments were carried out to failure; six quartzite experiments were terminated after a total piston displacement of 5 and 10 mm to initiate stable sliding. Three sliding experiments with 5 mm piston displacement were conducted on the cataclasite samples.

The conditions and main results are listed in Table 3.1. Poisson's ratio was determined only for experiments that included strain gages.

Table 3.1a: Quartzite samples

Experiment	Sample	Confining pressure (MPa)	Peak differential stress (MPa)	Youngs modulus (GPa)	Poisson's ratio
Nel24	DF2_23Bb	0	174.7	76.9	
Nel07	DB13 b	0	149.6	74.4	
Nel01	DF2_23Aa	0	232.7	75.1	
Nel29	DF2_21b	20	212.7	76	
Nel31	DB18a	20	217	77.5	
Nel08	DF1_33b	20	338.9	77.1	0.20
Nel09	DF2_24a	20	273.3	75.7	0.35
Nel11	DF1_31Aa	40	261.1	74.7	
Nel10	DF2_23c	40	350.8	78.4	
Nel23	DB12b	60	440.3	74.8	0.17
Nel13	DF2_23Aa	60	387.4	70.4	0.21
Nel16	DF1_32Bb	60	320.8	72.1	
Nel14	DF1_31B	60	392.3	71.6	
Nel15	DF1_31Ab	90	467.5	75.1	
Nel17	DF2_26a	90	299	74.3	
Nel22	DF2_21c	90	398.5	81.2	
Nel21	DF1_32Aa	120	534	78.5	
Nel19	DB13a	120	457	83.6	0.17
Nel18	DB11	120	549.3	82.1	0.18
Nel20	DF2_22a	120	439.7	71.5	
Nel27	DF2_26b	200	453.9	87.9	0.19
Nel28	DF1_32Ab	200	380.8	82.2	

Table 3.1b: Cataclasite samples

Experiment	Sample	Confining pressure (MPa)	Peak differential stress (MPa)	Youngs modulus (GPa)	Poisson's ratio
Nel32	DB50Bb2	0	95.1	42.6	
Nel34	DB14Aa2	0	115	44.1	
Nel39	DB50Ba2	20	167.9	52.2	
Nel35	DB14Aa1	20	83.9	71.7	0.13
Nel40	DB14Ab1	60	219.9	52.3	
Nel36	DB50Bb1	60	205.8	71.7	0.17
Nel41	DB14Ab2	120	209.2	50.6	
Nel38	DB50Ba1	120	178.1	64.1	0.23

Table 3.1: Conditions and results for rock mechanics experiments on the quartzite (Table 3.1a) and the fault rock (Table 3.1b).

RESULTS

Strength

The maximum differential stress, $\Delta\sigma_u = \sigma_1-\sigma_3$, is linearly related to the confining pressure (Fig. 3.10a), corresponding to a Mohr-Coulomb failure envelop. The strength of samples loaded under high confining pressures, 200 MPa for the quartzite and 120 MPa for the cataclasite, deviate from linearity (Fig. 3.10a) and are not incorporated in the linear regression. The quartzite has uniaxial strength of 207 MPa, and the cataclasite has uniaxial strength of 99 MPa. The failure strength data can be represented by Coulomb criterion with cohesion, C, and the angle of internal friction, φ, following the relation:

$$\tau = C + \sigma_n tan\varphi$$

where τ and σ_n are the shear stress and the normal stress respectively, on the fault plane at failure. C and φ are; C = 49 MPa and φ = 39° for the quartzite, and C = 29 MPa and φ = 29° for the cataclasite.

Elastic properties

Young's modulus (Fig. 3.10b) is calculated from the strain gage readings or, in experiments without stain gages, from load cell readings, corrected for machine stiffness. Young's modulus gently increases with confining pressure. The two data points for the cataclasite at confining pressures of 20 and 60 MPa (Nel35 and Nel36, Table 3.1) are not incorporated in the linear relation, since during these experiments oil leaked through the plastic jackets near the gages. The average Young's modulus for quartzite and cataclasite is 77 GPa and 52 GPa respectively.

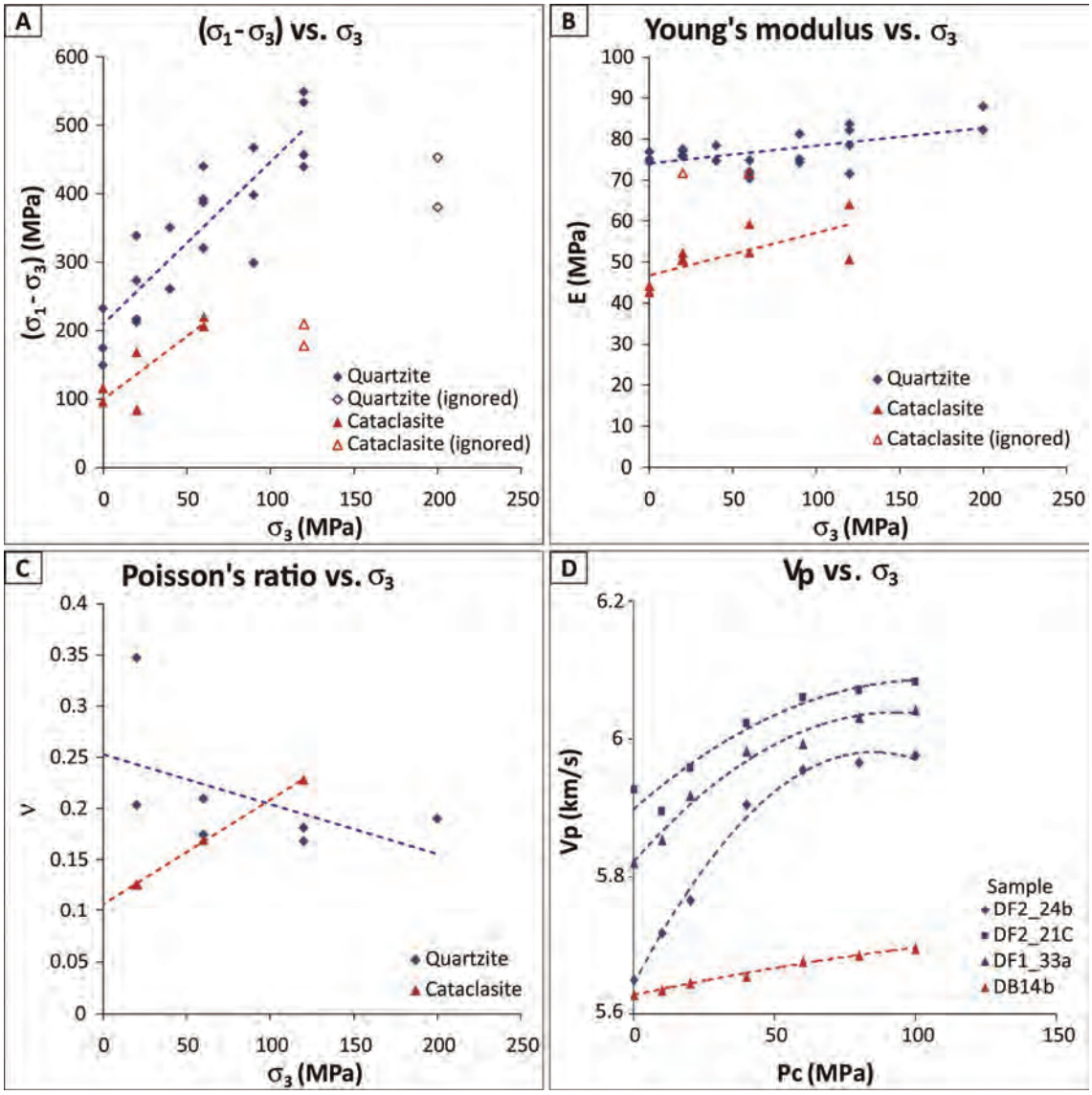

Figure 3.10: Main results of the rock mechanics experiments. (A) Maximum differential stress at failure vs. confining pressure for the quartzite (blue) and cataclasite (red), displays linear relations. The strength under high confining pressure, 200 MPa for the quartzite and 120 MPa for the cataclasite, deviate from linearity. The linear relation between the differential stress and confining pressure, in MPa, for the quartzite and cataclasite is given by $\Delta\sigma_u = 2.39\sigma_3 + 207.3$ and $\Delta\sigma_u = 1.85\sigma_3 + 98.6$ respectively. (B) Young's modulus (E) vs. confining pressure. Average E for the quartzite and cataclasite are 77 GPa and 52 GPa respectively. (C) Poisson's ratio vs. confining pressure with an average ratio of 0.21 for the quartzite, 0.23 for the cataclasite. Due to oil leakage at the strain gage, the measurements for 20 and 60 MPa are ignored.(D) P-wave velocities (V_P) vs. confining pressure. Three quartzite samples (blue) with maximum values of 5.98 to 6.08 km/s. The cataclasite sample (red) with velocity to a maximum of 5.69 km/s.

Poisson's ratio varies with the confining pressure (Fig. 3.10c). The quartzite displays a decrease with increasing confining pressure and an average Poisson's ratio of 0.21. Poisson's ratio of the cataclasite is 0.23 based on one sample (experiments at 20 and 60 MPa confining pressure are ignored).

P-wave velocity

P-wave velocities were measured for three 1x1 inch cylindrical quartzite samples and one 1x1 inch cubic cataclasite sample. The first arrivals of a voltage pulse were measured at confining pressures of 10, 20, 40, 60, 80 and 100 MPa, using an oscilloscope at frequency of 10 MHz.

The V_P of the quartzite increases significantly with confining pressure, to maximum values of 5.98 to 6.08 km/s (Fig. 3.10c). This V_P increase suggests wide-spread crack closure within the samples. The cataclastic sample displays only minor increase of V_P with increasing confining pressure, suggesting negligible crack closure; the maximum V_P for the cataclasite is 5.69 km/s.

DAMAGE ANALYSIS

The increase in V_P with increasing confining pressure in the quartzite was the first indication that the quartzite is internally damaged, and that this damage can be manifested by inelastic strain. Determination of the inelastic strain for the seven experiments with strain gages was done by subtracting the calculated elastic strain from the total measured strain following the method of Katz and Reches (2004). Considering the Poisson's effect and Hooke's law, the axial elastic strain, $(\varepsilon_{zz})_{elast}$, and the circumferential elastic strain, $(\varepsilon_{xx})_{elast}$, can be calculated from the following relationships:

$$(\varepsilon_{zz})_{elast} = \frac{1}{E}\left[\sigma_{zz} - \nu\left(\sigma_{xx} + \sigma_{yy}\right)\right]$$

$$(\varepsilon_{xx})_{elast} = \frac{1}{E}\left[\sigma_{xx} - \nu\left(\sigma_{yy} + \sigma_{zz}\right)\right]$$

where E and ν are the Young's modulus and Poisson's ratio respectively and are derived for the state of linear stress / strain relationships. For rock mechanics experiments under constant confining pressure, σ_{xx} and σ_{yy}, which are initially held constant during deformation, may be ignored (Katz and Reches, 2004), reducing the above equations to:

$$(\varepsilon_{zz})_{elast} = \frac{\sigma_{zz}}{E}$$

$$(\varepsilon_{xx})_{elast} = -\frac{\nu\sigma_{zz}}{E}$$

The inelastic strain, $(\varepsilon)_{inelast}$, is calculated by subtracting the elastic strain, $(\varepsilon)_{elast}$, from the total experimental strain $(\varepsilon_{zz})_{total}$ following the method of Katz and Reches (2004):

$$(\varepsilon_{zz})_{inelast} = (\varepsilon_{zz})_{total} - (\varepsilon_{zz})_{elast}$$

$$(\varepsilon_{xx})_{inelast} = (\varepsilon_{xx})_{total} - (\varepsilon_{xx})_{elast}$$

The inelastic strains of the seven quartzite samples are illustrated in Fig. 3.11. Negative strain on the right represents the axial strain ε_{xx}, positive strain on the left represents the circumferential strain ε_{zz}. The axial and circumferential elastic strains are also illustrated by the dashed lines. The axial inelastic strain is generally smaller than the elastic strain, with maximum values up to 0.8% for high confining pressures. The circumferential inelastic strain reaches strains > 1% for high confining pressures, significantly larger than the circumferential elastic strain of < 0.4%. This suggests significant damage of the quartzite samples before failure, by dilation, along axis-parallel micro-fractures.

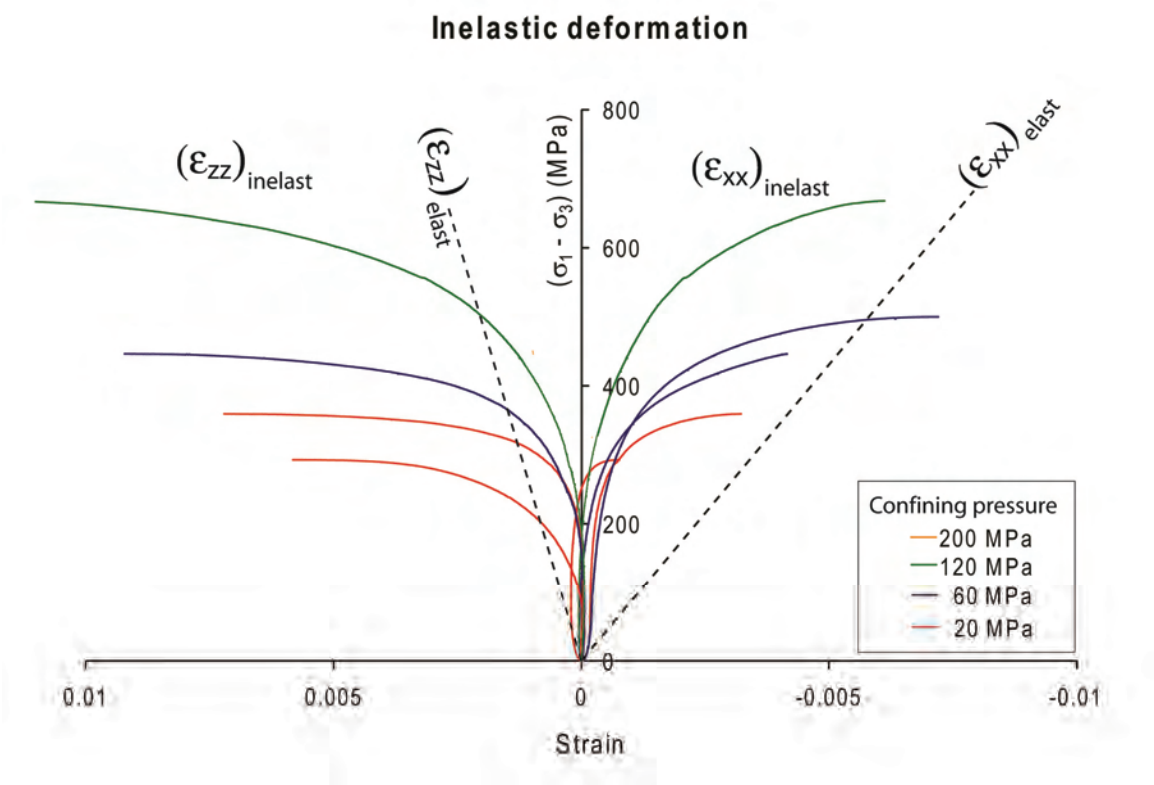

Figure 3.11: Calculated inelastic deformation for seven quartzite samples. The right represents the axial strain ε_{xx} vs. differential stress, on the left the circumferential strain ε_{zz} (positive). Dashed lines represent the calculated elastic strain. Calculated axial inelastic strains $(\varepsilon_{xx})_{inelast}$, plotted for experiments at confining pressures of 20, 60, 120 and 200 MPa, generally remain smaller with respect to the axial elastic strain, with maximum axial inelastic strains of 0.8% for high confining pressures. The circumferential inelastic strain, $(\varepsilon_{zz})_{inelast}$, is significantly larger, with values > 1% for high confining pressure, than the circumferential elastic strain of < 0.4%.

The damage of the samples was quantified by evaluating the deformation modulus, which is the local slope of the stress-strain curve (Katz et al., 2001). Figs. 3.12a and 3.12b illustrates the axial and volumetric strain curves for experiments on quartzite (sample Nel08) and cataclasite (sample Nel35), both under 20 MPa confining pressure. The quartzite samples undergo significant strain-hardening before failure with significant volumetric strain into the extensional (positive) strain field. The cataclasite behaves linearly elastic without significant strain hardening or volumetric strain, with failure occurring at significant lower strains and stresses (note the scale difference in Fig. 3.12).

Fig. 3.12c displays the deformation modulus for both rock types against strain, normalized for strain at failure, after Katz et al. (2001). The deformation modulus decreases significantly for the quartzite after 20% of the total strain, with values dropping from ~80 GPa to below 10 GPa. This trend of the deformation modulus is similar to the behavior of Mount Scott granite described by Katz and Reches (2004), who showed that this damage is associated with formation and dilation of micro-fractures. The deformation modulus of the cataclasite decreases only slightly with increasing strain, indicating that it behaves more brittle by with less damage, with respect to the stronger and more damaged quartzite.

The main fault-zone that developed within quartzite samples is a few mm wide zone of complex fault-branches, along which white ‘rock flour’ is generated (Fig. 3.13). The rock flour has a similar appearance as observed along the M2.2 rupture. The main fault-zone within cataclasite samples typically generates a narrow zone, less then1 mm thick, with only very few branches, along which minor amounts of white rock flour is generated.

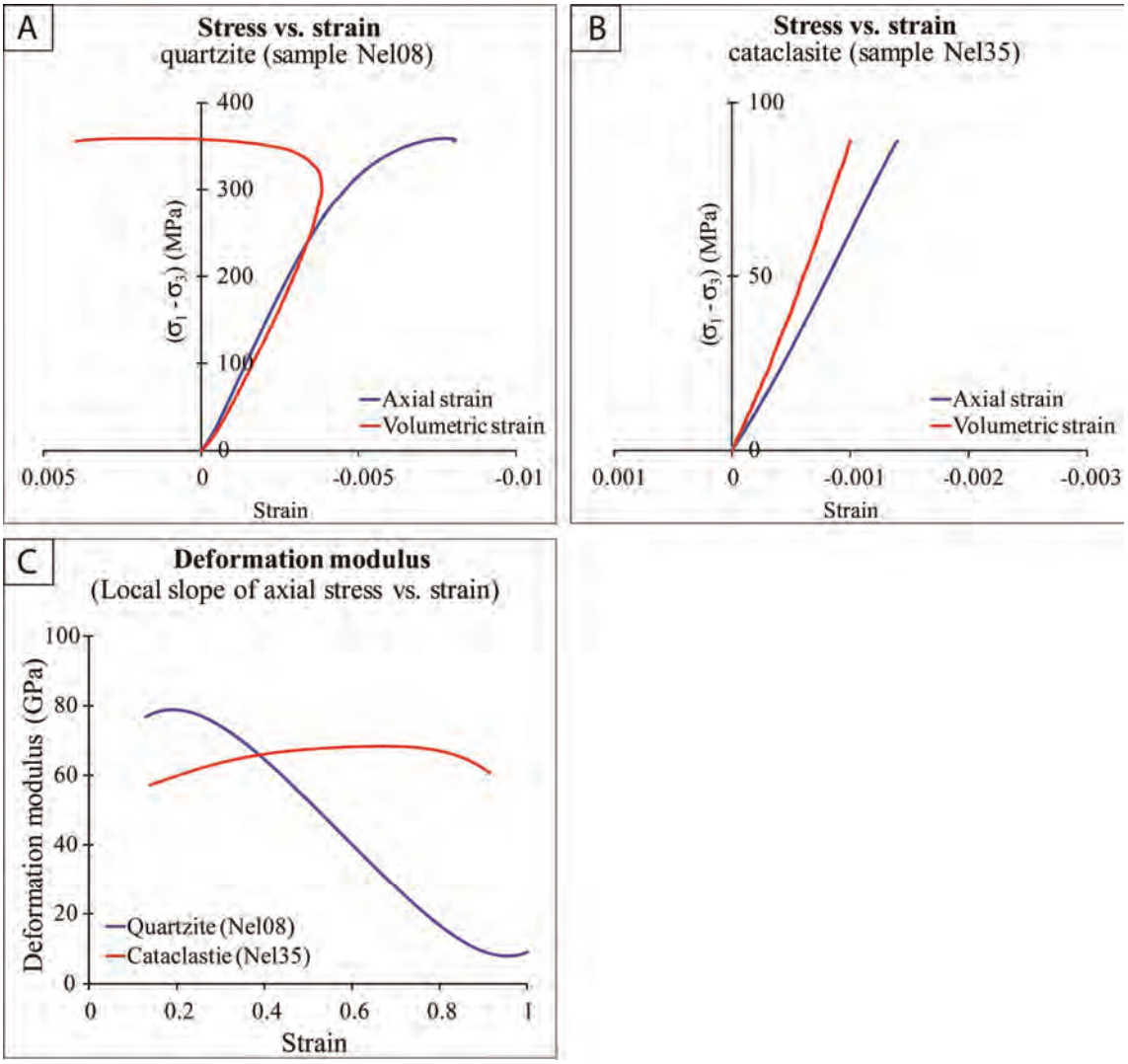

Figure 3.12: Characteristic results for the experiments, under confining pressure of 20 MPa. (A) Differential stress vs. strain for quartzite sample Nel08 displays strain hardening before failure (blue) with significant volumetric strain (red) into the extensional (positive) strain field. (B) Differential stress vs. strain for cataclasite sample Nel35 displays linear elastic behavior without strain hardening and only minor volumetric strain (compressive). (C) Deformation modulus for both the quartzite (Nel08) and cataclasite (Nel35) after Katz et al. (2001). The deformation modulus for the quartzite decreases significantly with increasing strain, starting at 20% of the total strain, from 80 to 10 GPa. The deformation modulus of the cataclasite decreases only slightly at 80% of the total strain.

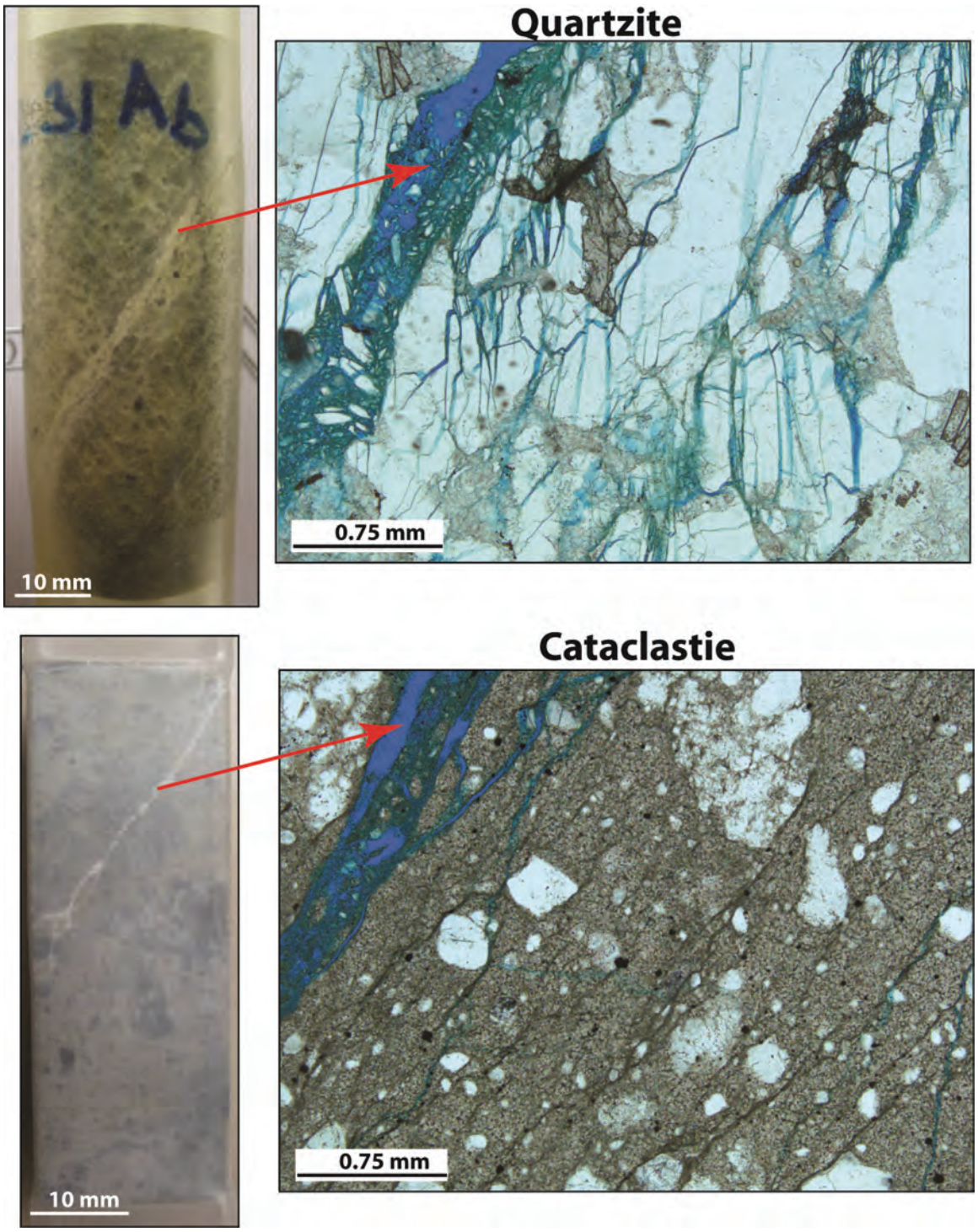

Figure 3.13: Damage within samples after experiments under 20 MPa confining pressure. The quartzite displays significant off-fault damage highlighted by the blue epoxy that filled the micro-fractures. Branches from the main fault die out within axial fractures within quartz grains. The cataclasite displays a narrow fault with minor off-fault damage. The main fault developed parallel to the poorly developed foliation within the matrix. Thin sections are displayed in plane-polarized light.

The extensive damage in the quartzite, and it relation to the formation of micro-fractures, is observed in thin sections of the failed samples for both rock types after experiments under 20 MPa confining pressure (Fig. 3.13). Significant numbers of off-fault micro-fractures (blue epoxy) appear in the quartzite, with multiple branches from axial fractures into individual quartz grains. These axial fractures form during loading and contribute to the strain-hardening and volumetric expansion of the sample. On the other hand, thin sections of the cataclasite display a narrow fault-zone with only minor off-fault damage (no blue epoxy). Quartz clasts within the cataclasite remain undamaged and no axial fractures are observed. The main fault within the cataclasite developed parallel to the ancient foliation within it (Fig. 3.13).

TESTING THE CONTACT OF QUARTZITE-CATACLASITE

A single experiment was conducted on an oversized sample (12.7 x 4.27 cm) that contains the cataclasite in contact with the quartzite. The contact is oriented at 33° to the long axis of the sample. The experiment was conducted under a confining pressure of 60 MPa. Fig. 3.14 illustrates thin sections through the sample after failure. The main fracture developed dominantly along the contact of the quartzite and the cataclasite (Figs. 3.14a and 3.14b). It consists of a zone of branching secondary fractures that dies out into axial fractures within single quartz grains, as displayed in close-ups of the thin section (Figs. 3.14c and 3.14d). Significant off-fault damage occurs within the quartzite forming axial fractures within the grains, that eventually link together to form through going fractures, near the contact with the cataclasite. The cataclasite, though twice as weak as the quartzite, remains visually undamaged. The density of damaged and dilating quartz

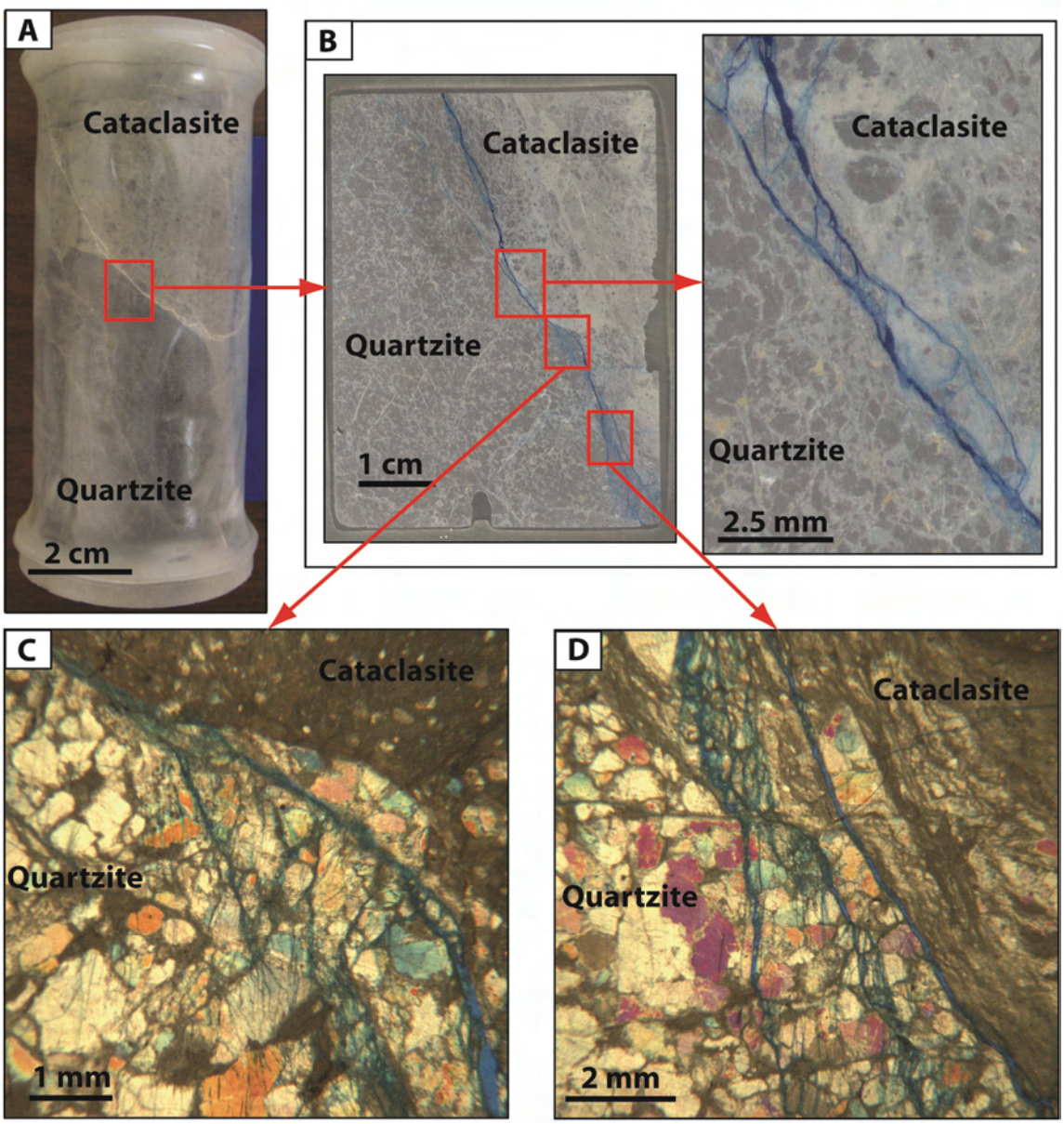

Figure 3.14: Section through the sample with quartzite-cataclasite contact. The experiment was done under 60 MPa confining pressure. The sample size is 12.7 x 4.27 cm. (A) The sample after failure, displays development of white rock flour, dominantly along the quartzite-cataclasite contact. (B) Oversized thin section displays localization of the main fault (blue epoxy) along the contact. The main fault displays several branching zones up to several mm thick. (C and D) Close-up of fault branches, with significant off-fault damage into the quartzite. Axial fractures within the quartz grains significantly increase towards the contact and link up to eventually form the main fault.

grains increases towards the main fracture, similar to the observations in the experiments of the quartzite samples (Fig. 3.13).

A striking similarity was noted with the field observations. Mapping the M2.2 rupture indicates that the rupture dominantly localized along the contact of the quartzite and cataclasite, characterized by generation of rock flour (Figs. 3.5 and 3.6), while damage within the cataclasite was rarely observed. The experiment described above displays similar localization of slip at the contact (Fig. 3.14a) with the generation of white rock flour along branching faults. Thin sections display increasing damage by axial fractures within quartz grains, towards the main fracture (Fig. 3.14), while the cataclasite remains visually undamaged. This suggests that the white rock flour, with similar appearance as observed along the M2.2 rupture, results from failure of the quartzite and that a similar mechanism controls the localization of failure in both the field and experiments.

SUMMARY OF ROCK MECHANICS EXPERIMENTS

Experiments on 22 quartzite samples and 8 cataclasite samples from within the Pretorius fault reveal that the quartzitic host rock, with $E = 77$ GPa and $\nu = 0.21$, is about twice as strong as the cataclastic fault rock, with $E = 52$ GPa and $\nu = 0.23$. The quartzite displays significant strain-hardening with associated dilation by micro-fractures, where the cataclasite is more brittle with no apparent micro-fracture damage. The contact between the quartzite and cataclasite, tested in one experiment, displays similar localization of failure at the contact as was observed in the field, with major damage of the quartzite near the contact and only minor visible damage within the cataclasite.

MECHANISM OF SLIP LOCALIZATION

CONCEPT

A 2D finite element model (FE) was developed to investigate the role of mechanical heterogeneity within the Pretorius fault on slip localization processes. Underground observations of the M2.2 rupture reveal that slip was localized along the contact between the quartzitic host rock and the cataclasite of the pre-existing Pretorius fault. The mechanisms leading to this localization remain unclear from field observations. The rock mechanics experiments on the cataclasite and the quartzite within the fault-zone indicate a mechanical difference between the brittle, linear elastic cataclasite and the stronger, less brittle, quartzite with strain-hardening due to micro-fracturing. A 2D FE model was used to investigate how the presence of this mechanical contrast affects the stress and strain distribution along idealized fault geometry, and if it control mechanisms of slip localization.

FE MODEL

In the model, a pre-existing segment of the Pretorius fault is idealized by a thin elongated elliptical inclusion, with an aspect ratio of 1:0.02, embedded in a medium with dimensions of 100 x 100 meters. The long axis of the ellipse is oriented at 45° to the x-axis (Fig. 3.15a). The material properties assigned to the medium and embedded ellipse reflect the properties derived from the rock mechanics experiments on the samples within the Pretorius fault. The ellipse is modeled by an isotropic linear elastic material with $E = 77$ GPa and $\nu = 0.23$. The strain-hardening of the quartzite is modeled by a combination

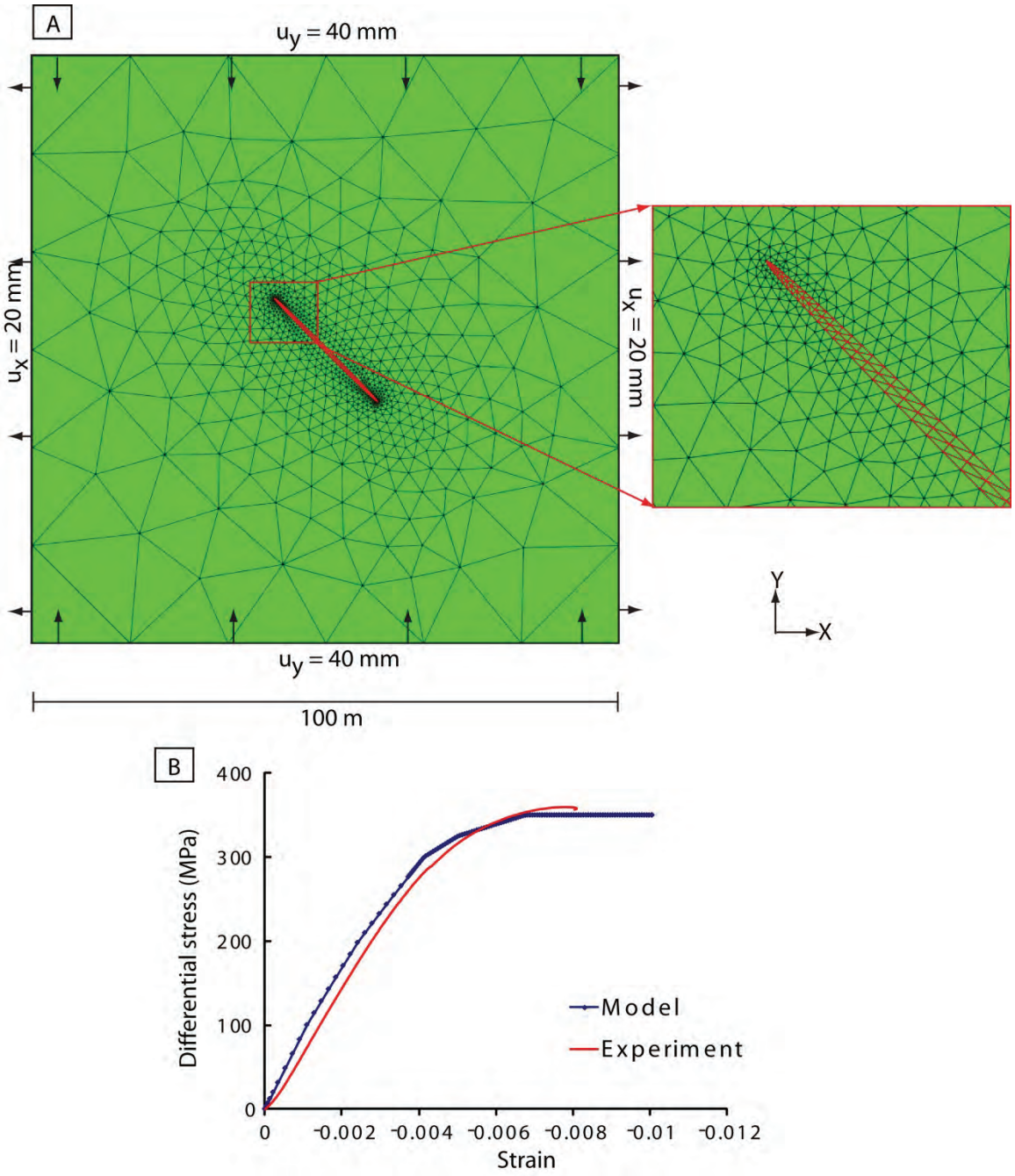

Figure 3.15: 2D FE model, with idealized elliptical fault geometry. (A) The dimensions and boundary conditions of the model. The elongated ellipse is oriented 45° with respect to the x-axis. The 3-node linear plane strain triangular mesh is refined towards the ellipse and towards the tips of the ellipse. Boundary displacement of 0.8% shortening in the x-direction and 0.4% extension in the y-direction is applied to generate shear along the ellipse. (B) Stress vs. strain relation between elements away from the elipse (blue) and rock mechanics experiments on sample NEL08 (red).

of isotropic elastic material with isotropic plastic hardening. Yield stresses with associated plastic strain values are determined from the rock mechanics stress-strain curves to simulate the experimental results up to the point of failure. The post-peak behavior of the quartzite is ignored in this analysis, and modeled by perfect plastic behavior for maximum stress of 350 MPa. There is a fit between the stress-strain relation for the medium, away from the ellipse, and the quartzite from rock mechanics experiments (Fig. 3.15b).

Arbitrary generic plane-strain displacement boundary conditions are applied on the edges of the medium with 0.8% shortening in the x-direction and 0.4% extension in the y-direction. The displacement field in combination with the orientation of the ellipse generates shear stresses along the edge of the ellipse.

The model uses a 3-node linear plane strain triangular mesh was used with reduced mesh size towards the tips of the elliptical inclusion. The problem is solved in Abaqus/CAE Standard solver (Student edition V 6.7) in 100,000 incremental time steps.

MODEL RESULTS

The investigation focused on the effects of non-linear behavior of the medium (quartzite) on the stress and strain distribution in the vicinity of the ellipsoidal fault (cataclasite). The total plastic shear strain parallel to the axis of the elliptical inclusion, though time, represents the permanent shear strain along the fault (Fig. 3.16). Away from the inclusion, the plastic shear strain increases homogeneously with increasing displacement. Towards the ellipse however, the plastic shear strain increases locally, reaching strains of 1.1×10^{-2}. This value is about 20% higher than the plastic shear strain away from the inclusion. Fig. 3.17a displays the total fault-parallel plastic shear strain,

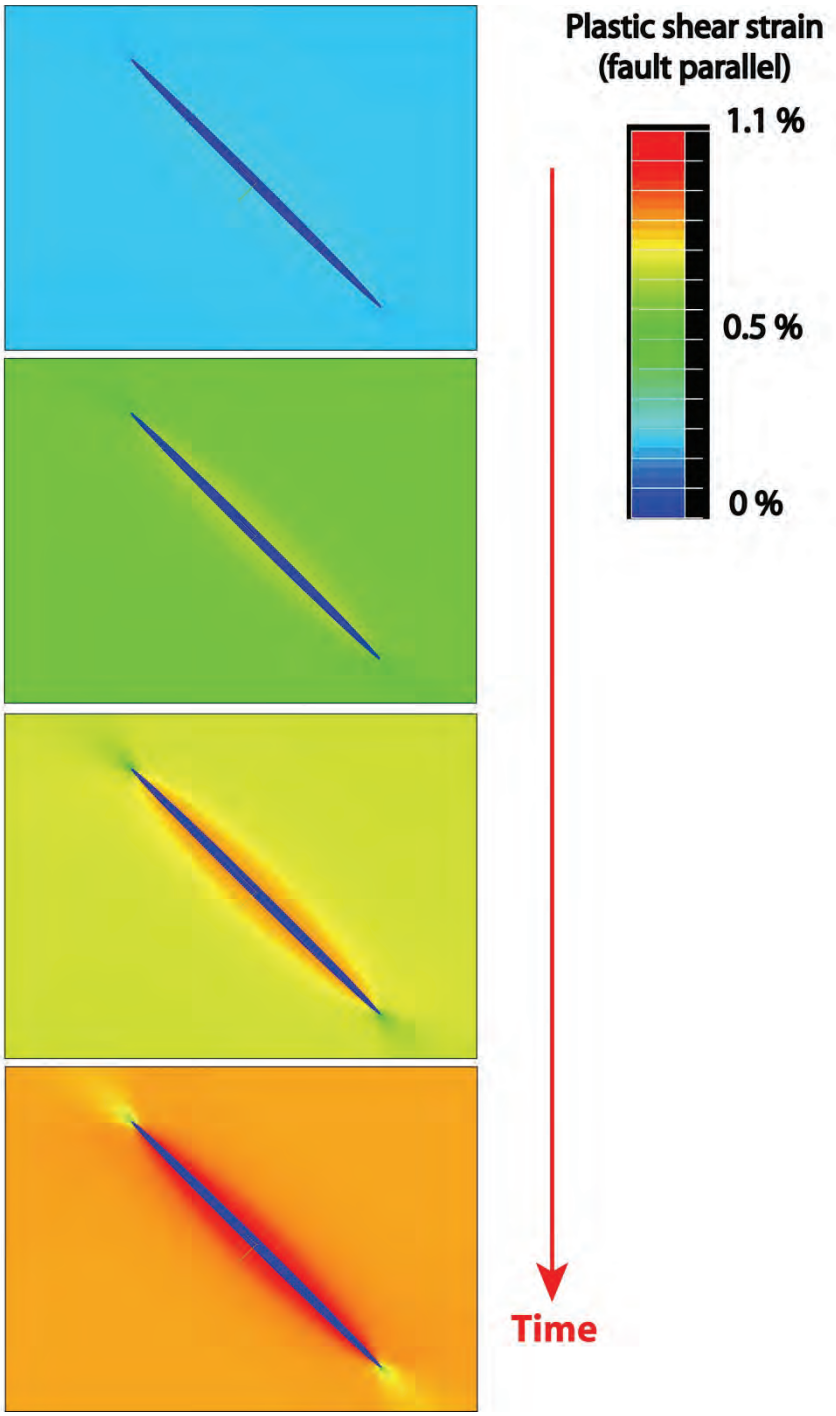

Figure 3.16: Plastic shear strain, parallel to the axis of the elliptical inclusion, though time. Towards the ellipse, the plastic shear strain increases locally, reaching strains of $1.1x10^{-2}$. This value is about 20% higher than the plastic shear strain away from the inclusion. Time steps displayed here are of ~25,000 increments of the total displacement.

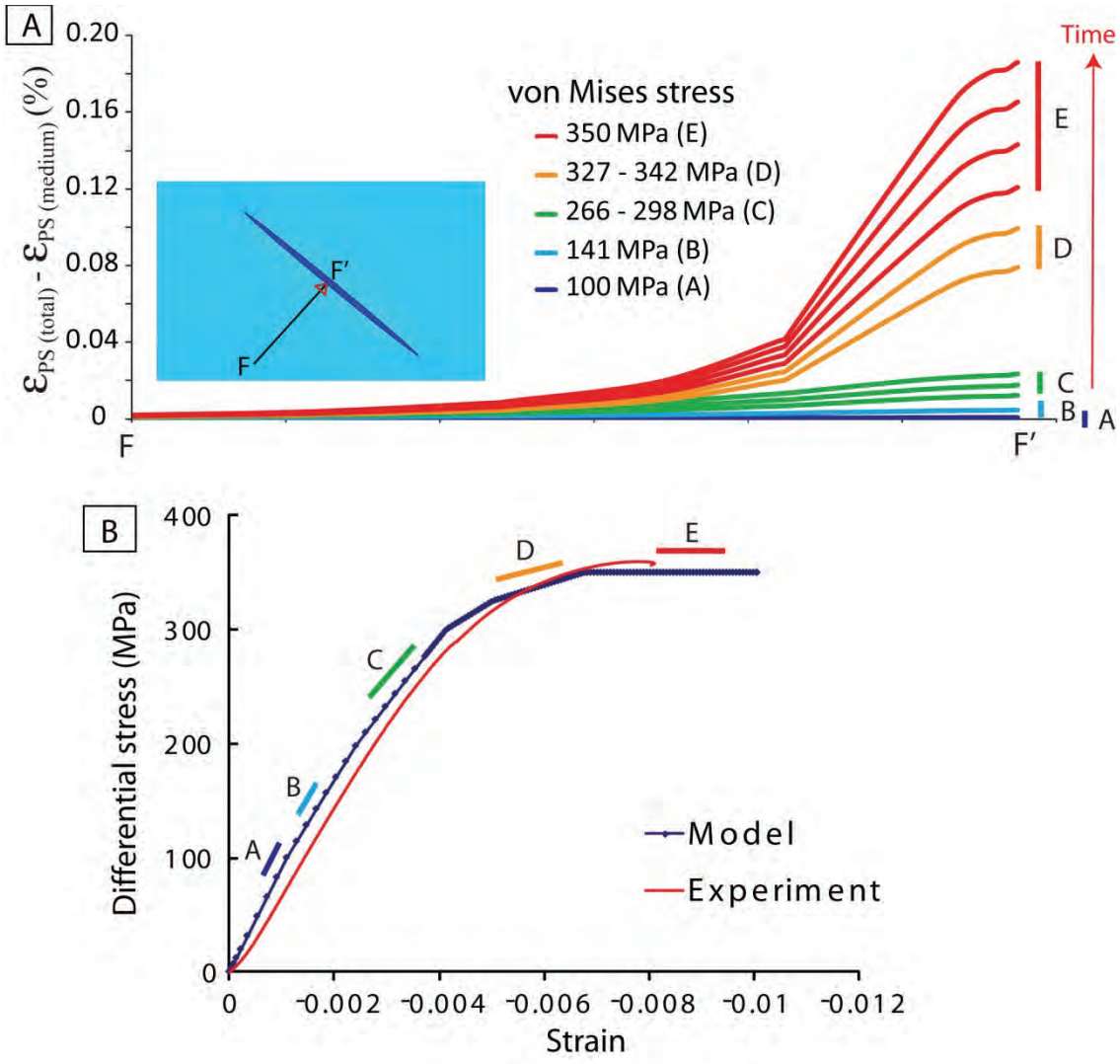

Figure 3.17: Mechanism of strain localization. (A) Total fault-parallel plastic shear strain, $\varepsilon_{ps(total)}$, minus the fault-parallel plastic shear strain of the medium, $\varepsilon_{ps(medium)}$, away from the elliptical inclusion, along profile F-F'. The individual lines represent 10,000 time increments of the total displacement. The associated Mises stress for each group A to E is giving. The plastic shear strain localizes towards F', which represents the edge of the ellipse. (B) Stress vs. strain relation between elements away from the ellipse (blue) and rock mechanics experiments (red). The groups A to E correspond to different stages of strain hardening.

$\varepsilon_{ps(total)}$, minus the fault-parallel plastic shear strain of the medium, $\varepsilon_{ps(medium)}$, away from the elliptical inclusion, along profile F-F', with F' located at the edge of the ellipse. Different lines represent time steps of 10,000 increments of total displacement, during which the plastic shear strain localizes towards the elliptical inclusion. For every group, A through E, the associated von Mises stress within a single element, located at the edge of the inclusion (highlighted near F' in Fig. 3.17a), is specified. The relationship of these groups to the mechanical behavior of the medium is indicated in Fig. 3.17b. Within the model, no mechanism is specified for strain hardening by plasticity. The rock mechanics experiments, however, reveal that strain hardening is associated with growth of micro-fractures within the grains of the quartzite that develop into axial fractures within the grain and eventually link up to contribute to macroscopic failure (Figs. 3.13, 3.14C and 3.14D). Groups A to E are interpreted to coincide with the following processes observed in the quartzite (Fig. 3.17):

A) Group A represents the linear-elastic behavior of the medium, without the onset of plasticity.

B) Group B represent the initiation of plasticity, with minor localization of plastic shear strain at the edge of the ellipse, coinciding with stable growth of micro-fractures.

C) Group C represents the increase of strain hardening, during which micro-fractures grow to develop axial fractures, causing dilation of the quartzite, results in increase of localization of ε_{ps} along the edge of the ellipse.

D) Group D corresponds to significant strain hardening by unstable crack growth, close to failure. Most of the localization occurs during this stage (Fig. 3.17a).

E) Post-peak behavior (Group E in Fig. 3.17), is defined by perfect plasticity at stress of 350 MPa within the model (Fig. 3.17b), representing permanent shear strain along a macroscopic fault. During this stage, the fault-parallel shear strain continues to localize at the edge of the inclusion (Fig. 3.17a).

MAIN FINDINGS FOR THE MECHANISM OF SLIP LOCALIZATION

The model reflects the contrast of the mechanical properties of the Pretorius fault and demonstrates that the difference in mechanical behavior could lead to strain localization and failure near the bi-material interface. The onset of localization occurs before failure and is directly related to strain hardening processes within the damaged zone. Thus, strain hardening within damaged host rock effectively controls nucleation and slip localization as observed in the M2.2 event that reactivated the Pretorius fault.

DISCUSSION AND CONCLUSION

EARTHQUAKE RUPTURE ZONE

The characteristic features of the M2.2 2004 rupture zone in TauTona mine are discussed in relation to similar observed structures observed along ruptures in South African mines. As mentioned in the Introduction, the present study provides a rare opportunity to analyze the rupture zone of a single earthquake along a major fault at focal depth. Other studies that address a similar situation include the analyses of the M4.6, Matjhabeng earthquake, 1999, along the Dagbreek fault, Welkom, South Africa (Dor et al., 2001). This event displaces rock bolts up to a distance of 30 - 45 m from the main Dagbreek fault, indicating a wide rupture zone, mainly within intact rock. This zone is

characterized by several fine grained and/or clayey, soft fresh gouge zones of 0.5 – 5 cm thick that characterize individual slip surfaces of the M4.6 rupture.

The M2.2 event reactivated an ancient fault that has been dormant for at least 2 Ba. Furthermore, the region of the Western Deep had subsided at least 10 km (Gibson et al., 2000b) and underwent low-grade thermal metamorphism, as well as hydrothermal alteration (Robb et al., 1997). All these events are likely to strengthen the Pretorius fault-zone and to lithify its fault rocks; these processes could eliminate the effects of the original deformation associated with slip along the fault. The initial examination of the Pretorius fault and its cataclasite zones suggested that this fault-zone will fail like an intact rock body and its rupture zone will be similar to a new fault. This suggestion is based on rock mechanics tests that indicate that the cataclasite of the Pretorius fault had re-strengthened to ~50% of the host quartzite strength (Fig. 3.10). The M2.2 rupture differs from our expectations as follows (see detailed descriptions above):

1) Observed: Almost the entire slip occurred along pre-existing segments (Figs. 3.3 – 3.6).

   Expected: Many new fractures across intact rock.

2) Observed: The slipping segments are fairly planar (Fig. 3.3 – 3.5 and 3.6).

   Expected: Most segments should be complex and branching; however, complex networks with multiple small fractures of tensile (Fig. 3.7) or shear character (Figs. 2.8 and 3.8) appear only locally.

3) Observed: The slipping segments are not parallel to each other (Fig. 3.3).

   Expected: Sub-parallel segment that conform the present stress field.

4) Observed: Slip is associated with the formation of gouge layers in thickness from ~ 1 mm to 5 mm composed of fine-grain rock flour (Fig. 3.5 and 3.6).

   Expected: As observed: Rock-flour is common to the failure of the quartzite in South African mines (Dor et al., 2001; McGarr et al., 1979; Olgaard and Brace, 1983; Ortlepp, 2000; Stewart et al., 2001) and in our lab experiments.

5) Observed: Slip is localized along the contacts between the cataclasite of the ancient fault segment and the quartzitic host rock (Figs. 3.3 - 3.6).

   Expected: Such localization was observed in present rock-mechanics experiments (Fig. 3.14) and several previous works, (e.g., Engelder, 1974).

The most surprising observation, and probably the most important one, is that slip was localized along preexisting segments, even though the fault was dormant for very long period. Our rock mechanics experiments and the following finite element modeling, which were described earlier in this chapter, provide a solution to this apparent paradox. The experiments illustrate that the cataclasite is relatively weak and highly brittle, whereas the host rock is relatively strong and with plastic-damage rheology. The juxtaposition of these two rock properties at the quartzite-cataclasite boundary leads to plastic strain localization in the host rock at the contact (Fig. 3.16), and possible failure in the brittle cataclasite (Fig. 3.17). One conclusion is that the mechanical heterogeneity within the Pretorius fault-zone effectively controls the slip localization, and possibly nucleation, during the event. As mechanical heterogeneities are common within fault-zones, (e.g., Caine, 1996) one can postulate that these heterogeneities, and not necessarily the absolute strength, control the localization and reactivation of the preexisting segments.

The significance of the local stress field and the formation of rock flour are discussed in Ch. 4.

Chapter 4:

Stress and Energetics of the M2.2 Event, TauTona Mine, South Africa

INTRODUCTION

The M2.2 earthquake reactivated several segments of the Pretorius fault-zone in TauTona mine, South Africa, as described in Ch. 3. This chapter focuses on the stress field associated with the rupture and the energy balance of this event.

The constraint on the state of stress at fault-zones is central to the understanding of earthquake mechanics (Scholz, 2002). Faulting theories (Anderson, 1951) that are based on laboratory observations are commonly applied to upper crust faults, even though the stresses close to active faults are poorly constraint (Zoback et al., 1987). The state of stress in the vicinity of active faults was estimated from borehole failures and earthquake inversion (Hickman and Zoback, 2004; Townend and Zoback, 2004; Yamamoto et al., 2000; Zoback et al., 1987; Zoback et al., 1989). Yet, stress data close to active fault are relatively rare, and often the state of stress is interpolated from far-field measurements. The first part of this chapter presents the stress state in TauTona mine based on borehole failure observations; some of the boreholes are located as close as 60 m to the rupture zone of the M2.2 earthquake.

The second part of this chapter focuses on the estimation of the energy balance of the M2.2 earthquake along the Pretorius fault by means of combined seismic data, 3D rupture geometry (Ch. 3), and stress measurements (first part of this chapter). The energy balance of an earthquake is usually based solely on seismic measurements (e.g., Kanamori, 2004). It is generally impossible to verify the seismological results with direct

geological observations of the rupture zone at focal depth. Wilson et al. (2005) calculated the fracture energy associated with an earthquake by using the surface area of gouge generated along the San Andreas Fault and during the M3.7 event that formed a new fault in Hartebeestfontein gold mine, South Africa. They concluded that the fracture energy, invested to form gouge powder, is approximately equal to the frictional heat energy that can be estimated from shear stress and total slip. Chester et al. (2005) analyzed the fracture energy along the Punchbowl fault, an inactive exhumed segment of the San Andreas system, with estimated 44 km of displacement. They found a total fracture energy of 700 MJ/m^2 during an estimated 10,000 earthquakes, resulting in 0.07 MJ/m^2 for a single earthquake. Ma et al. (2006) estimated the energetics of the M7.7 Chi-Chi earthquake along the Chelungpu-fault, Taiwan. They estimate 4.3 MJ/m^2 of fracture energy from the 2-cm MSZ, which accommodated estimated 6-7 earthquakes, resulting in 0.65 MJ/m^2 for a single earthquake, contributing about 6% to the earthquake breakdown work. Although this analysis combined seismic data with geological observations, it has limited observations of slip surface geometry, observed within a drilling core.

RUPTURE ZONE OF THE M2.2 EARTHQUAKE, 2004

THE PRETORIUS FAULT

The present study is conducted in the TauTona mine, located in the Western Deep Levels of the Witwatersrand Basin, South Africa (Fig. 3.1). The tectonic setting of the study area and the structure of the Pretorius fault-zone were presented in Chapter 2; the characteristics of the rupture zone of the M2.2 event were presented in Chapter 3. Only their main features are outlined here.

The Pretorius fault is a 10 km long, ENE trending, oblique, right-lateral fault forming a sub-vertical fault-zone (Ch. 2). The fault has right-lateral displacement of about 200 m, and vertical displacement of 30-100 m. In TauTona mine, the fault cuts a sequence of quartzitic rocks. The fault-zone itself has a complex structure with tens of segments that form a 25 – 30 m wide network of cross-cutting and anastomosing faults and fractures (Ch. 2). The segments are dominantly east-west striking, steeply dipping (40°-90°), quasi-planar surfaces that crosscut, intersect and branch from each other. Some of the segments are activated bedding surfaces that dip ~22° southward. Most of the segments contain a massive, highly cohesive and green to gray quartzitic cataclasite that varies in thicknesses from a few millimeters to tens of centimeters (Ch. 2). This cataclasite contains abundant clasts of light gray to dark gray, fine to very coarse grained quartzite up 0.5 m in diameter.

MAIN FEATURES OF THE RUPTURE-ZONE

On December 12, 2004, an M2.2 event reactivated part of the Pretorius fault. The rupture-zone of this event was recognized by (Ch. 3): (1) intense local damage to a few tunnels; (2) formation of fresh, white gouge (rock flour) along several segments in the fault-zone; and (3) displacement of rock-bolts that were intersected by the slipping fault segments. The rupture-zone was mapped in two setting: in tunnels that were excavated prior to the events and in a tunnels that was excavated through the rupture-zone about six months after the events. A cross section of the structure of the rupture, including its trace within the 120-MM-tunnel, is illustrated in Fig. 3.3. The main features of our three-dimensional mapping (Ch. 3) are the following:

1. Slip occurred along four large, quasi-planer, preexisting segments of the Pretorius fault (Fig. 3.3)
2. Slip, as identified by the presence of zones of fresh gouge, was almost exclusively localized along the contacts between the cataclasite in the ancient segment and the host rock (Figs. 3.4, 3.5 and 3.6, Ch. 3).
3. Locally, the slipping segment display complex networks with multiple small fractures of tensile (Fig. 3.7, Ch. 3) or shear character (Fig. 2.8 and 3.8, Ch. 3).
4. Maximum measured shear displacement was 25 mm in oblique, normal slip.
5. Gouge zones range in thickness from ~ 1 mm to 5 mm at a given position. These values indicate wear-rates of at least 0.4 $mm^3/N{\cdot}m$. Wear-rate is calculated here by [(volume of wear products) / (area of sliding surfaces)] / [normal stress ·slip distance].

IN-SITU STATE OF STRESS

The perturbations of the in-situ stress field by large scale mining activities at depths down to 3.6 km are the main source for seismic activity in the mines. McGarr et al. (1975) showed that most seismicity is directly related to significant stress perturbations at the mining face. The M2.2 rupture is located within an area of complex tunnel networks, only ~20 m underneath the mined reef (Fig. 2.2). Determination of the stresses associated with the M2.2 rupture requires the knowledge of the far field (regional) in-situ stress around TauTone mine, as well as the local stress field near the rupture. Constraining the far field stress forms an important part of the NELSAM program and improves the safety

within the mine as it can contribute to the prediction of stability during development of mining activities.

The regional in-situ stress at the TauTona mine was determined by borehole breakout observations within a sub-horizontal borehole drilled at 3.5 km depth. These data were analyzed in combination with boundary element modeling (Lucier et al., 2009). The local state of stress near the M2.2 rupture was determined from borehole breakouts in three vertical boreholes drilled at 3.6 km depth, as close as 60 m from the rupture-zone. The stress tensor is calculated by combining the borehole observations with the geometry of the rupture and boundary element modeling. Finally, this stress tensor was used to calculate the shear and normal stress associated with the M2.2 rupture.

REGIONAL IN-SITU STRESS

The Witwatersrand Basin forms part of the cratonic crust of South Africa. McGarr and Gay (1978) showed that the crust in South Africa is under a normal faulting regime such that $S_V \geq S_{Hmax} \geq S_{hmin}$. Locally, in TauTona mine, in-situ stress measurements where conducted in the shaft pillar at a depth of 2,361 m. The measurement were conducted following the overcoring technique (Cartwright and Walker, 2000). They found that the maximum principal stress (σ_1) deviated 20° from vertical, and plunged to the NNW with a vertical gradient of 36 MPa/km. The intermediate principal stress (σ_2) deviated 20° from horizontal in the SSE direction with a vertical gradient of 19 MPa/km. The minimum principal stress (σ_3) was nearly horizontal in the WSW direction with a vertical gradient of 10 MPa/km.

Far field stress determination

Lucier et al. (2009) estimated the regional stress state that is unaffected by mining operations. To do so, a 418 m long borehole image log was collected in a sub-horizontal borehole that was drilled at a depth of 3.5 km (LIC118 borehole in Fig. 4.1), several hundreds of meters from the active mining area. This borehole trends to the east and was logged with a Digital Optical TeleViewer camera (DOPTV made by Robertson Geologging, UK). Lucier et al. (2009) analyzed the borehole breakouts, starting at a measured depth of 35 m and continued throughout the entire length of the borehole (Fig. 4.1). A large scale rotation of the position of the boreholes and a change in borehole width occurs at 150 m depth. After this depth the orientation and width stay consistent, suggesting that the borehole reaches the far field stress (Lucier et al., 2009).

The stress field responsible for the observed breakouts within the LIC118 borehole was constrained by Lucier et al. (2009) following an iterative forward modeling with 3D boundary element modeling. The modeling was directed to examine the effects of mining geometry and the timing of active mining steps on the perturbation of the regional stress field. The results of this study (Fig 4.2) displays a well constrained regional stress field with the maximum principal stress (σ_1) deviated 0-20° from vertical, plunging towards the NNW and a magnitude gradient ranging from 26.7 to 27.3 MPa/km. The intermediate principal stress (σ_2) is inclined 0-20° from horizontal plunging towards an azimuth of 157° and 168° with a magnitude gradient between 21 and 26 MPa/km. The least principal stress (σ_3) is inclined 0-10° down from horizontal towards an azimuth between 235° and 258°, with a magnitude gradient between 12.9 and 15.5 MPa/km.

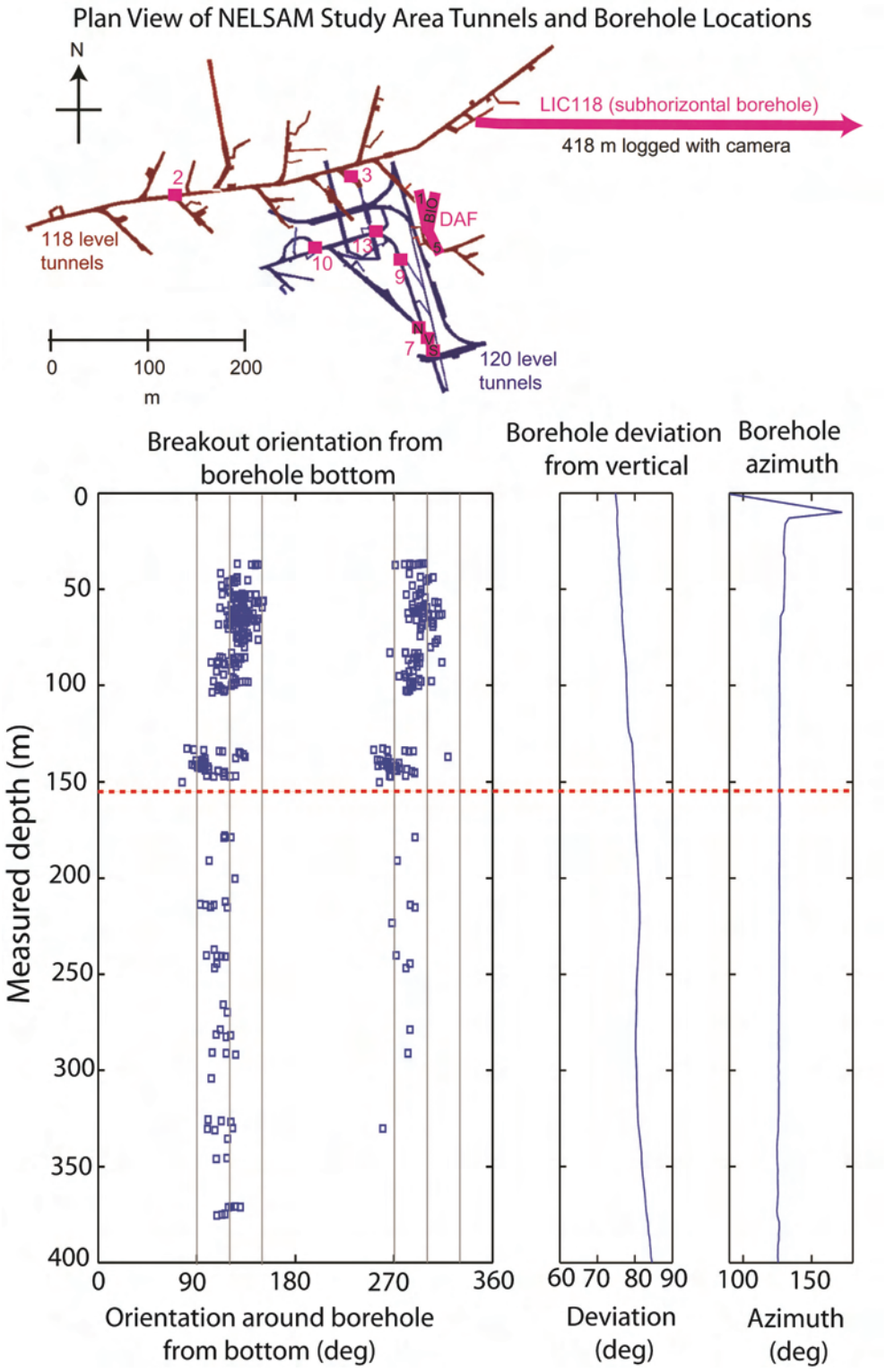

Figure 4.1: Borehole breakouts observed in 418 m of borehole image of LIC118, a sub-horizontal borehole drilled towards the east. Borehole breakouts are present from 35 m measured depth and continue for the entire borehole length. Large scale rotation and variation in width of the borehole breakouts occurs at a 150 m after which the orientation and width is consistent (Lucier at al., 2009)

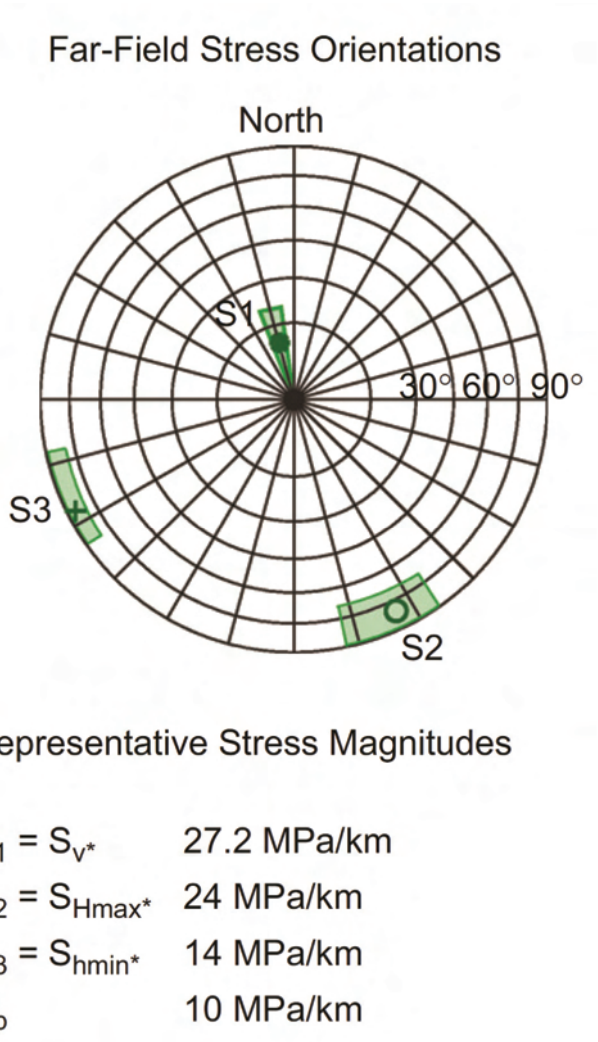

Figure 4.2: Orientations of the far-field stress and representative magnitudes. The range of acceptable principal stress orientations is illustrated in the green-shaded regions (Lucier et al., 2009).

This stress state is of normal faulting regime as suggested by McGarr and Gay (1978), with principal stresses that deviate slightly from vertical and horizontal, and with a maximum horizontal stress magnitude that approaches the vertical stress magnitude.

STRESS STATE CLOSE TO THE RUPTURE ZONE

Estimation of the local in-situ stresses in the region of the exposed rupture surface of the M2.2 event is based on borehole breakouts in shallow boreholes located within 60 m horizontally and 15 m vertically of the exposed rupture. The three vertical boreholes (holes 10, 13 and 9 in Fig. 3.9) are up to 11.5 m deep with a diameter of 75 mm and vertical deviations up to 1.5°. They were logged with the Digital Optical TeleViewer camera. Clear stress indicators are observed within hole 10 and 13, whereas hole 9 did not reveal borehole failure.

Hole 10 images reveal several breakout zones with cumulative length of 2.6 m (out of 10.02 m total log). Most of the breakouts are in the incipient stage: minor amount of spalling, partly discontinuous, and with widths that range from a few degrees to ~ 20°. While these breakouts are poorly developed, they are distinct: 180° between the two sides, consistent trends, and restricted to limited blocks bounded by faults (BO in Fig. 4.3a). Two types of drilling-induced tensile fracture appear in hole 10. One is about 1 m tall and centered at a depth of about 9.1 m below the tunnel floor (DITF in Fig. 4.3a). It is a narrow, dark vertical (axial) feature, bisecting the interval between the breakouts and limited to one block with the two segments are at 184° to each other. The second is poorly developed below the fault-zone at the termination of the axial DITF, forming en-échelon pattern of DITF (Fig. 4.3a).

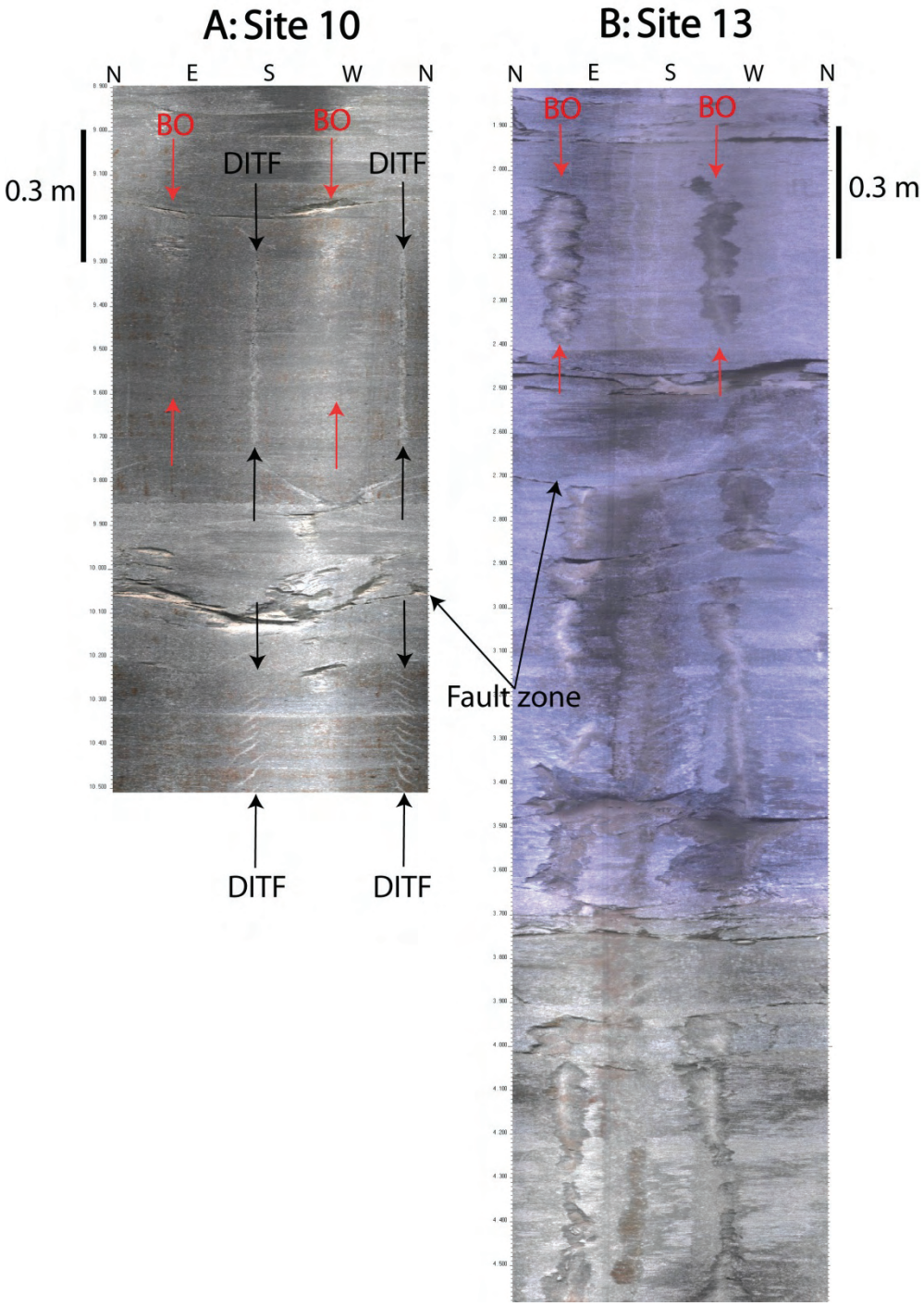

Figure 4.3: Borehole failure in image logs of short boreholes within the NELSAM site. (A) Borehole image log of hole 10 displays poorly developed borehole breakouts (BO) and well developed vertical axial planar drilling induced tensile fractures (DITF) as well as inclined, en échelon DITF at the bottom of the image. BO and DITF are bounded by fault-zones. (B)Borehole image log of hole 13 displays well developed borehole breakouts (BO). Some breakouts terminate abruptly against fault-zones and bedding surfaces.

Hole 13 images reveal several zones of well developed breakouts with cumulative length of 2.87 m (Fig. 4.3b) The breakouts are continuous within a given layer or block and range in width from 32° to 40°, accompanied with significant spalling. Some of the breakouts terminate abruptly against fault-zones and bedding surfaces.

The observed gaps in occurrence of breakouts and/or slight rotations of the orientations of the breakouts are bounded by faults or bedding surfaces observed in the boreholes. Previous work has shown that localized rotations and interruptions of breakouts are associated with local stress perturbations from recent slip on nearby faults (Barton and Zoback, 1994; Lucier et al., 2009). This suggests that some fractures and bedding planes within the NELSAM area were recently active, perturbing the local stress field. The poorly developed en-échelon DITF in Fig. 4.3 is separated from the axial DITF by a fault-zone. Occurrence of axial DITF is evidence that one of the principal stresses is parallel to the axis of the borehole (Peska and Zoback, 1995). The en-échelon DITF suggests a local change in the orientation of one of the principal stresses, most likely S_v, of a few degrees, suggesting recent slip along the faults that separate the two different DITF.

A total of 11 breakout zones in both boreholes and a DITF in hole 10 were observed. The average trend of the breakouts is 243.5°±7.7°. This indicated that S_{Hmax} trends 333.5°, which is in good agreement with the measured trend of the DITF that trends at 336°.

The magnitudes of the in-situ stresses are determined from the observed borehole failures following the method of Zoback et al. (2003). The method is based on effective hoop stress ($\sigma_{\theta\theta}$) and the radial stress (σ_{rr}) at the wellbore wall, and the effective stress

parallel to the axis of a vertical borehole (σ_{zz}) and the modified Kirsch equations (Kirsch, 1898):

$$\sigma_{\theta\theta} = S_{hmin} + S_{Hmax} - 2(S_{Hmax} - S_{hmin}) \cos 2\theta - 2P_p - \Delta P - \sigma^{\Delta T}$$

$$\sigma_{rr} = \Delta P$$

$$\sigma_{zz} = S_v - 2\nu(S_{Hmax} - S_{hmin}) \cos 2\theta - P_p - \sigma^{\Delta T}$$

where S_{hmin} and S_{Hmax} are the minimum and maximum horizontal stress components respectively, θ is the angle measured from the azimuth of S_{Hmax}, P_p is the pore pressure, ΔP is the difference between the pressure within the borehole and the pore pressure, ν is Poisson's ratio and $\sigma^{\Delta T}$ represents the thermal stress due to the difference between the temperature inside the borehole and the formation. The thermal stress can be described by:

$$\sigma^{\Delta T} = (\alpha_t E \Delta T)/(1 - \nu)$$

where α_t is the thermal expansion coefficient of the formation and E is the Young's modulus (Zoback et al., 2003).

Fig. 4.4a illustrates the circumferential effective stresses at the borehole walls for the following conditions: borehole internal pressure = 3.8 MPa (water pressure directly measured at the drill); pore pressure = 0 (for the very tight quartzite); ΔT = 25°C (estimated temperature difference between the water and the rock); Young's modulus = 77 GPa (rock mechanics experiments, Ch. 3); Poisson's ratio = 0.21; $\alpha_t = 7.1*10^{-6}$ (crystalline quartz); S_V = 97 MPa (3.6 km of overburden with a density of 2700 kg/m^3). The magnitudes of the in-situ stresses is estimated for the section of hole 10 that includes both the DITF and the poorly developed breakouts. The calculations were done in a

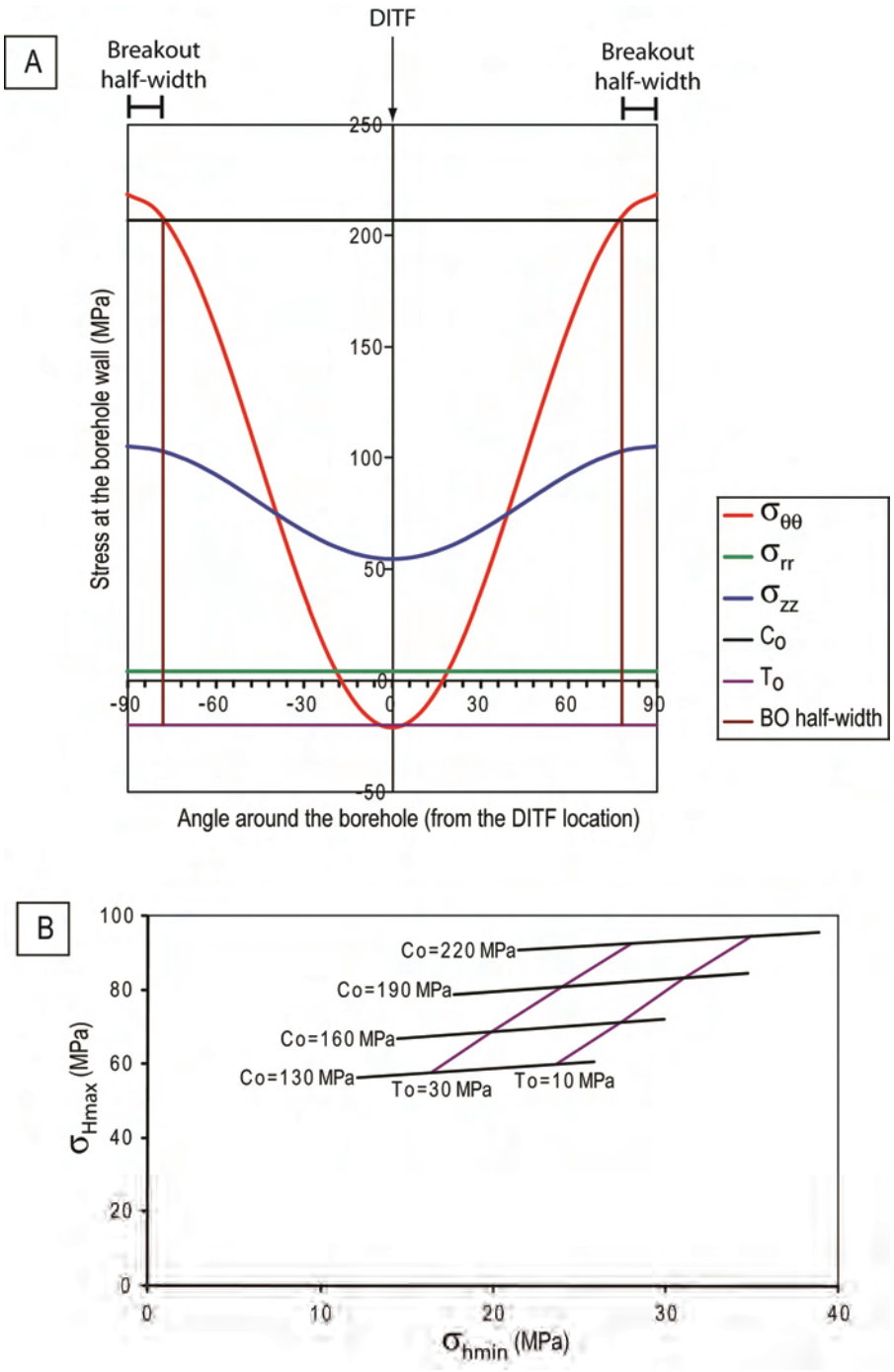

Figure 4.4: Stress calculations from boreholes close to the rupture zone. (A) Circumferential effective stress around the wall (after Zoback at al., 2003) of the vertical hole 10 for conditions: borehole internal pressure = 3.8 MPa; pore pressure = 0; ΔT = 25°C; Young's modulus = 77 GPa; Poisson's ratio = 0.21; $\alpha_t = 7.1*10^{-6}$; S_V = 97 MPa. The stresses displayed satisfy the observed breakouts with half-width 10° and the occurrence of drilling induced tensile fractures (DITF) for uniaxial compressive strength (C_o) of 207 MPa and tensile strength (T_o) of 26 MPa. (B) Range of magnitudes of in-situ stresses for hole 10 for a range of uniaxial compressive and tensile strength. The calculations are based on the method described in (A).

forward manner by “trial and error” of stress magnitudes that best fit, simultaneously, the breakout width of 20° and the presence of the DITF observations for a range of uniaxial compressive and tensile strengths (see Fig. 4.4b). Our experiments on quartzite samples of the Pretorius fault indicate uniaxial strength of 207 MPa (Fig. 3.10a, Ch. 3). Following Jaeger and Cook (1976) it is assumed that the uniaxial compressive strength (C_o) relates to the tensile strength (T_o) as:

$$C_o = 8T_o$$

Using C_o= 207 MPa and T_o= 26 MPa results in maximum and minimum horizontal stress with magnitude of ~90 MPa and ~30 MPa respectively (Fig. 4.4b). One should note however that the solution depend on the rock strength.

The observations of well developed breakouts in hole 13 with a width up to 40° and the lack of borehole failure within hole 9 were used to further constrain the magnitude of the stress field within the area of the M2.2 event, following the same technique. The results indicate constrains of the horizontal stresses such that S_{hmin} = 30-36 MPa and S_{Hmax} = 70-94 MPa, for reasonable range of uniaxial compressive strength and tensile strength of the Witwatersrand Basin quartzites (Table 4.1). The fact that the in-situ stresses for all 3 boreholes have similar orientations and that the magnitudes are constrained to a small range, suggest that the in-situ stresses listed in Table 4.1 closely represent the local in-situ stress field within the vicinity of all three boreholes, including the M2.2 rupture.

	Magnitude (MPa)	Plunge (°)	Trend (°)
S_{Hmax}	70 - 94	0	335
S_{hmin}	30 – 36	0	245
S_v	94	90	0

Table 4.1: Local in-situ stress state determined from borehole failure observed in holes 9, 10 and 13.

Modeled mining-induced stress tensor

The mining induced stress tensor, $[\sigma_{ij}]_M$ was calculated at the locations of hole 13 and 10 with the boundary-element program MAP3D (Murphy, personal communication). This stress tensor lists the state of stress at the boreholes based on the stress perturbation due to mining activity on the overburden stresses. The calculations were done for the layout and mining progress of the mine at the time of December 12, 2004, using Poisson's ratio of 0.2, and without tectonic stress. The results are averaged over a borehole depth of 3-10 meters, similar to the depth of the observed breakouts. The results for $[\sigma_{ij}]_M$, listed in Table 4.2, suggest a relatively small S_V with respect to S_{Hmax}. The reduction of S_V is related to the mining of the gold reef ~40 m above the tunnels from which the boreholes were drilled. In addition, the results of $[\sigma_{ij}]_M$ suggest that S_{Hmax} is similar in orientation to the S_{Hmax} orientation determined from the breakout analysis.

	Magnitude (MPa)	Plunge (°)	Trend (°)
σ_1	59	32	350
σ_2	45	42	117
σ_3	32	29	239
S_{Hmax}	54	0	160
S_{hmin}	36	0	250
S_v	46	90	0

Table 4.2: Mining induced stress tensor, calculated at the locations of hole 13 and 10 with the boundary-element program MAP3D. Calculations are averaged over a borehole depth of 3 -10 m.

Best fit stress tensor

Three independent observations are described that are related to the stress state within the area of the M2.2 rupture; the geometry of the rupture with slip direction, in-situ stresses from borehole images, and the mining induced stress tensor. Our objective below is to determine the in-situ stress tensor $[\sigma_{ij}]_R$ that best fits all three observations. The following is assumed:

1. The state of stress at the proximity of the rupture zone can be represented by one stress tensor.
2. The S_{hmin} is approximately equal to σ_3, and thus σ_3 is oriented 245° and its magnitude ranges 30 – 36 MPa (above discussion).

3. The S_{Hmax} is oriented 335° and its magnitude ranges 70 – 94 MPa (above discussion).
4. The calculated mining induced stresses $[\sigma_{ij}]_M$, indicate that S_V is relatively small with respect to S_{Hmax}. For this reason, I search for a $[\sigma_{ij}]_R$ for which the ratio of S_{Hmax} / S_V is largest.
5. The direction of maximum shear stress on the rupture, under $[\sigma_{ij}]_R$, is close to 15°/240°, which is the measured slip direction of this event.
6. The resulting shear stress (τ) and normal stress (σ_n) on the rupture surface, calculated from $[\sigma_{ij}]_R$, has the highest ratio of τ/σ_n.

The search is limited for horizontal σ_3 in a 245° trend (condition 2 above). As the principal stresses σ_1 and σ_2 are located within a plane which is perpendicular to σ_3, they are restricted to a vertical plane striking 335°. All possible permutations of magnitude and orientation of σ_1 and σ_2 with constant σ_3 = 30 MPa, are substituted into $[\sigma_{ij}]_R$. For each of the permutations, the predicted slip along the fault surface 43°/167° is calculated. The angle between this predicted slip direction and the observed slip from field observations is the misfit angle, α, from condition 5 above.

First, the numerical values for the ratio of S_{Hmax} / S_V are calculated for the condition 4, the ratio $1/\alpha$ of condition 5 and the ratio τ/σ_n of condition 6, for a range of possible orientations and magnitudes of principal stresses in $[\sigma_{ij}]_R$. Next, each ratio is normalized by its maximum value, providing equal weight of the three conditions 4, 5 and 6. To simultaneously optimize the three conditions, the factor K is defined as:

$$K = \frac{1}{\alpha} + \frac{\tau}{\sigma_n} + \frac{\sigma_{Hmax}}{\sigma_V}$$

The solutions with the highest optimizing factor K represents the best fit for the conditions 4 – 6 simultaneously. Fig. 4.5 displays the optimizing K factor as a function of the plunge of maximum compression (σ_1) and the stress ratio φ, where $\varphi = (\sigma_2-\sigma_3) / (\sigma_1-\sigma_3)$. A wide range of solutions are found with high K values (K > 2). The best-fit solution was selected by taking 24 tensors with the largest K values (2.100 < K < 2.138). From this group 12 tensors with the largest ratio S_{Hmax} / S_V were separated in order to be most conform with the MAP3D solution, suggesting a relatively low vertical stress. The solutions enclosed in the red contour (Fig. 4.5) have K > 2.10 and the lower S_{Hmax} / S_V ratio. The average solution within the red contour is the best fit tensor $[\sigma_{ij}]_R$ (black circle with error bars in Fig. 4.5) and is listed in Table 4.3. Fig. 4.6 displays the mining induced stress $[\sigma_{ij}]_M$ and the best fit tensor$[\sigma_{ij}]_R$ in a stereographic projection.

	Magnitude	Plunge (°)	Trend (°)
σ_1	86 ± 8 MPa	60 – 110	155 and 335
σ_2	69 ± 8 MPa	0 – 30 and 150 – 180	155 and 335
σ_3	30 MPa	0	245
S_{Hmax}	74 ± 6 MPa	0	335
S_{hmin}	30 MPa	0	245
S_v	80 ± 7 MPa	90	0
α	< 14°		
τ/σ_n	0.11 – 0.13		

Table 4.3: Best fit tensor displays the average of the solutions, with values for the optimization factor K > 2.10, that satisfy the conditions described in the text.

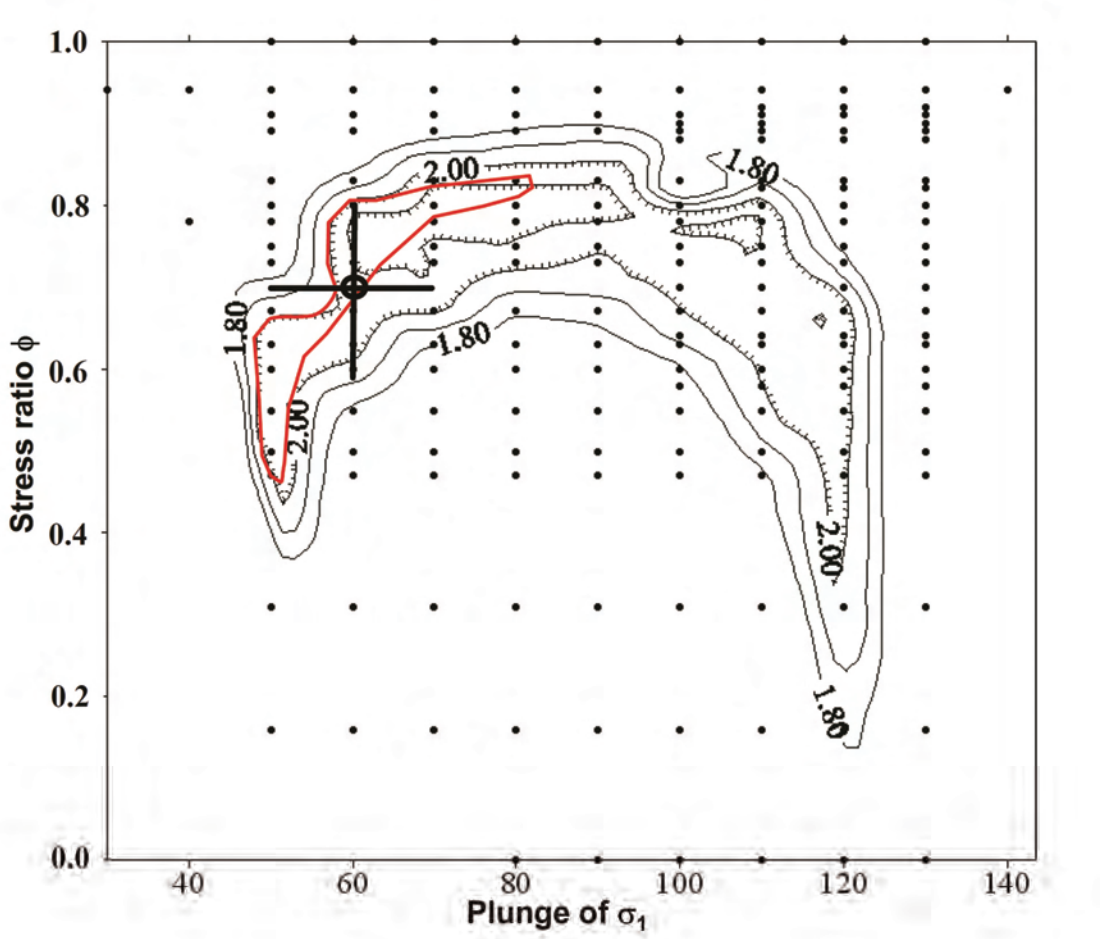

Figure 4.5: Optimization factor K to find the best fit stress tensor. The K factor optimized the conditions discussed in the text. Contours display 24 tensors with highest K values ($2.100 < K < 2.138$) for given stress ratio vs. plunge of σ_1. The solution enclosed in the red contour have $K > 2.10$ and the lower S_{Hmax} / S_V ratio. The black circle represents the average solution within the red contour, with error bars, and is the best fit tensor..

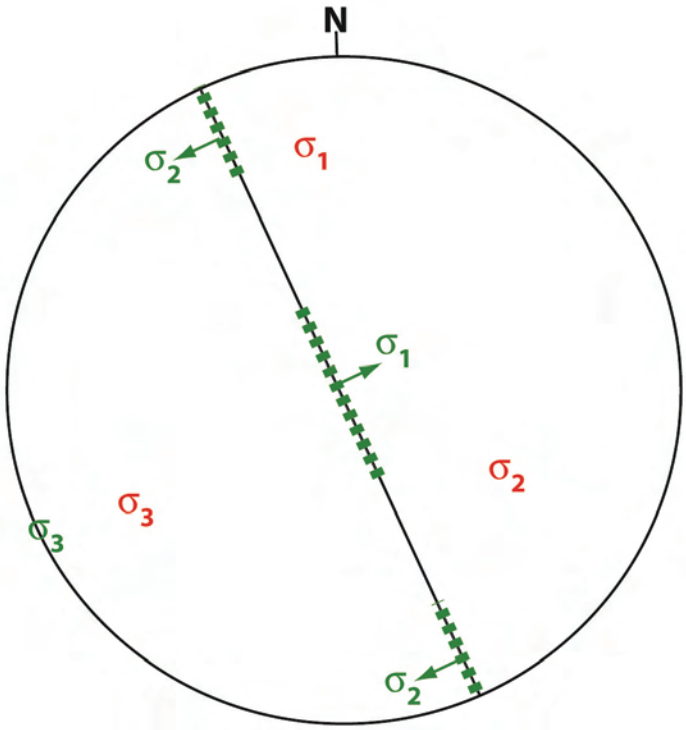

Figure 4.6: The mining induced stress $[\sigma_{ij}]_{M,}$ in red, and the best fit tensor$[\sigma_{ij}]_{R,}$ in green, in stereographic projection. The dashed green line displays the range of orientations for the best fit tensor that satisfy the conditions discussed in the text.

Stress on rupture segments

The observations from the borehole failures imply that S_{Hmax} is oriented semi-perpendicular to the Pretorius fault, and to the trend of the surfaces that slipped during the M2.2 event. This suggests that they are to be locked instead of critically stressed, due to the high magnitude and perpendicular orientation of S_{Hmax}. This hypothesis was investigated by calculating the normal and shear stresses on the slipped surfaces by combining the best fit stress tensor $[\sigma_{ij}]_R$ with the rupture geometry.

All accepted solution for the best fit tensor, $[\sigma_{ij}]_R$, indicate low shear stresses in the observed direction of slip along the reactivated surface A (43°/167°), with τ/σ_n = 0.11 - 0.13. The optimized slip direction along surface A for $[\sigma_{ij}]_R$ results in a ratio τ/σ_n = 0.14, with τ = 10.7 MPa and σ_n = 77.3 MPa. The calculated misfit angle between the predicted optimized slip direction and the observed slip direction, for the highest shear stress solution, is 11°. This suggests that the observed slip direction confirms with the estimated in-situ stress field for surface A, but that slip occurred under significantly low shear stress.

No evidence for a slip direction of the M2.2 rupture along surface B and C was observed during the underground mapping. However, secondary structures suggest a normal slip component along both segments. The calculated slip direction for $[\sigma_{ij}]_R$ indicates normal-dextral slip along surface B and normal-sinistral slip along surface C. The highest ratio of τ/σ_n along surface B and C, consistent with a normal slip component under the state of stress of $[\sigma_{ij}]_R$, results in ratios for τ/σ_n of 0.11 and 0.13 respectively. The range of values for the shear stress (τ) and the normal stress (σ_n) over all three

slipped surfaces under the state of stress of $[\sigma_{ij}]_R$, conform with the observed slip directions, are τ = 3.7-10.7 MPa and σ_n = 66.9-83.9 MPa.

Our findings for the best fit tensor in the area of the exposed rupture and hole 9, 10 and 13 indicate that slip occurred under low ratio of shear stress to normal stress. This suggests that either significant weakening occurred during the M2.2 rupture, or that the failure was controlled by the geometry of the mine opening rather then by the in-situ stress.

MAIN FINDINGS OF THE IN-SITU STATE OF STRESS

The in-situ stresses, calculated in 3 boreholes in the vicinity of the M2.2 rupture, have similar orientations and magnitudes, suggesting that this closely represents the local in-situ stress field (Table 4.1) within the vicinity of all three boreholes, including the M2.2 rupture. The orientations of the local in-situ stress field are similar to the orientations of the far field in-situ stress (Fig. 4.2). The best fit stress tensor in the area of the exposed rupture (Table 4.3), conform with borehole failure observations, boundary element model calculations and observed rake of slip along the M2.2 rupture, suggests that slip occurred under significantly low shear stress, with maximum τ/σ_n = 0.14.

ENERGY BALANCE OF THE M2.2 EARTHQUAKE

During an earthquake, the potential energy (ΔW), a combination of the elastic strain energy and gravitational energy, is released through radiation energy (E_R), frictional heat energy (E_H) and fracture energy (E_G) following (Kanamori, 2004; Scholz, 2002):

$$\Delta W = E_R + E_H + E_G$$

The details of the magnitude of each energy term, the energy partitioning, and its variation with earthquake magnitude and tectonic setting, are not well constrained (Beeler et al., 2003; Chester et al., 2005; Kanamori, 2004). The unique situation of the exposed rupture surface of a single earthquake, in combination with its seismic signal and nearby stress measurements, allows estimation of the energy partitioning during the M2.2 event.

The total potential energy can be estimated from a combination of field observations with the seismic moment, M_o, following (Beeler et al., 2003):

$$W = \frac{\tau_a M_o}{G}$$

where τ_a represents the average shear stress along the fault and G the shear modulus. The shear modulus for the quartzites is derived from our rock mechanics experiments (Ch. 3), as 32 GPa. The seismic moment M_o of the rupture is calculated to be 2.6 x 10^{12} Nm based on the ISSI seismic network, with an estimated rupture area of 2900 m^2 (Boettcher et al., 2006). Assuming a shear stress along the fault of τ = 3.7 - 10.7 MPa (range of resulting shear stress based on the local in-situ best fit stress tensor $[\sigma_{ij}]_R$), the calculated potential energy (W) for the M2.2 rupture is 300 to 870 MJ.

The radiation energy (E_R) of the event was calculated from the seismic data (Boettcher et al., 2006) following the method of Haskell (1964). The results suggest that E_R significantly decreases with the distance from the source, due to inelastic attenuation and scattering. It is generally accepted that the radiation energy of an earthquake only contributes about 6% of the total potential energy (McGarr, 1999). Our estimated radiation energy E_R = 20-40 MJ (Boettcher et al., 2006) for the M2.2 event, suggests 2 - 13% of the total potential energy is lost by radiation.

The frictional heat energy is equal to the work done to overcome the fault frictional resistance (Scholz, 2002). The frictional work associated with the M2.2 rupture is estimated following:

$$E_{\mathrm{H}} = \tau \mathrm{d}A$$

where τ is the shear stress, d the average displacement along the fault and A the area of the rupture (Reches and Dewers, 2005). The shear stress, determined above, is 3.7 – 10.7 MPa. The average displacement is assumed to equal the measured displacement of 25 mm (Ch. 3). Using the rupture area calculated from the seismic data of 2900 m^2 (Boettcher et al., 2006), which fits within the range of rupture area derived from field observations of 280 – 3375 m^2 (Ch. 3), a heat energy of E_H = 260 – 780 MJ is estimated for the 25 mm of observed slip. This estimation is based on the assumption of constant shear stress along all three reactivated segments, even though evidence for displacement was found only along segment A. By this calculation, the estimated heat energy accounts for at least 30% to the total potential energy of the earthquake.

The fracture energy represents the generation of new surface area in the gouge powder and fractures (Wilson, 2005). For a tensile fracture in a brittle material, the specific fracture energy is nearly equivalent to the surface energy of the fracture (Brace and Walsh, 1962; Friedman et al., 1972). The cumulative surface energy of a fault gouge can be used as an estimate for the fracture energy of the earthquake (Chester et al., 2005; Wilson et al., 2005). Previously the assumption was made that the gouge surface energy has a negligible contribution to the earthquake energy budget (Andrews, 2005; Heaton, 1990; Chester et al., 2004). Wilson et al. (2005) showed that gouge formation of earthquakes can encounter for 50% or more of the total earthquake energy. They

analyzed the particle size distribution of fault gouge from another rupture zone, the Bosman fault, in the Hartebeestfontein mine in South Africa, and pulverized rocks from the San Andreas Fault at Tejon Pass, California. They found that grains are in nano-sized primary scale with surface area up to 100 m^2/g.

The gouge that formed during the M2.2 event is identical in appearance to the fresh ultra-fine gouge observed along the Bosman fault and elsewhere in ruptures within the mine (Wilson et al., 2005). Both earthquakes generated ultra-fine white fresh rock flour from similar host rocks (Witwatersrand quartzite). A similar grain size distribution is assumed with a surface area of 80 m^2g^{-1} that corresponds to a surface energy of 0.2 – 0.36 MJ per m^2 for a 1 mm thick gouge zone. Underground mapping of the M2.2 event revealed fresh gouge formation along 1-5 zones each of 0.5-1 mm thick. To estimate the minimum E_G, a minimum of 1 zone of gouge along the entire rupture is assumed, with a minimum thickness of 0.5 mm. Using a rupture area 2900 m^2, the estimated fracture energy for the M2.2 rupture is between 290 – 522 MJ. This estimate does not include energy consumed by the secondary fractures (e.g. Fig. 3.7, Ch. 3) and off-fault damage (Ch 3). The estimated fracture energy is approximately equal to frictional heat energy.

MAIN FINDINGS

The earthquake energy partitioning of a single earthquake, the M2.2 rupture, is estimated by combining filed observations with nearby stress measurements and the seismic signal. It was found that the fracture energy is at least equal, if not larger, than the heat energy, contributing for at least a third to the total energy budged of the event. The contribution of the radiation energy is not more than 13% of the total energy budget.

DISCUSSION: RUPTURING AND IN-SITU STRESS FIELD

The local in-situ stress field in the vicinity of the exposed rupture was estimated based on borehole failures of three nearby boreholes, drilled 4-5 months after the M2.2 event of December 12, 2004. The analysis of the data suggests a homogeneous stress field (Table 4.1) with orientations consistent with the mining induced stress tensor, calculated for the borehole locations at the time of the rupture. In addition, the orientations are consistent with the orientations of the far field in-situ stress, estimated from borehole failures in a borehole that extends several hundreds of meters outside the mining area. This suggests that the mining operations in the area of the exposed rupture zone do not significantly affect the orientations of the stresses. Hence, it is assumed that the best fit tensor (Table 4.3) represents the state of stress in the vicinity of the M2.2 event.

The above conclusion leads to an apparent paradox. The underground observations of the direction of slip along the reactivated surfaces are consistent with the suggested slip based of the best fit stress tensor $[\sigma_{ij}]_R$ (Table 4.3). However, the orientation of S_{Hmax} is oriented roughly perpendicular to the segments, resulting in very low ratio of shear/normal stress on the slipping surfaces, with maximum $\tau/\sigma_n = 0.14$. Further, the slip was localized almost exclusively along ancient segments of the Pretorius fault (Ch.3) that were healed during a 2 Ba period. It is puzzling how slip occurred along these three segments simultaneously and why failure did not occur by forming more favorably oriented, new faults, as occurred in previous cases (Dor et al., 2001; McGarr et al., 1979).

Below five explanations are discussed that could lead to the observed slip during the M2.2 event, under low shear/normal stress ratio; (1) Quasi-static weakening, (2) Dynamic

weakening, (3) Stress rotation within the damage zones, (4) Stress perturbation by active mining, and (5) Earthquake dynamic effects.

1) **Quasi-static weakening**. Similar configurations to our observations have been determined close to the San Andreas Fault, California, where S_{Hmax} is at high angle (60-80°) with respect to active sub-vertical strike slip faults (Rice, 1992; Zoback et al., 1987), and the active Nojima Fault, Japan, where stress measurements suggests that S_{Hmax} is oriented almost perpendicular to the active fault trend (Yamamoto et al., 2000). These observations were explained by inherently weak fault-zone material (Moore and Rymer, 2007), or high pore fluid pressures (Chester et al., 1993; Tembe et al., 2009). However, such mechanisms are not applicable to the Pretorius fault as the fault rock is strong as suggested by the rock mechanics experiment (Ch. 2), and no evidence found for elevated pore pressure in the dewatered mining area.

2) **Dynamic weakening.** The shear resistance of a fault can be lowered during high velocity, co-seismic slip rates (Dieterich, 1978), by a thin layer of silica-gel on the slip surface (Di Toro et al., 2004), shear melting (Mair and Marone, 2000; Tsutsumi and Shimamoto), pore fluid pressurization (Lachenbruch, 1980), acoustic fluidization (Melosh, 1996), elastohydrodynamic lubrication (Brodsky and Kanamori, 2001), and lubrication by a gouge layer (Reches et al., 2009). While dynamic weakening has been used to explain earthquake instability, it is generally accepted that slip initiates when the quasi-static friction is exceeded.

3) **Stress rotation within a damage zone**. Faulkner et al. (2006) and Healy (2008) discussed the possibility of local stress rotations near active faults due to the

presence of a damage zone. They showed that the reduction of the elastic properties and preferred crack orientations could rotate σ_1 as much as 45°. Our stress measurements are conducted within 3 boreholes that surround the rupture zone, all within a distance of 60 m from the rupture. This would suggests that if local stress rotations towards the reactivated surfaces occurred due to the significant damaged quartzites within the fault-zone, these rotations would have to concentrate within tens of meter of the rupture.

4) **Stress perturbation by active mining**. The complex mining activity in the vicinity of the M2.2, with two overlapping reef zones (Fig. 2.2) and complex tunnel geometry, disturb the stress field that could locally change stresses at the rupture segments. This hypothesis was tested by Lucier (2009), using the boundary-element program MAP3D. She examined how the stress perturbations from the mining excavation affect the likelihood of slip on the three reactivated segments of the M2.2 event (Figs. 4.7 and 4.8). The likelihood of slip was defined in terms of the Coulomb Failure Function, $CFF = \tau - \mu\sigma_n$, where τ and σ_n are the shear and normal stress on a fault plane and μ is the sliding friction. If CFF is positive, the fault is moved towards being critically stressed. The calculations were done for $\mu = 0.6$, at mining configuration before the M2.2 event, mining step 1 (green in Fig. 4.7), which does not include any excavation on the upper reef (Fig. 2.2), and mining step 2 (purple in Fig. 4.7) that represents the beginning of the mining of the upper reef at the time of the rupture. The results indicate that CFF resolved for segment C (F1 in Fig. 4.7a), displays area of positive CFF (red colors) after mining step 1. The area of positive CFF along the segment increases

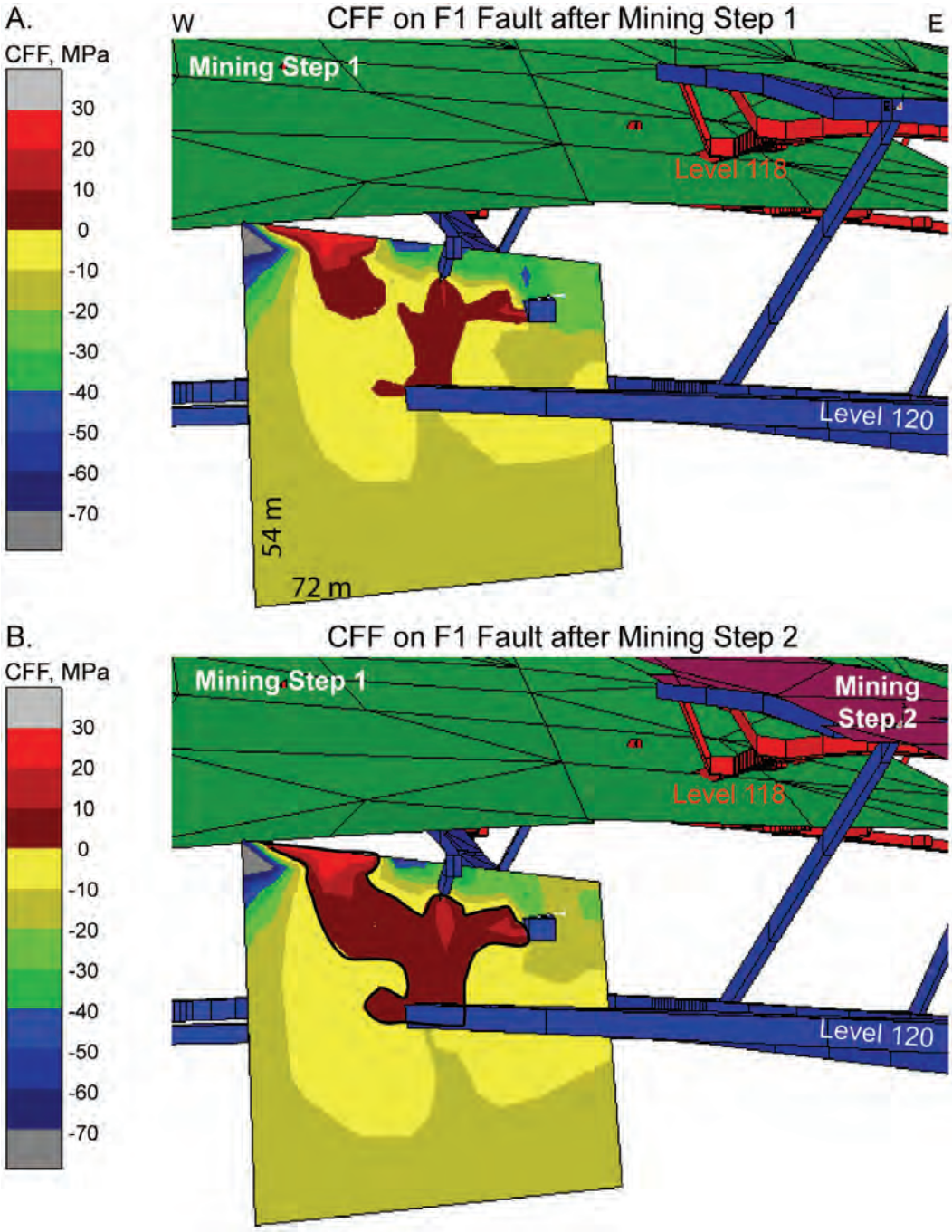

Figure 4.7: Modeling the potential for mining-induced seismicity on the F1 fault (segment C). A.) CFF resolved on F1 after mining step one (green), red colors indicates positive CFF. B.) CFF resolved on F1 after mining step two (purple). The area of positive CFF (red colors) is increased relative to that in mining step one (Lucier et al., 2009).

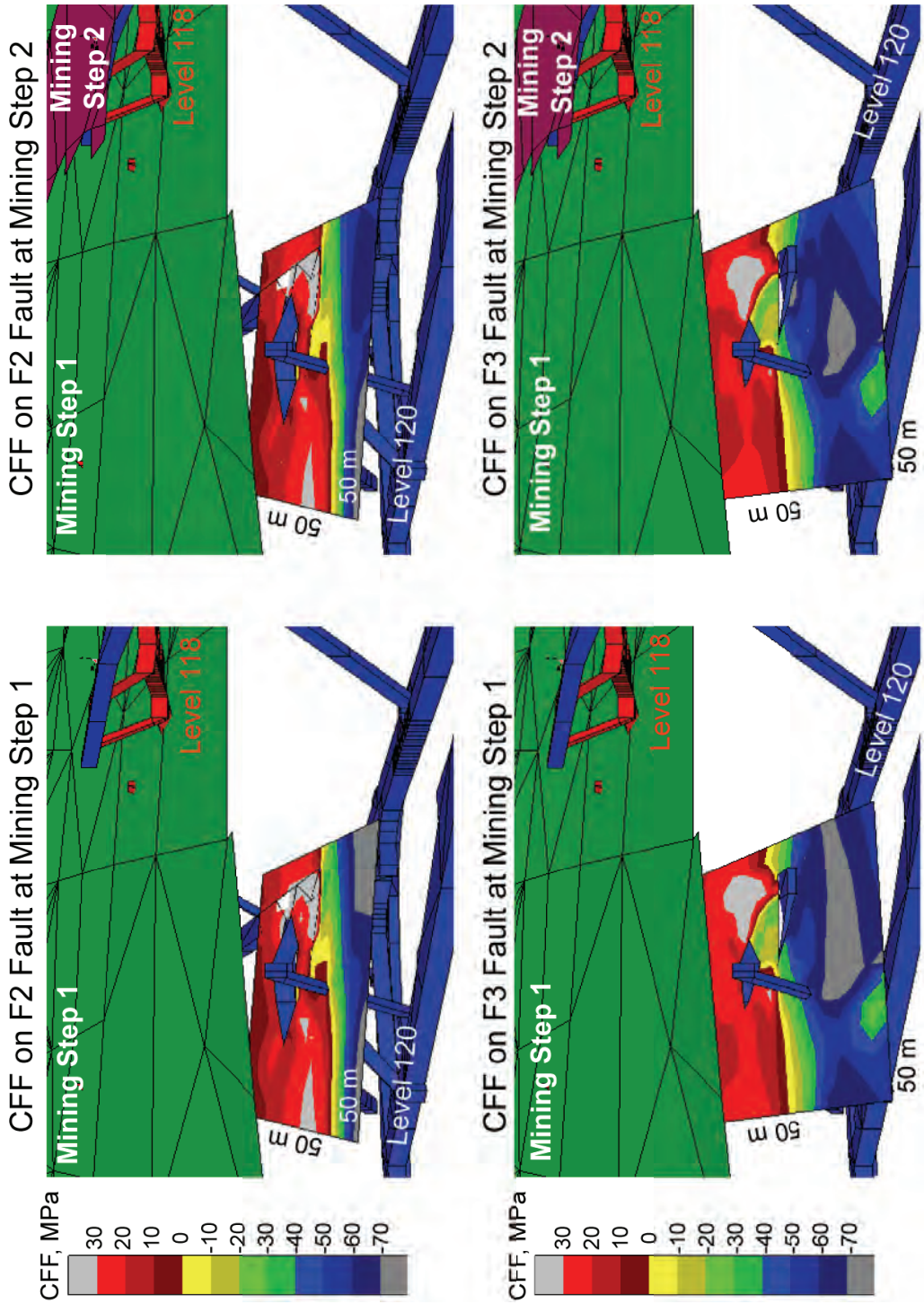

Figure 4.8: CFF resolved on F2 (segment B) and F3 (segment A) at mining steps one (left) and two (right). The red colors and light gray indicate the critically stressed areas of the faults (Lucier et al., 2009).

5) for mining step 2. The change in CFF between the mining steps suggests that segment C is more likely to slip, as a result of this change in mining conditions in the overlaying reef. Fig. 4.8 display the CFF resolved on segment A (F3 in Fig. 4.8) and segment B (F2 in Fig. 4.8) for both mining steps. Although critically stresses, the areas of positive CFF between the two mining steps does not change for both segments, suggesting that these segments would not slip as a result of the change in mining conditions. Therefore, the slip of the M2.2 event could have nucleated at segment C. A suggested slip direction for the change in CFF was not calculated.

6) **Earthquake dynamic stress field.** If a local, small slip occurred within a weak area in the Pretorius fault, it could dynamically alter the stress field and allow the M2.2 to slip in unfavorable static stress state. This initial small event could serve as a trigger to the much larger event. A possible analogue to this scenario was presented recently by Boettcher et al. (2009) in their analysis of small earthquake in the Pretorius fault. They show that two “pre-shocks” of M- 3.9 and M- 3.4 preceded an M- 2.7 ‘‘main-shock’’ by a few tens of milliseconds. Analyzing the dynamic stress field associated with the M2.2 earthquake is beyond the scope of the present study, but one can speculate that similar “pre-shocks” could activate the M2.2 earthquake.

The mechanisms proposed above could explain the observed slip along the three unfavorably oriented segments during the M2.2 event. The most likely scenario for the M2.2 rupture is nucleation along segment C, which is the main slip zone (MSZ) of the Pretorius fault (Ch. 2), leading to dynamic stress interaction on the other segments of the

rupture zone. All three segments underwent dynamic weakening due to gouge formation and lubrication.

CONCLUSIONS

The stress and energetics associated with the M2.2 event that reactivated several segments of the Pretorius fault, TauTona mine, South Africa, are analyzed in this chapter. Borehole failures combined with boundary element modeling, suggest a normal faulting regime in the vicinity of the TauTona mine (Lucier et al., 2009).

The stress associated with the M2.2 rupture is determined by observations of borehole failures within three vertical boreholes within 60 m of the rupture exposure. It was found that:

1) The local stress field in the vicinity of the exposed rupture is determined by the best fit stress tensor (Table 4.3) that satisfies the observations of drilling induced tensile fractures and borehole breakouts within 3 vertical boreholes, the geometry of the rupture surfaces of the M2.2 event, and the mining induced stress tensor, calculated with MAP3D.
2) The maximum horizontal compressive stress, S_{Hmax}, is oriented semi-perpendicular to the reactivated surfaces of the M2.2 event, indicating high fault-normal stresses and low shear stresses resolved along the rupture surfaces. Most likely the M2.2 rupture nucleated along segment C, which is the main slip zone (MSZ) of the Pretorius fault (Ch. 2), leading to dynamic stress interaction on the other segments of the rupture zone.

3) Our estimate of energy balance of the M2.2 earthquake suggests that seismic radiation consumed 2-13% of the total energy, and fracture energy (=gouge formation) is roughly equal to the frictional heat energy.

Chapter 5:

Numerical Simulations of Ramp-Thrust Systems:

Analysis of Rheology and Inter-layer Friction

INTRODUCTION

Ramp-related folds are common structures in fold-and-thrust belts (e.g., Douglas (1950); Dahlstrom, (1970); Boyer and Elliott, (1982). The ramp-folding model was first proposed by Rich (1934) to explain the structural features at the Cumberland overthrust block of the Appalachian orogeny. In his model, a sequence of sedimentary rock moves along a bedding-parallel horizontal thrust fault that jumps from one level to another through an inclined ramp (Fig. 5.1a). Rich proposed that this configuration leads to the development of an anticlinal structure with a flat crestal region (Fig. 5.1a). Rich's model has been adopted to describe structures in the Idaho-Wyoming thrust belt (Royse et al., 1975), the Canadian Rockies (Douglas, 1950), and many folds in the Appalachians (Harris and Milici, 1977; Mitra, 1988; Rodgers, 1963). In the recent three decades, several quantitative geometric-kinematic ramp models have provided insight in fault related fold geometries (Johnson and Berger, 1989; Mitra, 1990; Suppe, 1983). These models are based on the balanced cross-section concept and seismic interpretations that include assumptions of layer-parallel shear, kink-type folding and constant bed thickness. This chapter focuses on the geometry of a single ramp structure with emphasis on the effects of rock-layers rheology and friction between the layers. The finite element code of Abaqus was used to study these effects.

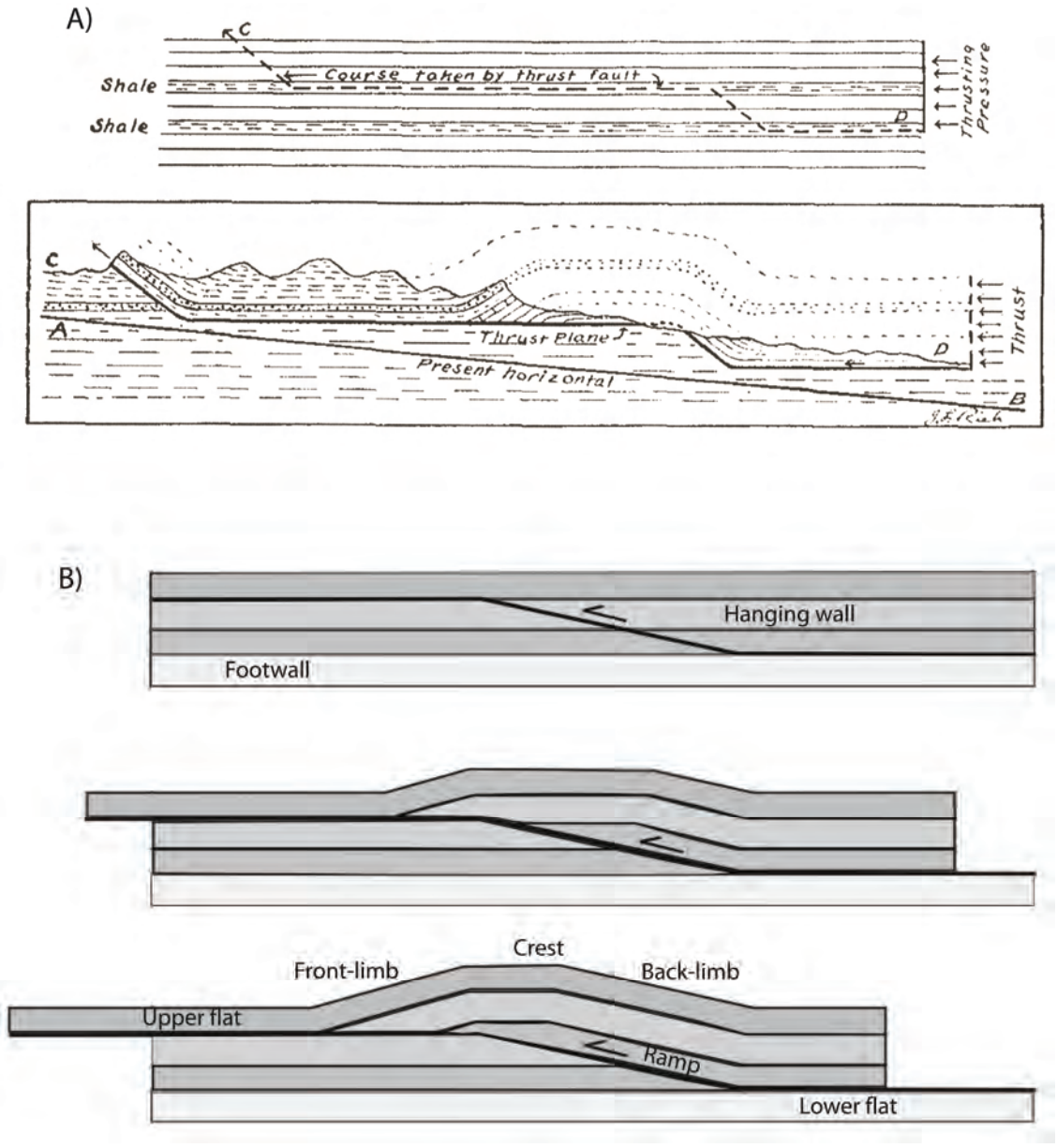

Figure 5.1: Ramp-folding model of a single ramp structure. A) Cross section of the Cumberland overthrust block of the Appalachians and the suggested model of ramp-folding of sedimentary rocks that move over a bedding-parallel horizontal thrust fault that jumps from one level to another through an inclined ramp, to form the Pine Mountain anticline with a flat crestal region (Rich, 1943). (B) Development of ramp-related folds conform to Rich's model, including proper terminology (Suppe, 1983). As the sedimentary units move over the ramp, a symmetric anticline forms with flat crestal region. The inclination of the front- and back-limb is equal, but opposite.

Rocks in the upper crust have complex non-linear rheology deforming in the brittle regime by fractures and faults, and in the ductile regime by shear zones, flow and folds. Deformation of material with complex rheology can be simplified by elastic (Stein and Ekstrom, 1992), plastic or viscous behavior (Erickson, 1996; Johnson and Fletcher, 1994), or a combination of these (Erickson and Jamison, 1995). The deformation history of some large scale geological structures, e.g. fold and thrust belts, is associated with large amounts of strain in excess of 100% locally, far beyond the infinitesimal strain as predicted in elastic theory. Hence, it is essential to incorporate finite strain and non-linear inelastic behavior into the analysis of large scale structures.

A finite element model is presented to investigate the effects of elastic, elastic-plastic and a non-linear elastic-plastic-damage rheology, on the geometry of folding above a ramp. In the model the inter-layer friction is controlled and different boundary conditions are investigated. The strain distribution through time of development is discussed and the final geometry of the fold is analyzed. It is demonstrated that a more realistic material definition has significant impact on the fold geometry. The non-linear and post-beak behavior of the rheology controls folding amplitude and asymmetry and generates localization of dilatational volumetric strain.

RAMP FOLDING MODELS

The classic analysis of ramp folding was developed by Suppe (1983) in which he presented a quantitative description of the geometry of ramp-related folding. These geometric relations has been applied to the interpretation of a number of map-scale folds (Mitra, 1990; Suppe, 1983). The model assumes uniform bed thickness and parallel fold

geometry with kink-folding and flexural-slip being the main mechanism of deformation. As the hanging wall moves over the ramp, a fold develops that progressively increases its structural relief, until the entire hanging wall segment is transferred over the ramp. At this stage the width of the crest of the fold is increased with increasing displacement and used as a measure for displacement along the fault. During the development of the fold, the dip on the back-limb of the fold above the ramp is assumed to be parallel to the dip of the ramp itself. Suppe (1983) derived equations for angular relations between the upper and lower ramp-flat transition angle, the fold inter-limb angle and the dip of the fault, providing a useful tool for interpretation of such structures and balancing of cross sections. Internal strain within layers during ramp folding was recognized by Mitra and Namson (1989), who pointed out the importance of knowing the original bed thickness during equal area balancing as strains as small as 10% can lead to major variations in the restoration.

A kinematic model is described by Johnson and Berger (1989) that reproduces the exact fold geometry described by Suppe (1983), while obeying the similar assumptions as for the geometrical model. The amplitude of the fold near the ramp is equal to the thickness of the duplicated section by faulting, and the crest is flat. The thickness of the beds in constant, except within the fold hinges, and the shape of the kink-like bands on both sides of the anticline is independent of displacement. The result is a complete kinematical analysis of Suppe's model that provides a link between the geometrical and mechanical models.

Mechanical analyses of ramp folding investigated the effect of pore pressure on the reduction of frictional sliding on the fault (Raleigh and Griggs, 1963; Rubey and

Hubbert, 1965), the effect of roughness of the fault surface (Elliott, 1976), and determination of stress and deformations of a viscous layer that moves up the ramp (Erickson and Jamison, 1995; Johnson and Fletcher, 1994; Wiltschko, 1979). Berger and Johnson (1980) preformed a mechanical analysis of ramp folding of homogeneous, viscous thrust sheets translated over and idealized ramp in a detachment surface. They found that the resulting folds have symmetric limbs and a flat crest, similar to Rich's model. They incorporated frictional drag on the ramp and investigated folding, stresses and strains within the thrust sheet, and expressed the shape of folding by a Fourier sinusoidal series (Berger and Johnson, 1980; Johnson and Fletcher, 1994).

The above mechanical models greatly contributed to the understanding of physical processes that control mechanisms of ramp folding. In this chapter, a mechanical analysis is presented to investigate the effect of inter-layer friction and rheology on the geometry of the fold above a friction-less ramp

MODEL DESIGN

MODEL GLOBAL GEOMETRY

A 2D finite element model is developed, based on a simplified model of a single ramp structure (Fig. 5.1b) conforming to Rich's model. The model displays the geometrical development of a ramp-related fold as predicted by the model of Suppe (1983), and presents terminology adopted in this chapter. The finite element model that is founded on this simplified ramp-model has generic dimensions that do not fit a specific structure. A sedimentary sequence of 7.5 km thickness overlies, with a fault contact, a rigid basement with a ramp (Fig. 5.2). The model is 50 km long with the ramp at its center, and the

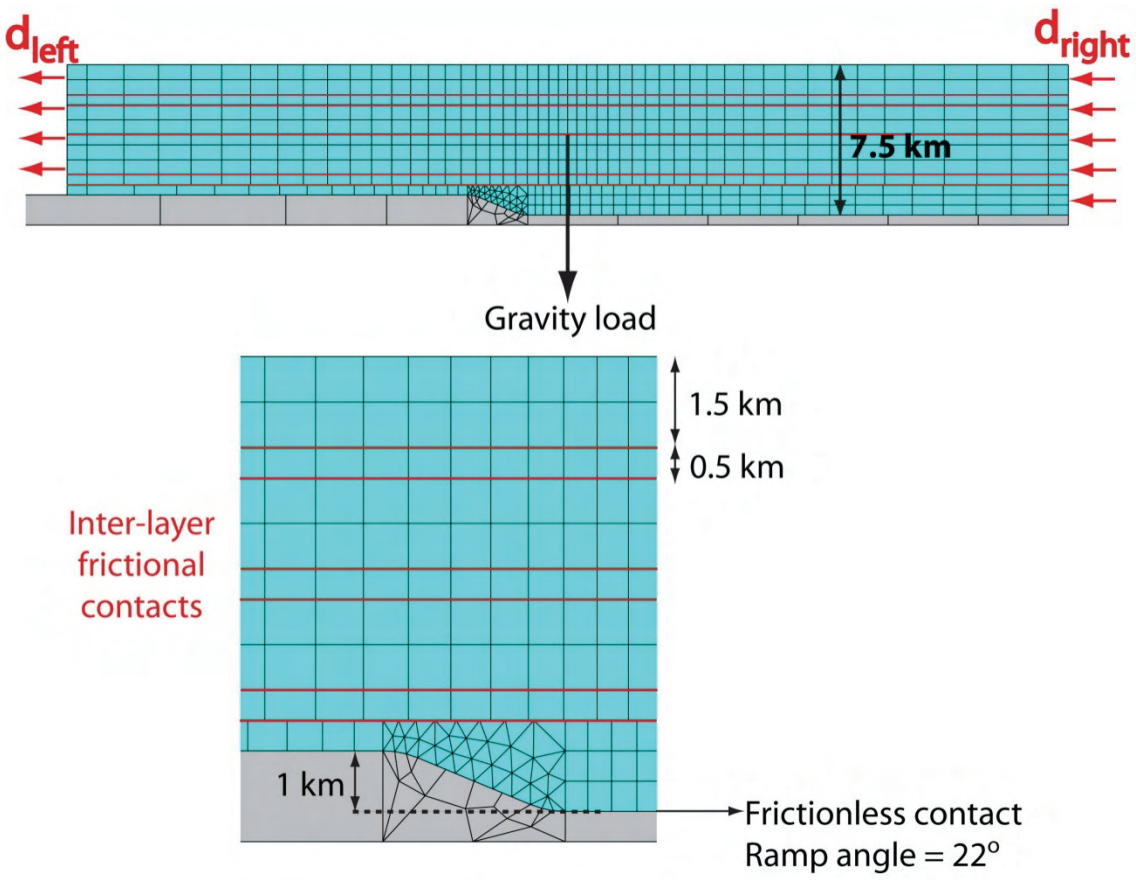

Figure 5.2: Finite element model geometry of a ramp structure. A 7.5 km thick, 50 km long sedimentary package, consisting of alternating 0.5 to 1.5km thick layers with frictional contacts, overlies a rigid basement with a fault contact that is frictionless. The ramp is inclines 22°, with a vertical structural step of 1 km. Displacement boundary conditions are applied on the margins of the sedimentary package (d_{left} and d_{right}). Gravitational load is applied to the entire model. The basement is considered to be rigid. The mesh consists of linear quadrilateral elements for the sedimentary layers, with triangular elements at the ramp.

sedimentary cover consists of alternating layers 1.5 km and 0.5 km thick with frictional contacts. The ramp is inclined at 22.5° forming a vertical structural step of 1 km (Fig. 5.2).

MESH

For the sedimentary cover, a structured mesh was used consisting of linear, plane strain, quadrilateral and triangular elements. The mesh density was increased towards the center of the sediment layers (Fig 5.2). The thin layers (0.5 km) are meshed with a single row of quadrilateral elements. The thick layers (1.5 km) are meshed with 2 rows of quadrilateral elements, each with a thickness of 0.75 km. The lowest layer, connecting to the footwall, is meshed with a single row of 0.75 km thick quadrilateral elements to the left of the ramp and three rows of quadrilateral elements to the right of the ramp, each 0.5 km thick. Above the ramp, the lowest layer was meshed with triangular elements in order to handle the ramp geometry. The quadrilateral elements have a maximum length of 1.83 km and a minimum length of 371 m. The edges of triangular elements range from 720 m to 195 m. The sharp edge transition between the ramp and horizontal nature of the footwall was smoothened out by curved (fillet) geometry. The footwall is meshed with a single row of up to 12 km long quadrilateral elements. At the ramp a free quad-dominated mesh was used (mixing quadrilateral elements with triangular elements). The footwall is assumed to be undeformable; therefore the single purpose for a mesh definition is to define contact properties along the top of the basement, justifying the coarse mesh. A total of 637 elements and 1000 nodes are used for the entire model.

BOUNDARY CONDITIONS

The external nodes of the basement are pinned. Displacement boundary conditions are applied on the left of the entire sedimentary cover, d_{left}, and on the right side, d_{right} (Fig. 5.2). Both d_{left} and d_{right} act towards the left (negative x-direction), and are varied to be 0, 10 or 20 km. The contacts between the layers and between the ramp and the sedimentary cover are defined as "hard" contact to avoid significant penetrations. No separation between the contacts is allowed. The tangential behavior for the contacts is a penalty formulation for given friction coefficients. The contact resistance between the basement and the sediments is set to be zero (frictionless). The coefficient of friction for the contacts between the individual sedimentary layers was varied to be 0.0, 0.4 and 0.8. The surface of the upper most sedimentary layer acts as a free surface. A gravitational acceleration of 9.81 m s^{-2} is applied to the entire model.

MATERIALS

The materials assigned to the sedimentary cover above the ramp include standard linear-elastic (Table 5.1), elastic-plastic (Table 5.2), and elastic-plastic-damage rheology (Table 5.3) that is discussed below. The basement is isotropic linear elastic, and ten times as stiff as the sedimentary cover.

ρ (gm^{-3})	2600
E (GPa)	200
ν	0.2

Table 5.1: Linear-elastic material properties

Elasticity			Plasticity	
			Compressive	
			Yield stress (MPa)	Plastic strain
ρ (gm^{-3})	2600		80	0
E (GPa)	50		110	0.05
ν	0.2		130	0.08
			150	0.1
			180	0.15
			200	0.2
			220	0.3
			250	0.4

Table 5.2: Elastic-Plastic material properties. Parameters of plasticity are directly entered into Abaqus.

Elasticity			Plasticity							
			Compressive			Tensile			Parameters	
			Yield stress (MPa)	Plastic strain		Yield stress (MPa)	Plastic strain			
ρ (gm^{-3})	2100		41	0		3.2	0		Density	2100
E (GPa)	20.2		58	0.0003		5.5	0.0001		E (GPa)	20.2
ν	0.27		69	0.0008		6.6	0.00045		υ	0.27
			74	0.0013		6.9	0.0008		Ψ	15
			70	0.0016		6	0.0009		ecc.	0.1
			56	0.0021		5	0.00098		fc0/fb0	1.16
			38	0.0027		3	0.00115		K_c	0.66
						1.9	0.00135		viscos.	0

Table 5.3: Elastic-Plastic-Damage material properties. Parameters of plasticity are directly entered into Abaqus and were calibrated against the mechanical behavior of Berea sandstone (Busetti, 2009, Ch. 2).

Elastic-plastic-damage

The elastic-plastic-damage (EPD) material, developed by Busetti (2009), can realistically simulate rock behavior in laboratory experiments (Busetti, 2009, Ch. 2). The

material was derived from rock mechanics experiments with Berea sandstone; these experiments include both compression and tension loading, and display pressure dependent yielding and stiffness degradation. Parameters of yield stress and associated inelastic strains are directly entered into the Concrete Damaged Plasticity material model of Abaqus (Table 5.3). The resulting stress-strain curves for both compression and tension were calibrated against the mechanical behavior of Berea sandstone (Busetti, 2009, Ch. 2) in four-point beam bending experiments (Weinberger et al., 1994) and tri-axial experiments of dog-bone shaped samples (Bobich, 2005; Ramsey and Chester, 2004). The post-yielding curves for plastic strain for the material are illustrated in Fig. 5.3. The material is about 10 times stronger in compression then in tension. The elastic parameters of the elastic-plastic-damage material are defined by E = 20.2 GPa and ν = 0.27 with a density of 2100 gm^{-3}. Other Abaqus material parameters are a dilation angle of 15°, a K_c value of 0.66, indicating minimal dependence on the intermediate principal stress, as well as the default value for the ratio of initial equi-biaxial to uniaxial compressive yield stress, fb0/fbc= 1.16, which contributes to the shape of the yield surface. These parameters were determined by calibration against laboratory experiments (Busetti, 2009, Ch. 2).

The stress-strain behavior of each rheology, for a single element, during the same model run is displayed in Fig. 5.4. The post-peak behavior of the elastic-plastic-damage material displays non-linear softening, highly dependent on the behavior of neighboring elements. For high amounts of strain, the elastic rheology is quasi-rigid, while the elastic-plastic-damage material is the softest (Fig. 5.4) due to post-failure strain softening.

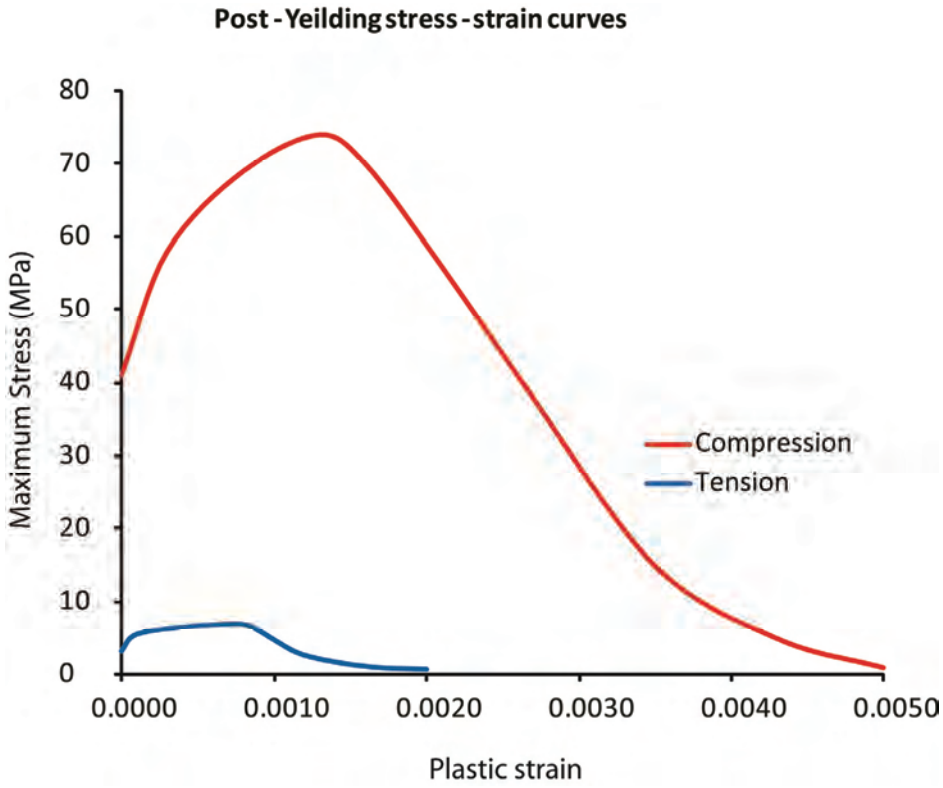

Figure 5.3: Post-yielding curves for plastic strain for the elastic-plastic-damage material. These parameters were entered directly into Abaqus. The values for tension (blue) and compression (red) are based on experimental data for Berea sandstone (Busetti, 2009, Ch. 2). The material is about 10 times stronger in compression.

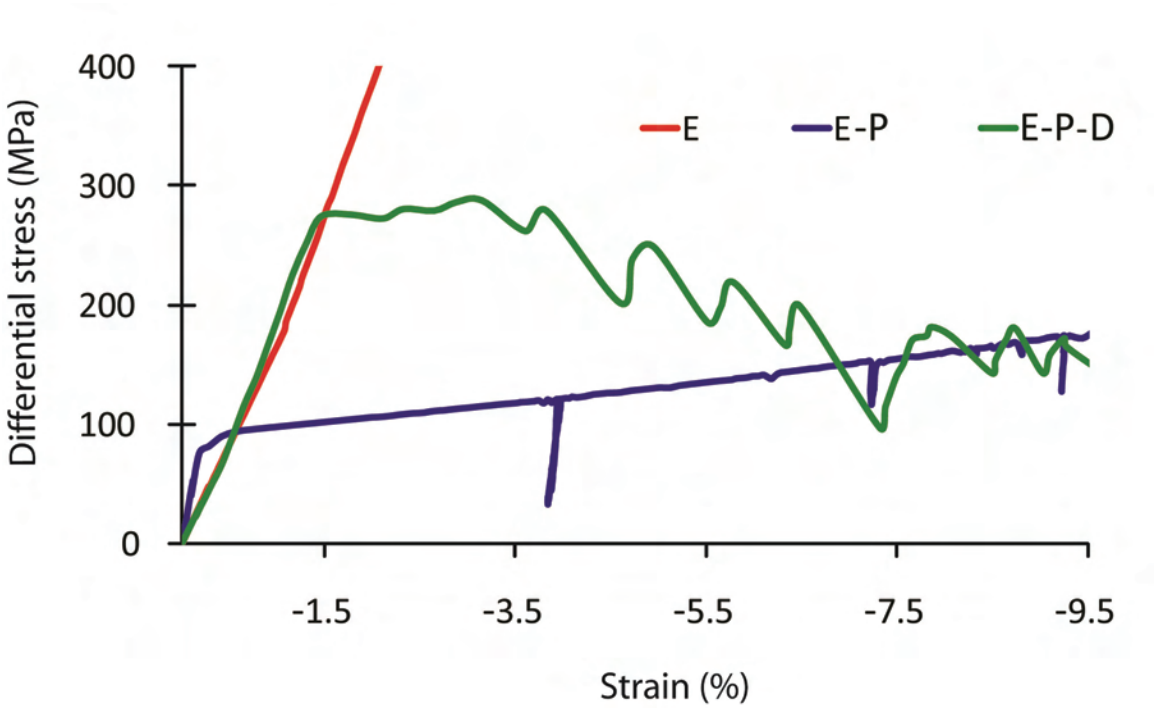

Figure 5.4: Stress-strain behavior for a single element during the same model runs, for the Elastic (E), Elastic-Plastic (E-P) and Elastic-Plastic-Damage (E-P-D) materials. The Elastic material is quasi-rigid for high amounts of strain. The post-peak behavior of the Elastic-Plastic-Damage material displays non-linear softening, highly dependent on the behavior of neighboring elements.

MODEL CONDITIONS

The model is solved with the explicit solver of Abaqus Student Edition v.6.72 that is well suited for large deformations, non-linearity and contact definitions. The displacement is applied linearly over the total time of 3.2×10^7 seconds. The size of the stable time increment in Abaqus is determined by the characteristic element dimension and the smallest dilatational wave speed of the material. For time efficiency a global semi-automatic mass scaling is used at the beginning of the displacement step, applied to the whole model, to target a stable time increment of 25 sec to approximate the solution. A total of 27 models were run for three inter-layer friction conditions, under three displacement boundary conditions for d_{left}, for three different rheologies (Table 5.4). Early termination of some models occurred, especially for elastic material rheology.

Rheology	Boundary condition	Inter-layer friction (μ)
E	$d_{left} = 0$	0
E-P	$d_{left} = ½\ d_{righ}$	0.4
E-P-D	$d_{left} = d_{righ}$	0.8

Table 5.4: Rheology, boundary conditions and inter-layer friction values used to run a total of 27 models.

RESULTS

STRAIN DISTRIBUTION

The stress-strain behavior of the rheology affects the distribution of strain during the transport of sediments over the ramp. The maximum principal strain for the elastic, elastic-plastic and elastic-plastic-damage material is displayed in Fig 5.5, 5.6 and 5.7

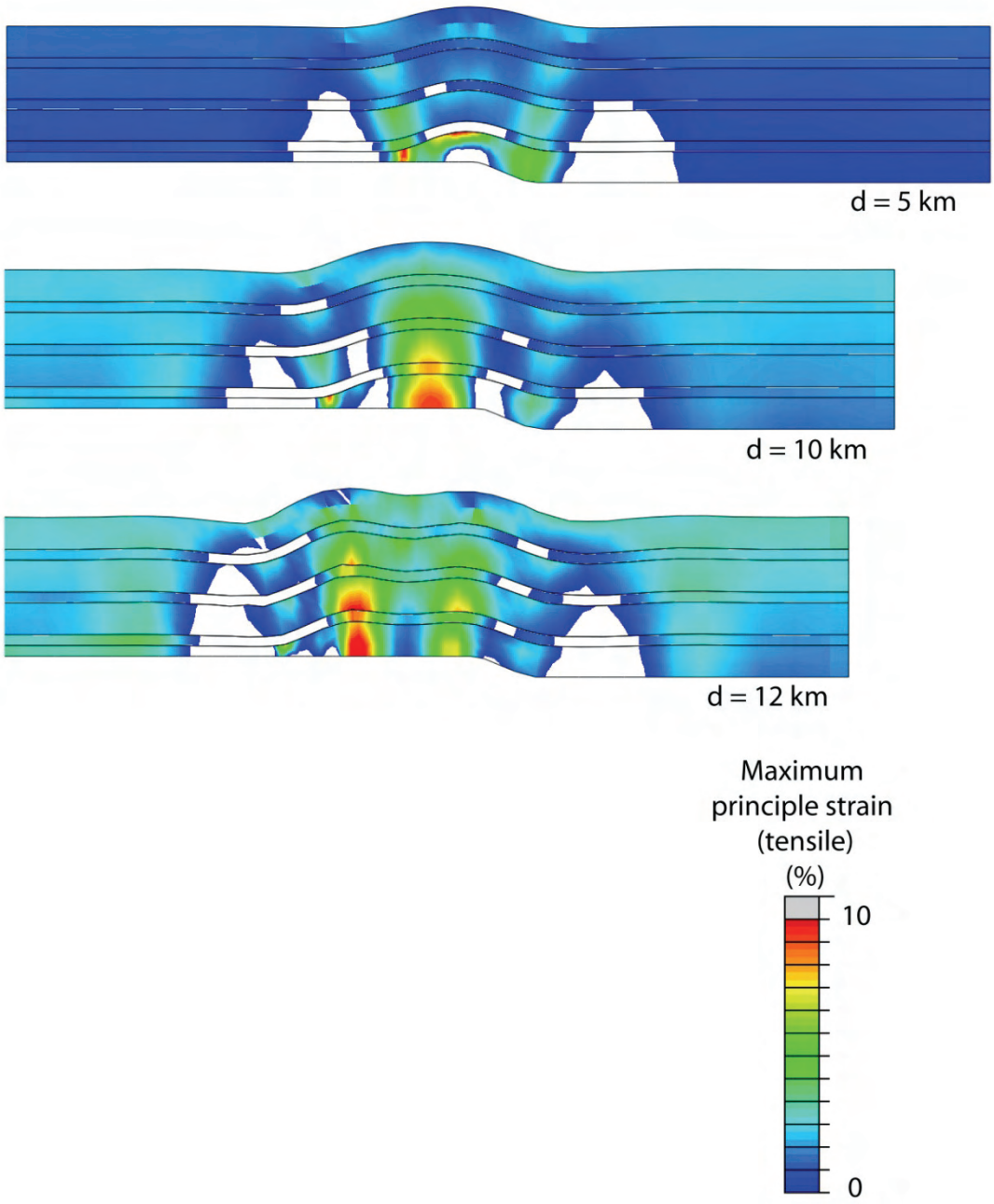

Figure 5.5: Maximum principal strain (extension) for elastic material, with inter-layer friction of 0.4 and d_{left} = ½ d_{righ}. Symmetrical anticlinal structure develops with extension strain localizing in the synclinal bends. With progressive deformation, extension strain increases in the crest, causing flattening of the crest and eventually development of a symmetric syncline. The model terminated numerically after a displacement of ~12 km.

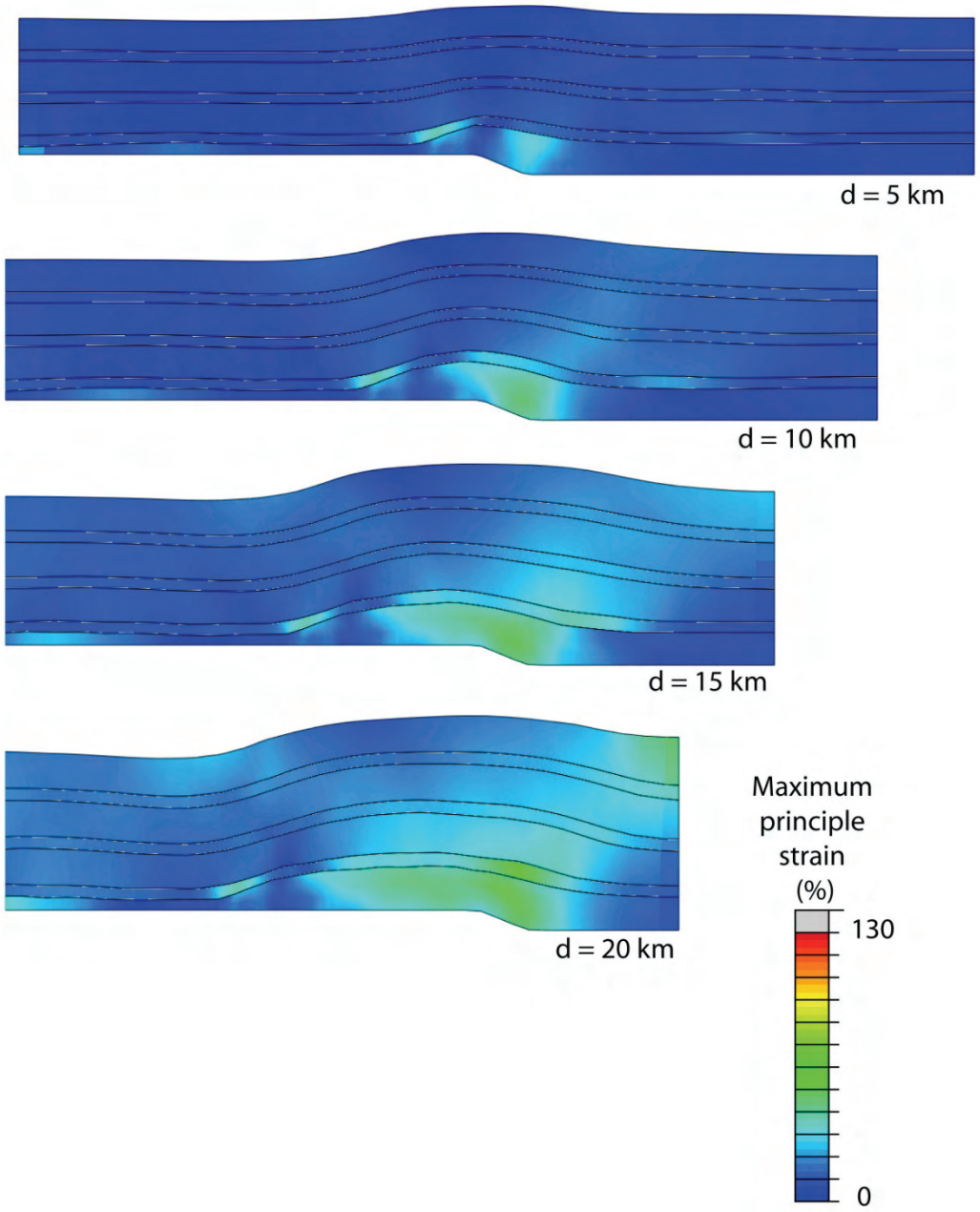

Figure 5.6: Maximum principal strain (extension) for elastic-plastic material, with inter-layer friction of 0.4 and d_{left} = ½ d_{righ}. Open asymmetric anticline develops with increased extensional strain within the lower layers above the ramp. The strain pattern is dominated by the strain histories as retained by the elements.

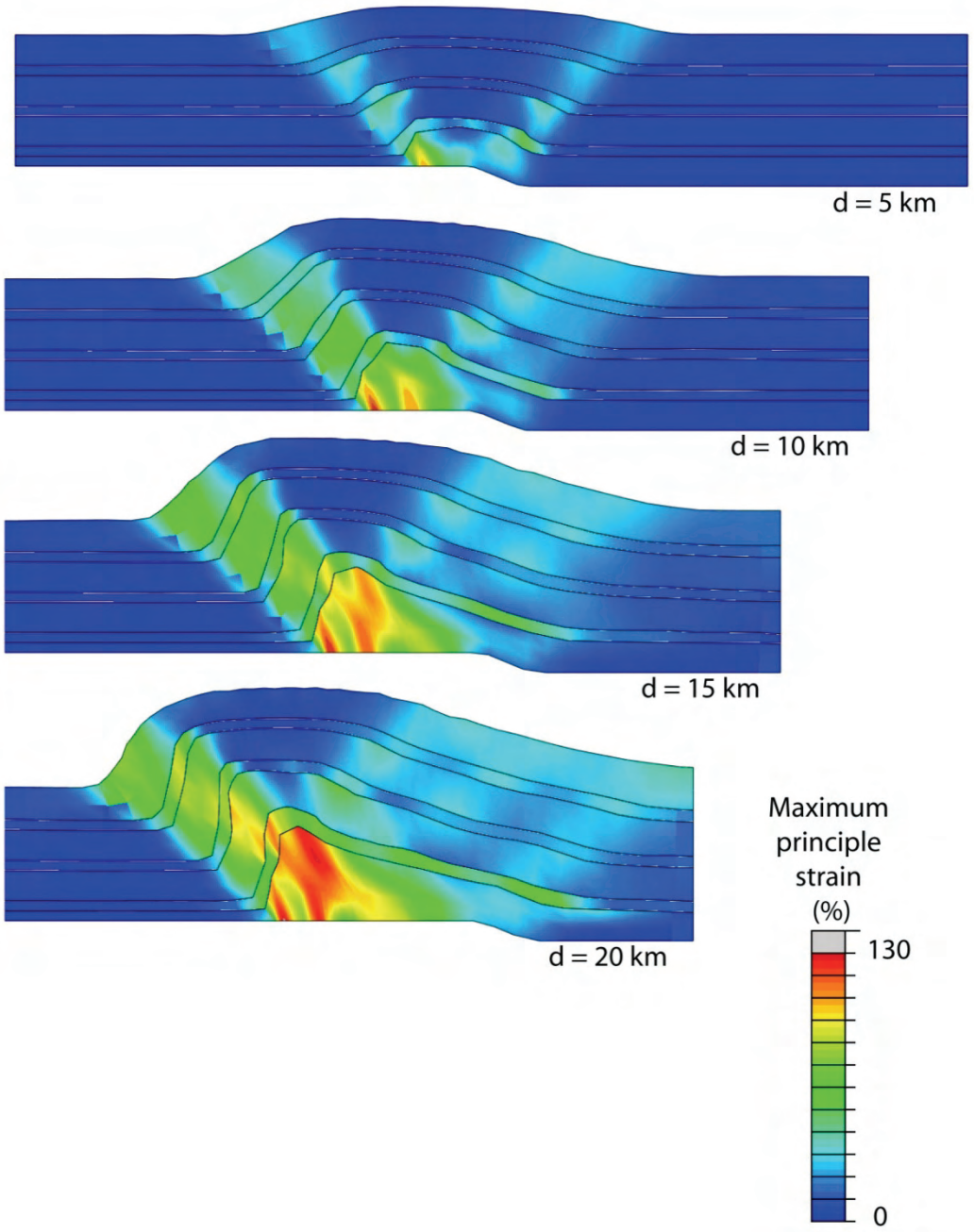

Figure 5.7: Maximum principal strain (extension) for elastic-plastic-damage material, with inter-layer friction of 0.4 and $d_{left} = ½\ d_{righ}$. A gentle open anticline develops that propagates into a highly asymmetric fold with steep front-limb. Increased extension strain is observed within the synclinal bends and within the fold hinge, where it increases with progressive deformation.

respectively, for model conditions with inter-layer friction of 0.4 and displacement boundary conditions of $d_{left} = ½ d_{righ}$. For each model the maximum principal strain for displacements of d_{right} = 5 km, 10km, 15 km and 20 km are displayed, unless the model terminated earlier due to numerical limitations. Note the different scale for the elastic material (Fig 5.5) which experiences significantly less strain due to its strength. Distinct features for the strain within each model are described below. Note that compressive strain is negative.

Elastic

Transportation of linear elastic layers over the ramp generates a symmetric anticlinal structure that develops in the early stage of deformation (Fig. 5.5). The amplitude of the fold increases with increasing deformation to maximum amplitude of ~1.5 km, while the crest of the anticline develops above the upper ramp-flat transition. Two zones of extension strain are recognized in the gentle synclinal bends of the structure; a stationary zone of increased strain located at the synclinal bend above the ramp, and a “mobile” zone of increased strain that traces the synclinal bend as it moves along the upper flat, with strain up to 4-5%. Progressive deformation leads to flattening of the crest of the anticline. This process initiates above the upper flat, within the lower layers, and is associated with a zone of increased extension strain up to 10% (d=10 km in Fig 5.5). The extension strain causing the flattening of the crest of the single anticline, eventually leads to the development of a gentle symmetric syncline. The model terminated numerically after a displacement of ~12 km.

Elastic-Plastic

A gentle, open anticline structure develops within the elastic-plastic rheology above the ramp (Fig 5.6). The structure develops a minor asymmetry with slightly steeper forelimb. Increased extension strain is observed within the lower layers above the ramp. Progressive deformation causes a minor increase of the extension strain up to ~65%; while material passes though this zone of increased strain, the strain pattern is dominated by the strain histories as retained by the elements. Progressive deformation leads to minor flattening of the crest of the structure, without significant effect on the extension strain as observed for the elastic rheology (Fig. 5.5).

Elastic-Plastic-Damage

In the early stage of deformation, the elastic-plastic-damage rheology displays a gentle, open anticlinal structure with a flat crest within the upper layers (Fig. 5.7); this structure is similar to the structure of monoclines (Reches and Johnson, 1978). The lower layers display an asymmetric anticline with a gentle dipping back-limb and a steeply dipping front-limb. Increased extension strain is observed within the synclinal bends of the structure, with a stationary zone of increased extension strain above the ramp and a mobile zone that traces the front-limb of the structure along the upper flat, similar to the elastic solution. Progressive deformation significantly steepens the front-limb of the structure while the dip of the back-limb does not change, resulting in a substantially asymmetric anticlinal structure. While the amount of strain at the back-limb remains at ~60%, significant localization of the tensile strain is observed within the steep to vertical front-limb of the structure. The strain localization increases with increasing deformation as the front-limb is transported along the upper flat (Fig. 5.7).

The distribution of strain for the solutions of the three rheologies is discontinuous at the layer boundaries, suggesting accommodation of deformation by flexural slip. Largest strain values are observed within the thicker layers (Fig 5.5, 5.6 and 5.7).

FOLD GEOMETRY

The presentation of the fold geometry is based on the deformation of the bottom of a marker bed (Fig. 5.8). The elevation of the bottom of the marker bed is subtracted from the original elevation before deformation, and plot against the horizontal distance from a pin-line (Fig 5.8). This analysis was done for all 27 models at the final stage after 20 km displacement, or for the maximum displacement that allowed comparison before the calculation was terminated.

No displacement at left side ($d_{left} = 0$)

The structure of the marker bed for boundary condition d_{left} = 0 km (Table 5.4) is illustrated in Fig. 5.9. The solution for the elastic rheology terminated numerically at d_{right} = 5 km. A symmetrical anticlinal structure developed for all three inter-layer frictions (Fig 5.9a). The amplitude of the anticlines decreases slightly with increasing friction. The crest of the anticline is located above the upper ramp-flat transition. Both the elastic-plastic and elastic-plastic-damage materials display asymmetric folding with development of steep to vertical anticlinal front-limbs and development of a foreland syncline. The gently dipping back-limbs are roughly parallel to the dip of the ramp, with exception of the elastic-plastic rheology with any inter-layer friction defined. The maximum curvature of the folds for the elastic-plastic and elastic-plastic solutions is located far away from the position of the ramp; ~11 km from the ramp for the elastic-plastic-damage solution, and ~ 7 km for the elastic plastic solution (Fig. 5.9).

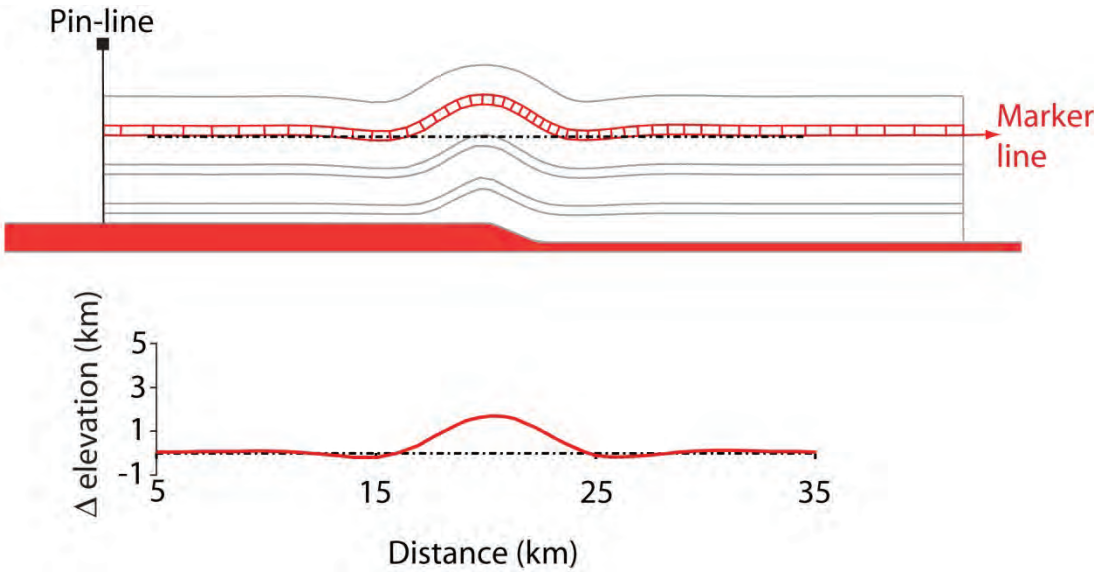

Figure 5.8: Presentation of the fold geometry, based on subtraction of the elevation of the bottom of a marker bed after deformation, from the original elevation.

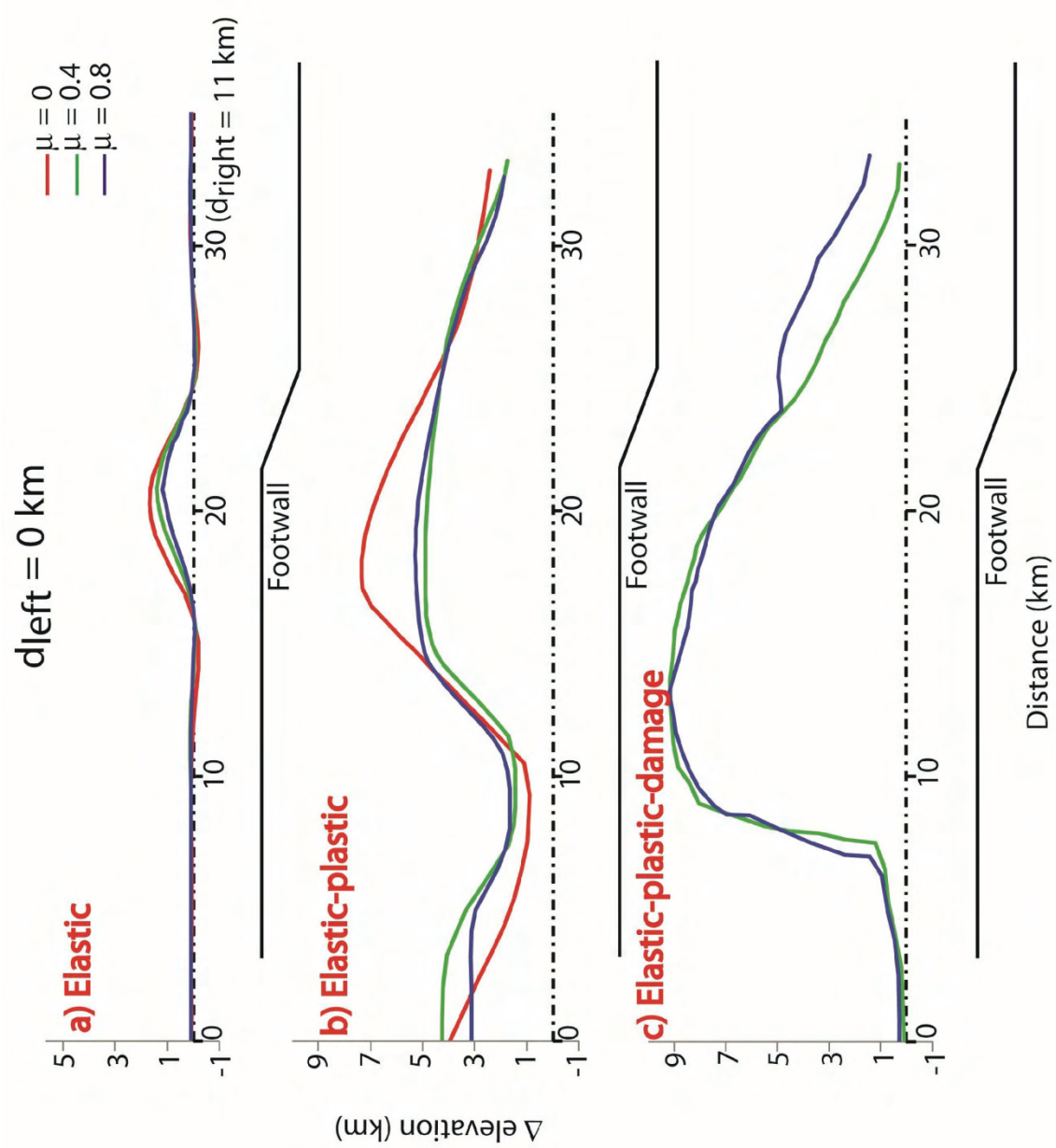

Figure 5.9: Structure of the marker bed for models with boundary condition d_{left} = 0 km. A) Elastic models develop symmetrical anticlines. Results are displayed for displacements of 11 km. B) Elastic-Plastic models develop asymmetric anticlines with front-limb synclines. Maximum curvature occurs far away from the ramp. C) Elastic-Plastic-Damage models develop highly asymmetric anticlines with high amplitude of folding with elevations up to 9 km and steep to vertical front-limbs. Maximum curvature occurs far away from the ramp. For all models an increase in friction results in decreasing folding amplitudes.

Furthermore, the amplitude of ~ 9 km for the folds of the elastic-plastic-damage solution is almost twice as much as the amplitude of the elastic-plastic solution of ~5 km, for similar inter-layer friction,

Partial displacement at left side (d_{left} = 1/2 d_{right})

For this boundary condition, similar features are observed as described for the above condition; the elastic solution is symmetric (Fig. 5.10a), the fold structure is asymmetric for the elastic-plastic rheology, with steep front limb and gentle dipping back-limb, and significantly asymmetric with nearly vertical front-limb for the elastic-plastic-damage rheology. A distinct difference, however, is that for all rheologies, more open fold develop, with generally lower amplitudes, and wider spread of folding.

Full displacement at left side (d_{left} = d_{right})

All three rheologies display gentle open anticlinal structures with a flat crest that extends for several kilometers (Fig. 5.11). The amplitude of folding is significantly lower with respect to the previously described models. The dip of the front- and back-limb for the elastic and elastic-plastic solutions is roughly identical; hence the folding structure is symmetrical. The elastic-plastic-damage solution displays an asymmetric structure with a steeper back-limb. Although generally the inter-layer friction does not significantly affect the folding geometry for this boundary condition, the elastic-plastic-damage solution displays a smoother and more symmetric structure with lower fold amplitude for zero inter-layer friction.

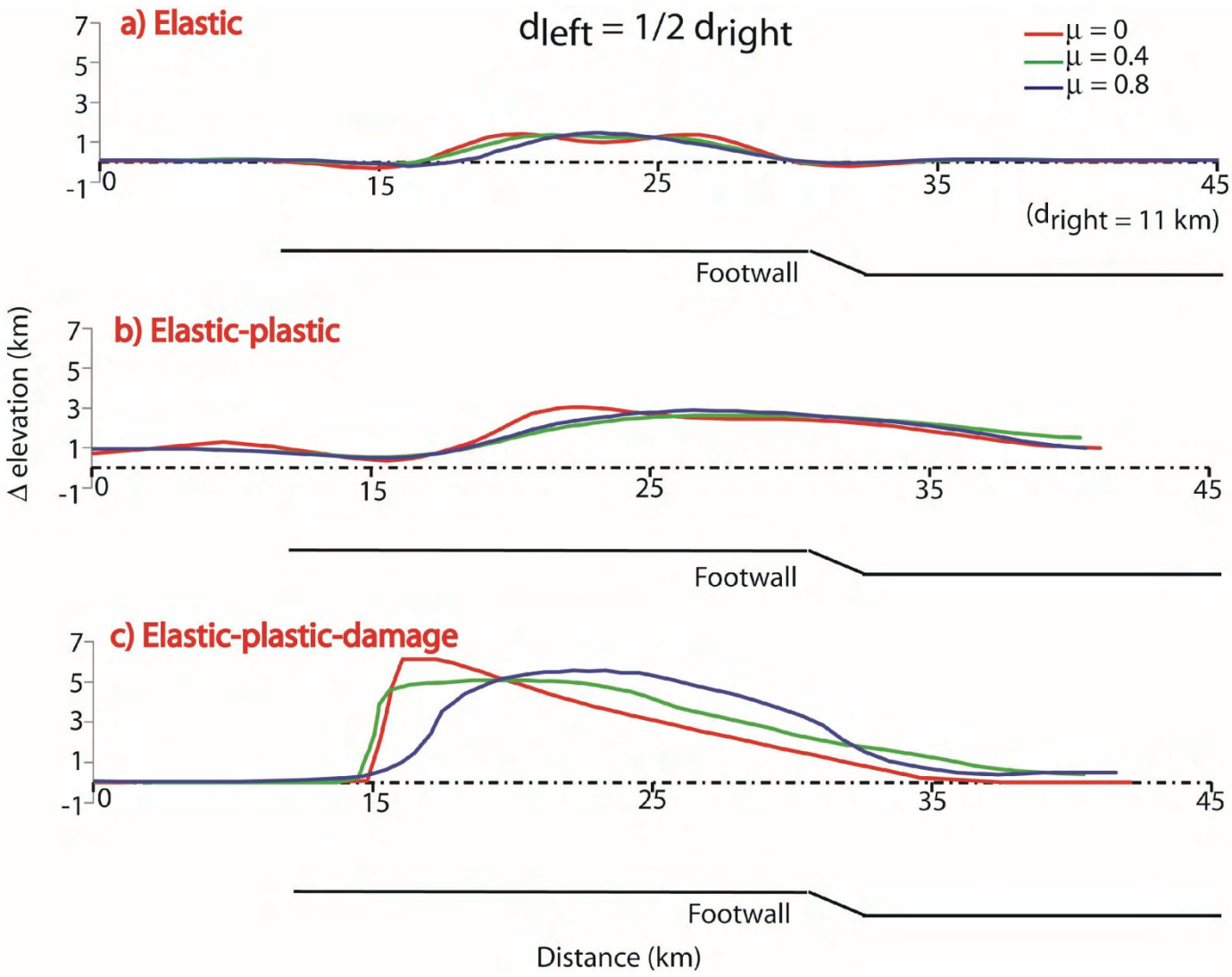
a) Elastic
$d_{left} = 1/2\ d_{right}$
μ = 0
μ = 0.4
μ = 0.8
7
5
3
1
-1
0
15
25
35
45
(d_{right} = 11 km)
Footwall
b) Elastic-plastic
Δ elevation (km)
Footwall
c) Elastic-plastic-damage
Footwall
Distance (km)

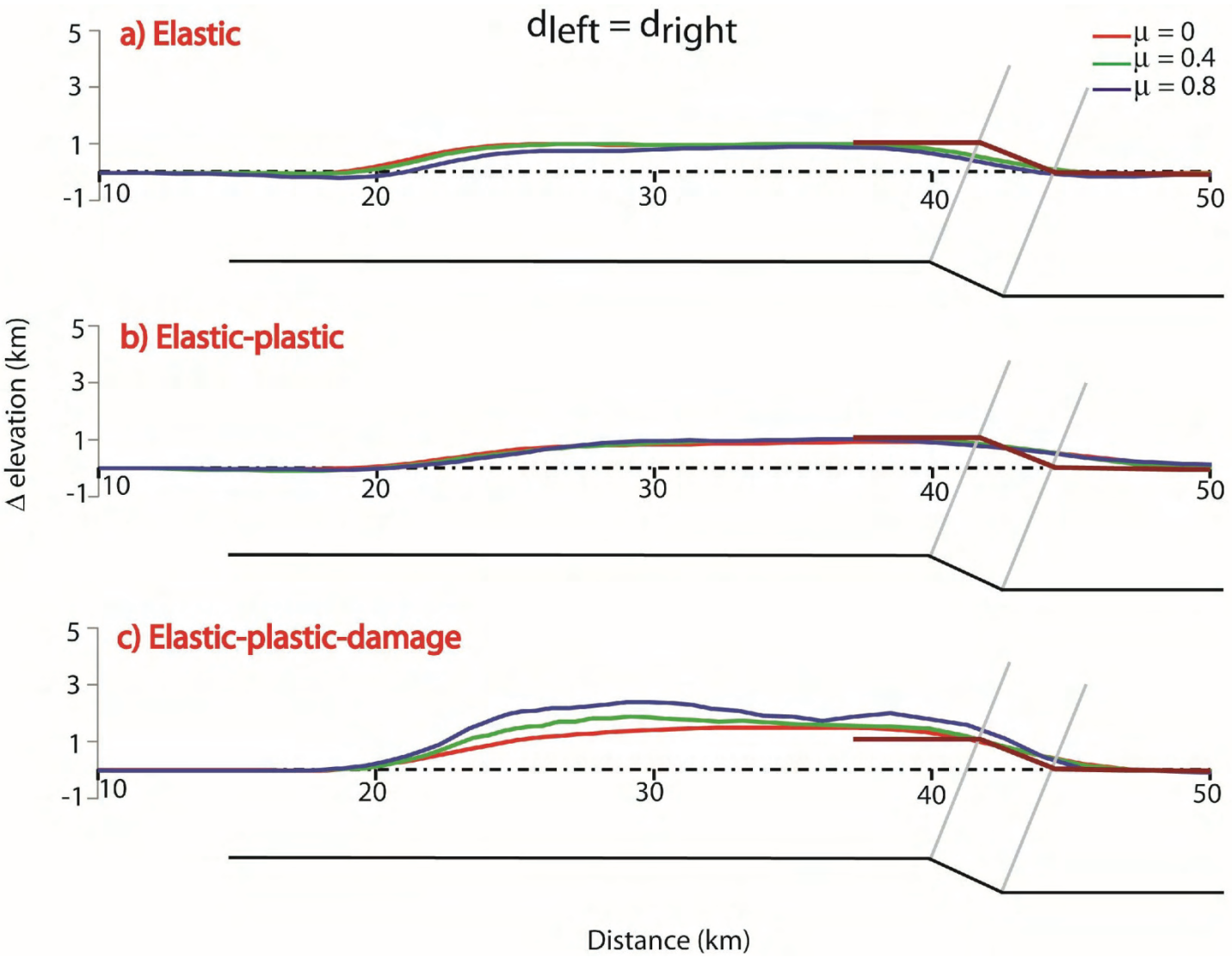
a) Elastic
dleft = dright
μ = 0
μ = 0.4
μ = 0.8
b) Elastic-plastic
c) Elastic-plastic-damage
Δ elevation (km)
Distance (km)
5
3
1
-1
10
20
30
40
50

Figure 5.10: Structure of the marker bed for models with boundary condition d_{left} = ½ d_{right}. A) Elastic models develop symmetrical anticlinal structures. Results are displayed for displacements of 11 km. B) Elastic-Plastic models develop open anticlinal structures with slightly steeper front-limbs. C) Elastic-Plastic-Damage models develop highly asymmetric anticlines with high amplitude of folding and steep to vertical front-limbs. Maximum curvature occurs far away from the ramp. For all models an increase in friction results in decreasing folding amplitudes.

Figure 5.11: Structure of the marker bed for models with boundary condition $d_{left} = d_{right}$. A) Elastic models develop open symmetrical anticlinal structures with flat crestal region. B) Elastic-Plastic models develop open anticlinal structures with flat crestal region. C) Elastic-Plastic-Damage models develop open anticlines. Increasing friction results in a smoother solution. The models under this boundary condition are most conform to the Rich model (Rich, 1934). The expected position and inclination of the layers at the back-limb, according to Suppe (1983) is displayed in red. The elastic-plastic-damage rheology displays the best fit, with back-limb layers being parallel to the ramp.

VOLUMETRIC STRAIN

The volumetric strain is calculated for each element and the final stage of deformation. Fig. 5.12 displays the volumetric change for the elastic-plastic and elastic-plastic-damage rheology for boundary condition of $d_{left} = ½ d_{righ}$ and inter-layer friction of 0.4. The elastic-plastic solution displays minor compaction of almost the entire sedimentary package. Compaction is largest at the ramp, with values up to 3%. The elastic-plastic-damage solution displays dominantly dilatational volume changes, with localization within the steep to vertical front-limb of the structure and values up to 50%. To accommodate such significant values of strain, those areas are expected to be highly deformed with faults and fractures.

SYNTHESIS

The above simulations lead to the following main observations:

1. The inter-layer friction has limited effect on the final geometry of folds above the ramp. Increase of inter-layer friction generally leads to a decrease in fold amplitude.

2. The boundary displacements, expressed by the ratio RD= d_{left}/d_{right} (Fig. 2), have a major influence on the fold geometry. Fig. 5.13 displays nine fold shapes for the inter-layer friction of 0.4, and it shows that for smaller RD (with $d_{left} = 0$ indicating RD = 0), the final ramp -fold geometry is characterized by the following:

    1) Increase of fold amplitude.
    2) Amplification of a syncline at the front-limb of the anticlinal fold.
    3) Increase in distance of maximum deformation with respect to the ramp position.

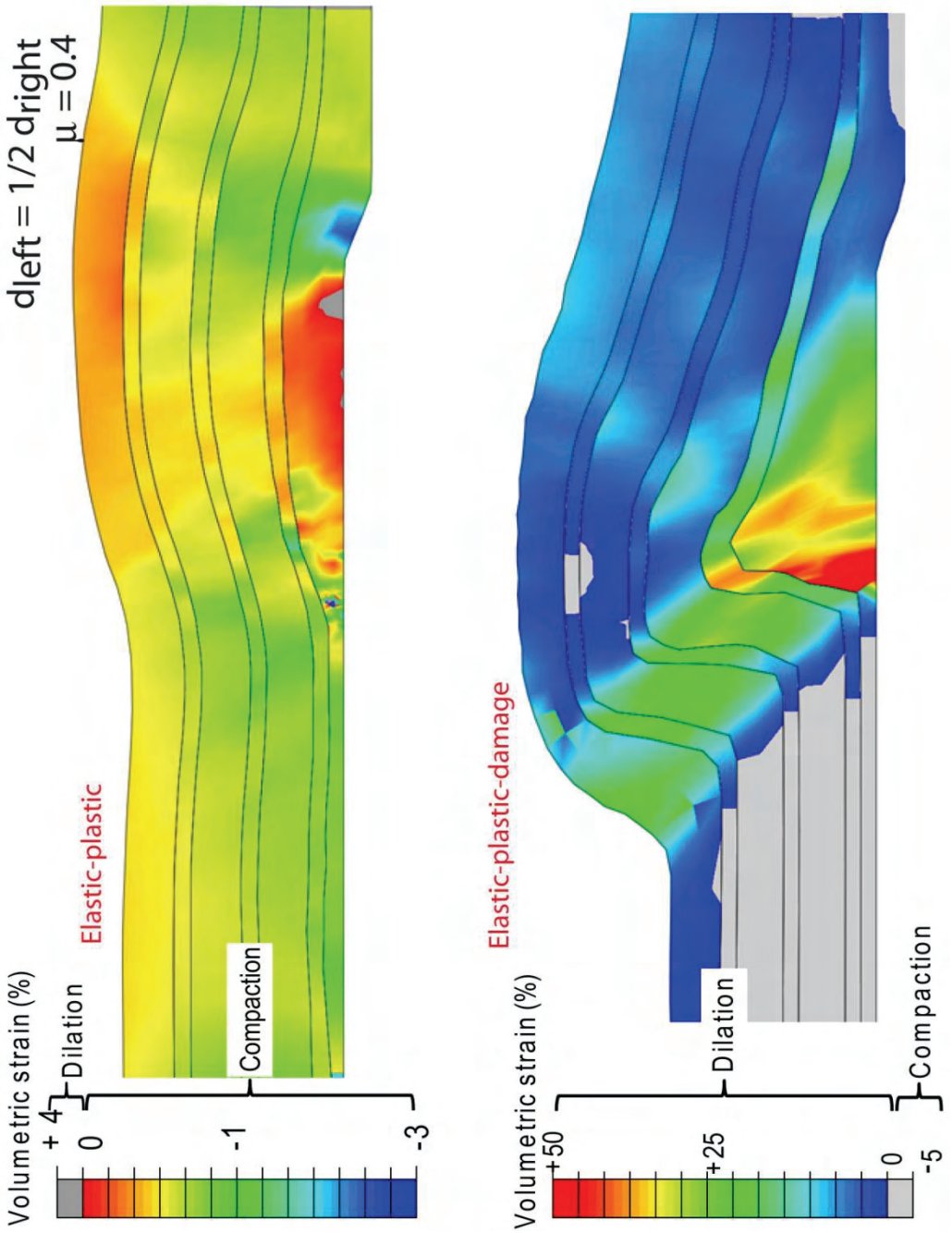

Figure 5.12: Volumetric change for elastic-plastic and elastic-plastic-damage rheology for boundary condition d_{left} = ½ d_{righ} and inter-layer friction of 0.4. The elastic-plastic solution displays minor compaction, while the elastic-plastic-damage solution displays dominantly dilatational volume change with values up to 50 % in the fold hinge.

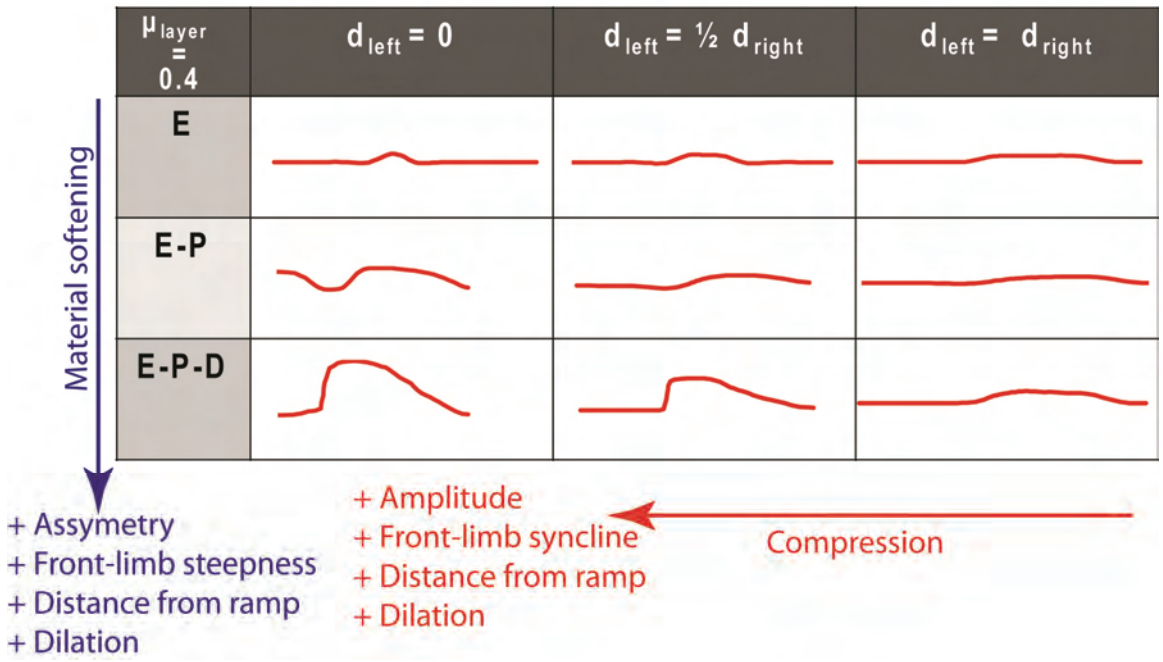

Figure 5.13: Summary of the effect of material softening and boundary conditions on the geometry of the final ramp-related fold, solutions with inter-layer friction of 0.4. Inter-layer friction has limited effect on the final geometry, with increasing friction resulting in a decrease of fold amplitude.

4) Increase in dilation.

3. The results indicate that softer rheology, controlled by plasticity for the elastic-plastic, and post peak behavior (strain softening) for the elastic-plastic-damage material, lead to the following (Fig. 5.13):

1) Increase of fold asymmetry.
2) Increase in front-limb steepness.
3) Increase in distance of maximum deformation with respect to the ramp position.
4) Increase in dilation.

DISCUSSION

Several scenarios have been proposed to explain asymmetric folding above ramp structures. Berger and Johnson (1980) suggested low-amplitude asymmetrical fold in the hanging wall prior to translation up the ramp, where the asymmetry reflects high drag on the thrust surface; Allmendinger (1981) suggested that folds in the Meade thrust sheet became highly asymmetric after the frontal thrust and folds locked. Analogue modeling of ramp-related folding by Chester et al. (1991), describes the influence of layering on ramp-related folding. Their model consists of a single layer of sandstone with a saw-cut, with overlain limestone inter-layered with mica or lead, subjected to shortening to form a ramp structure. They observe symmetric folds that develop for inter-layers of lead, while the weaker mica layers produce significant asymmetric folding. Chester et al. (1991) suggested that the fold asymmetry results from strain-induced weakening of the hanging wall. Our model supports this suggestion, as asymmetric folding is observed for the

elastic-plastic-damage rheology (Fig. 5.9, 5.10 and 5.11), that undergoes significant strain softening (Fig. 5.3 and 5.4).

The model used for this analysis is based on a simplified ramp model (Fig. 5.1) that follows from the model of Rich (1934). The results comparable to results of the model of Rich are for boundary condition $d_{left} = d_{right}$ (Fig. 5.11). Independent of rheology, a wide open anticlinal structure with a flat crest that extends for several km is formed. It was suggested by Suppe (1983) that layers at the back-limb of the anticlinal structure are parallel to the fault-ramp, representing the inclination of the ramp. The expected position and inclination of the back-limb, displayed in red in Fig. 5.11, has a significantly shallower inclination for both the elastic and elastic-plastic model solutions. The elastic-plastic-damage solution however, displays a better fit with the expected inclination of the back-limb. Suppe (1983) also suggested that the length of the crest of the anticline is directly related to the amount of displacement along the fault. Our results are in general agreement with this result as the length of the crests is ~ 20km, equal to the amount of applied displacement, independent of rheology (Fig. 5.11). In fact, the total width of the anticlines that developed under the other two boundary conditions is roughly equal to the applied displacement. Therefore, the total width of the anticline that forms above the ramp can be used as first-order approximation for the amount of displacement along the fault, independent of rheology, inter-layer friction or boundary conditions.

REFERENCES

Allmendinger, R. W., 1981, Structural geometry of Meade thrust plate in northern Blackfoot Mountains, southeastern Idaho: AAPG Bulletin, v. 65, p. 509-525.

An, L. J., and C. G. Sammis, 1996, Development of strike-slip faults: shear experiments in granular materials and clay using a new technique: Journal of Structural Geology, v. 18, p. 1061-1077.

Anderson, E. M., 1951, The Dynamics of Faulting: Oliver and Boyd, Edinburgh, 2nd ed, p. 191 pp.

Armstrong, R. A., W. Compston, E. A. Retief, I. S. Williams, and H. J. Welke, 1991, Zircon ion microprobe studies bearing on the age and evolution of the Witwatersrand triad: Precambrian Research, v. 53, p. 243-266.

Aydin, A., and A. M. Johnson, 1978, Development of faults as zones of deformation bands and as slip surfaces in sandstone: Pure and Applied Geophysics, v. 116, p. 931-942.

Barton, C. A., and M. D. Zoback, 1994, Stress perturbations associated with active faults penetrated by boreholes: possible evidence for near-complete stress drop and a new technique for stress magnitude measurement.: Journal of Geophysical Research, v. 99, p. 9373-9390.

Beeler, N. M., T. F. Wong, and S. H. Hickman, 2003, On the Expected Relationships among Apparent Stress, Static Stress Drop, Effective Shear Fracture Energy, and Efficiency: Bulletin of the Seismological Society of America, v. 93, p. 1381-1389.

Berger, P., and A. M. Johnson, 1980, First-order analysis of deformation of a thrust sheet moving over a ramp: Tectonophysics, v. 70, p. T9-T24.

Bobich, J. K., 2005, Experimental analysis of the extension to shear fracture transition in Berea sandstone Master's Thesis, Texas A&M University, College Station, p. 1-52.

Boettcher, M., A. McGarr, M. Johnston, T. H. Jordan, V. Heesakkers, and Z. Reches, 2007, Constraints on Seismogenesis of Small Earthquakes ($-2.8 \leq MW \leq 3$) Defined by the Dense Instrument Network of the Natural Earthquake Laboratory in South African Mines (NELSAM): Eos Trans. AGU, 88(52), Fall Meet. Suppl., Abstract S33D-02.

Boettcher, M. S., A. McGarr, and M. Johnston, 2009, Extension of Gutenberg-Richter distribution to M_w -1.3, no lower limit in sight: Geophys. Res. Lett., v. 36.

Boettcher, M. S., A. McGarr, M. Johnston, G. van Aswegen, V. Heesakkers, and Z. Reches, 2006, Analysis of a M2.2 Earthquake in Tautona Gold Mine, South

Africa, and Estimate of its Energy Budget: Eos Trans. AGU, 87(52), Fall Meet. Suppl., Abstract S43C-06.

Boyer, S. E., and D. Elliott, 1982, Thrust systems: AAPG Bulletin, v. 66, p. 1196-1230.

Brace, W. F., and J. B. Walsh, 1962, Some direct measurements of the surface energy of quartz and orthoclase: The American Mineralogist, v. 47, p. 1111–1122.

Brady, B. H. G., and E. T. Brown, 1993, Rock mechanics for underground mining: 2nd. ed. Chapman and Hall, London, p. 571.

Brodsky, E. E., and H. Kanamori, 2001, Elastohydrodynamic lubrication of faults: J. Geophys. Res., v. 106.

Busetti, S., 2009, Fracturing of Layered Reservoir Rocks: Dissertation, University of Oklahoma, p. 1-256.

Caine, J. S., J. P. Evans, and C. B. Forster, 1996, Fault zone architecture and permeability structure: Geology, v. 24, p. 1025-1028.

Cartwright, P., and G. Walker, 2000, In-situ stress measurement, 83 level shaft pillar area, TauTona mine, AngloGold.

Chester, F. M., J. P. Evans, and R. L. Biegel, 1993, Internal structure and weakening mechanisms of the San Andreas Fault: Journal of Geophysical Research, v. 98, p. 771-786.

Chester, J. S., F. M. Chester, and A. K. Kronenberg, 2005, Fracture surface energy of the Punchbowl fault, San Andreas system: Nature, v. 437, p. 133-136.

Chester, J. S., J. M. Logan, and J. H. Spang, 1991, Influence of layering and boundary conditions on fault-bend and fault-propagation folding: Geological Society of America Bulletin, v. 103, p. 1059-1072.

Dahlstrom, C. D. A., 1970, Structural geology in the eastern margin of the canadian rocky mountains: Bulletin of Canadian Petroleum Geology, v. 18, p. 332-406.

Di Toro, G., D. L. Goldsby, and T. E. Tullis, 2004, Friction falls towards zero in quartz rock as slip velocity approaches seismic rates: Nature, v. 427, p. 436-439.

Dieterich, J. H., 1978, Time-dependent friction and the mechanics of stick-slip: Pure and Applied Geophysics, v. 116, p. 790-806.

Dor, O., Z. Reches, and G. van Aswegen, 2001, Fault zones associated with the Matjhabeng earthquake 1999, South Africa: Rockburst and Seismicity in Mines, RaSiM5 (Proceedings), South African Inst. of Mining and Metallurgy, p. 109–112.

Douglas, R. J. W., 1950, Callum Creek, Langford Creek, and Gap Map-Areas: Alberta: Geological survey of Canada Memoir, v. 255, p. 124 p.

Elliott, D., 1976, The Energy Balance and Deformation Mechanisms of Thrust Sheets: Philosophical Transactions of the Royal Society of London. Series A, Mathematical and Physical Sciences, v. 283, p. 289-312.

Engelder, J. T., 1974, Cataclasis and the Generation of Fault Gouge: Geological Society of America Bulletin, v. 85, p. 1515-1522.

Erickson, G. S., and W. R. Jamison, 1995, Viscous-plastic finite-element models of fault-bend folds: Journal of Structural Geology, v. 17, p. 561-573.

Erickson, S. G., 1996, Influence of mechanical stratigraphy on folding vs faulting: Journal of Structural Geology, v. 18, p. 443-450.

Faulkner, D. R., T. M. Mitchell, D. Healy, and M. J. Heap, 2006, Slip on "weak" faults by the rotation of regional stress in the fracture damage zone: Nature, v. 444, p. 922-925.

Fossen, H., R. A. Schultz, Z. K. Shipton, and K. Mair, 2007, Deformation bands in sandstone: a review: Journal of the Geological Society, v. 164, p. 755-769.

Friedman, M., J. Handin, and G. Alani, 1972, Fracture-surface energy of rocks: International Journal of Rock Mechanics and Mining Sciences, v. 9, p. 757-766.

Frimmel, H. E., and W. E. L. Minter, 2002, Recent developments concerning the geological history and genesis of the Witwatersrand gold deposits, South Africa: Society of Economic Geologists Special Publication, v. 9, p. 17-45.

Germanovich, L. N., R. L. Salganik, A. V. Dyskin, and K. K. Lee, 1994, Mechanisms of brittle fracture of rock with pre-existing cracks in compression: Pure and Applied Geophysics, v. 143, p. 117-149.

Gibson, M. A. S., S. J. Jolley, A. C. Barnicoat, and L. M. Gochioco, 2000a, Interpretation of the Western Ultra Deep Levels 3-D seismic survey: The Leading Edge, v. 19, p. 730-735.

Gibson, R. L., W. U. Reimold, D. Phillips, and P. W. Layer, 2000b, (super 40) Ar/ (super 39) Ar constraints on the age of metamorphism in the Witwatersrand Supergroup, Vredefort Dome (South Africa): South African Journal of Geology, v. 103, p. 175-190.

Grice, A. G., 1998, Underground mining with backfill: Proceedings of the 2nd Annual Summit -Mine Tailings Disposal Systems, Brisbane, Australia, p. 234–239.

Harris, L. D., and R. C. Milici, 1977, Characteristics of thin-skinned style of deformation in the southern Appalachians, and potential hydrocarbon traps: Related Information: Geological Survey Professional Paper 1018, 44 p.

Haskell, N. A., 1964, Total energy and energy spectral density of elastic wave radiation from propagating faults: Bulletin of the Seismological Society of America, v. 54, p. 1811-1841.

Healy, D., 2008, Damage patterns, stress rotations and pore fluid pressures in strike-slip fault zones: J. Geophys. Res., v. 113.

Hickman, S., and M. Zoback, 2004, Stress orientations and magnitudes in the SAFOD pilot hole: Geophys. Res. Lett., v. 31.

Huntoon, P. W., 1974, Synopsis of Laramide and post-Laramide structural geology of the eastern Grand Canyon, Arizona: In: Eastwood, R.L., Karlstrom, T.N.V., Swann, G.A. (Eds.), Geology of Northern Arizona, Part 1ÐRegional Studies, Northern Arizona University, Flagsta, Arizona, p. 317-355.

Jaeger, J., and N. Cook, 1976, Fundamentals of rock mechanics, New York: John Wiley, p. 585.

Johnson, A. M., 1970, Physical Processes in Geology, W. H. Freeman, New York, p. 577 pp.

Johnson, A. M., and P. Berger, 1989, Kinematics of fault-bend folding: Engineering Geology, v. 27, p. 181-200.

Johnson, A. M., and R. C. Fletcher, 1994, Folding of Viscous Layers: Mechanical Analysis and Interpretation of Structures in Deformed Rock: Columbia University Press, 461pp.

Kamo, S. L., W. U. Reimold, T. E. Krogh, and W. P. Colliston, 1996, A 2.023 Ga age for the Vredefort impact event and a first report of shock metamorphosed zircons in pseudotachylitic breccias and granophyre: Earth and Planetary Science Letters, v. 144, p. 369-387.

Kanamori, H., 2004, The diversity of the physics of earthquakes: Proceedings of the Japan Academy. Series B: Physical and Biological Sciences, v. 80, p. 297-316.

Katz, O., M. C. Gilbert, Z. e. Reches, and J. C. Roegiers, 2001, Mechanical properties of the Mount Scott Granite, Wichita Mountains, Oklahoma: Oklahoma Geology Notes, v. 61, p. 28-34.

Katz, O., and Z. e. Reches, 2004, Microfracturing, damage, and failure of brittle granites: Journal of Geophysical Research, v. 109, p. no.B1, 13.

Katz, Y., R. Weinberger, and A. Aydin, 2004, Geometry and kinematic evolution of Riedel shear structures, Capitol Reef National Park, Utah: Journal of Structural Geology, v. 26, p. 491-501.

Killick, A., A. Thwaites, G. Germs, and A. Schoch, 1988, Pseudotachylite associated with a bedding-parallel fault zone between the Witwatersrand and Ventersdorp Supergroups, South Africa: Geologische Rundschau, v. 77, p. 329-344.

Kirsch, G., 1898, Die Theorie der Elastizitat und die Bedurfnisse der Festigkeitslehre. VDI Z, v. 42, p. 707.

Lachenbruch, A. H., 1980, Frictional heating, fluid pressure, and the resistance to fault motion: J. Geophys. Res., v. 85, p. 6249-6272.

Lin, A., 1994, Microlite Morphology and Chemistry in Pseudotachylite, from the Fuyun Fault Zone, China: The Journal of Geology, v. 102, p. 317-329.

Lofgren, G., 1971, Experimentally Produced Devitrification Textures in Natural Rhyolitic Glass: Geological Society of America Bulletin, v. 82, p. 111-124.

Lowell, J. D., 1995, Mechanics of basin inversion from worldwide examples: Geological Society, London, Special Publications, v. 88, p. 39-57.

Lucier, A. M., M. D. Zoback, V. Heesakkers, Z. e. Reches, and S. K. Murphy, 2009, Constraining the far-field in situ stress state near a deep South African gold mine: International Journal of Rock Mechanics and Mining Sciences, v. 46, p. 555-567.

Ma, K.-F., H. Tanaka, S.-R. Song, C.-Y. Wang, J.-H. Hung, Y.-B. Tsai, J. Mori, Y.-F. Song, E.-C. Yeh, W. Soh, H. Sone, L.-W. Kuo, and H.-Y. Wu, 2006, Slip zone and energetics of a large earthquake from the Taiwan Chelungpu-fault Drilling Project: Nature, v. 444, p. 473-476.

Mair, K., and C. Marone, 2000, Shear Heating in Granular Layers: Pure and Applied Geophysics, v. 157, p. 1847-1866.

Marone, C., 1998, The effect of loading rate on static friction and the rate of fault healing during the earthquake cycle: Nature, v. 391, p. 69-72.

McCarthy, T. S., I. G. Stanistreet, and L. J. Robb, 1990, Geological studies related to the origin of the Witwatersrand Basin and its mineralization; an introduction and a strategy for research and exploration: South African Journal of Geology, v. 93, p. 1-4.

McGarr, A., M. Boettcher, J. B. Fletcher, R. Sell, M. J. S. Johnston, R. Durrheim, S. Spottiswoode, and A. Milev, 2009, Broadband Records of Earthquakes in Deep Gold Mines and a Comparison with Results from SAFOD, California: Bulletin of the Seismological Society of America, v. 99, p. 2815-2824.

McGarr, A., and N. C. Gay, 1978, State of Stress in the Earth's Crust: Annual Review of Earth and Planetary Sciences, v. 6, p. 405-436.

McGarr, A., D. D. Pollard, N. C. Gay, and W. D. Ortlepp, 1979, Observations and Analysis of Structures in Exhumed Mine-induces Faults: Proceedings of Conference VIII: Analysis of Actual Fault Zones in Bedrock (U.S. Geol. Survey, Menlo Park. Open file Rep. 79-1239), p. 101-120.

McGarr, A., S. M. Spottiswoode, and N. C. Gay, 1975, Relationship of mine tremors to induced stresses and to rock properties in the focal region: Bulletin of the Seismological Society of America, v. 65, p. 981-993.

Melosh, H. J., 1996, Dynamical weakening of faults by acoustic fluidization: Nature, v. 379, p. 601-606.

Mitra, S., 1988, Three-dimensional geometry and kinematic evolution of the Pine Mountain thrust system, southern Appalachians: Geological Society of America Bulletin, v. 100, p. 72-95.

Mitra, S., 1990, Fault-propagation folds: Geometry, kinematic evolution, and hydrocarbon traps: Journal Name: AAPG Bulletin (American Association of Petroleum Geologists); (USA); Journal Volume: 74:6, p. Medium: X; Size: Pages: 921-945.

Mitra, S., and J. S. Namson, 1989, Equal-area balancing: Am. J. Sci, v. 289, p. 563-599.

Moore, D. E., and M. J. Rymer, 2007, Talc-bearing serpentinite and the creeping section of the San Andreas fault: Nature, v. 448, p. 795-797.

Muhuri, S. K., T. A. Dewers, T. E. Scott, and Z. e. Reches, 2003, Interseismic fault strengthening and earthquake-slip instability; friction or cohesion?: Geology, v. 31, p. 881-884.

Olgaard, D. L., and W. F. Brace, 1983, The microstructure of gouge from a mining-induced seismic shear zone: International Journal of Rock Mechanics and Mining Sciences & Geomechanics Abstracts, v. 20, p. 11-19.

Ortlepp, W. D., 1992, Note on fault-slip motion inferred from a study of micro-cataclastic particles from an underground shear rupture: Pure and Applied Geophysics, v. 139, p. 677-695.

Ortlepp, W. D., 2000, Observation of mining-induced faults in an intact rock mass at depth: International Journal of Rock Mechanics and Mining Sciences, v. 37, p. 423-436.

Oudmayer, B. C., and J. de Jager, 1993, Fault reactivation and oblique-slip in the Southern North Sea: Geological Society, London, Petroleum Geology Conference series, v. 4, p. 1281-1290.

Peska, P., and M. D. Zoback, 1995, Compressive and tensile failure of inclined well bores and determination of in situ stress and rock strength: J. Geophys. Res., v. 100.

Raleigh, C. B., and D. T. Griggs, 1963, Effect of the Toe in the Mechanics of Overthrust Faulting: Geological Society of America Bulletin, v. 74, p. 819-830.

Ramsey, J. M., and F. M. Chester, 2004, Hybrid fracture and the transition from extension fracture to shear fracture: Nature, v. 428, p. 63-66.

Reches, Z., 1978, Development of monoclines: Part I, structure of the Palisades Creek branch of the East Kaibab monocline, Grand Canyon, Arizona: Matthews, V. (Ed.), Laramide Folding Associated with Basement Block Faulting in the Western United States, Memoir 151. Geological Society of America, v. 151, p. 235-273.

Reches, Z., 1988, Evolution of fault patterns in clay experiments: Tectonophysics, v. 145, p. 141-156.

Reches, Z., 2006, Building a natural earthquake laboratory at focal depth: Scientific Drilling, v. 3, p. 30-33.

Reches, Z., and T. A. Dewers, 2005, Gouge formation by dynamic pulverization during earthquake rupture: Earth and Planetary Science Letters, v. 235, p. 361-374.

Reches, Z., and H. Ito, 2007, Scientific drilling of active faults: past and future: Harms, U., Koeberl, C., and Zoback, MD. (Eds.) Scientific Drillings Continental Scientific Drilling A Decade of Progress, and Challenges for the Future. Springer, p. 235-258.

Reches, Z., and A. M. Johnson, 1978, Development of monoclines: Part II, theoretical analysis of monocline: Matthews, V. (Ed.), Laramide Folding Associated with Basement Block Faulting in the Western United States, Memoir 151. Geological Society of America, v. 151, p. 273-311.

Reches, Z., D. Lockner, D. E. Moore, and S. Madden, 2009, Dynamic Weakening During Earthquakes by Gouge Lubrication: Eos Trans. AGU, 90(52), Fall Meet. Suppl., Abstract T52A-03.

Reimold, W. U., 1995, Pseudotachylite in impact structures -- generation by friction melting and shock brecciation?: A review and discussion: Earth-Science Reviews, v. 39, p. 247-265.

Rice, J. R., 1992, Fault stress states, pore pressure distributions, and the weakness of the San Andreas Fault, *in* B. Evans, and W. Tf, eds., Fault mechanics and transport properties of rock: london, Acedemic press Inc., p. 475-504.

Rich, J. L., 1934, Mechanics of low-angle overthrust faulting as illustrated by Cumberland thrust block, Virginia, Kentucky, and Tennessee: AAPG Bulletin, v. 18, p. 1584-1596.

Robb, L. J., E. G. Charlesworth, G. R. Drennan, R. L. Gibson, and E. L. Tongu, 1997, Tectono-metamorphic setting and paragenetic sequence of Au-U mineralisation in the Archaean Witwatersrand Basin, South Africa: Australian Journal of Earth Sciences, v. 44, p. 353-371.

Rodgers, J., 1963, Mechanics of appalachian foreland folding in Pennsylvania and west Virginia: AAPG Bulletin, v. 47, p. 1527-1536.

Royse, F., Jr., M. A. Warner, and D. L. Reese, 1975, Thrust belt oof Wyoming, Idaho and northern Utah: Structural geometry and related problems: Bolyard, D.W., ed., Symposium on deep drilling frontiers in central Rocky Mountains: Denver, Colorado, Rocky Mountain Association of Geologics, p. 41-54.

Rubey, W. W., and K. M. Hubbert, 1965, Role of Fluid Pressure in Mechanics of Overthrust Faulting: Reply: Geological Society of America Bulletin, v. 76, p. 469-474.

Scholz, C. H., 1998, Earhquakes and friction laws: Nature, v. 391, p. 6.

Scholz, C. H., 2002, The mechanics of earthquakes and faulting: Cambridge, Cambridge university press.

Sibson, R. H., 1975, Generation of Pseudotachylyte by Ancient Seismic Faulting: Geophysical Journal of the Royal Astronomical Society, v. 43, p. 775-794.

Spray, J. G., 1995, Pseudotachylyte controversy: Fact or friction?: Geology, v. 23, p. 1119-1122.

Stein, R. S., and G. Ekstrom, 1992, Seismicity and Geometry of a 110-km-Long Blind Thrust Fault 2. Synthesis of the 1982â€“1985 California Earthquake Sequence: J. Geophys. Res., v. 97.

Stewart, R. A., W. U. Reimold, E. G. Charlesworth, and W. D. Ortlepp, 2001, The nature of a deformation zone and fault rock related to a recent rockburst at Western Deep Levels Gold Mine, Witwatersrand Basin, South Africa: Tectonophysics, v. 337, p. 173-190.

Suppe, J., 1983, Geometry and kinematics of fault-bend folding: American Journal of Science, v. 283, p. 684-721.

Swanson, S. E., and P. M. Fenn, 1986, Quartz crystallization in igneous rocks: American Mineralogist, v. 71, p. 331-342.

Tembe, S., D. Lockner, and T.-f. Wong, 2009, Constraints on the stress state of the San Andreas Fault with analysis based on core and cuttings from San Andreas Fault Observatory at Depth (SAFOD) drilling phases 1 and 2: J. Geophys. Res., v. 114.

Thatcher, W., 1983, Nonlinear Strain Buildup and the Earthquake Cycle on the San Andreas Fault: J. Geophys. Res., v. 88.

Townend, J., and M. D. Zoback, 2004, Regional tectonic stress near the San Andreas fault in central and southern California: Geophys. Res. Lett., v. 31.

Tsutsumi, A., and T. Shimamoto, High-velocity Frictional Properties of Gabbro: Geophys. Res. Lett., v. 24.

van Aswegen, G., and A. G. Butler, 1993, Applications of Quantitative Seismology in SA Gold Mines: In: Young, R.P. (Ed.) Rockbursts and Seismicity in Mines, Balkema, Rotterdam.

Ward, J. A., G. F. Slater, D. P. Moser, L. H. Lin, G. Lacrampe-Couloume, A. S. Bonin, M. Davidson, J. A. Hall, B. Mislowack, R. E. S. Bellamy, T. C. Onstott, and B. Sherwood Lollar, 2004, Microbial hydrocarbon gases in the Witwatersrand Basin, South Africa: Implications for the deep biosphere: Geochimica et Cosmochimica Acta, v. 68, p. 3239-3250.

Weinberger, R., Z. Reches, A. Eidelman, and T. S. Scott, 1994, Tensile properties of rocks in four-point beam tests under confining pressure: Proceedings of the first North American Rock Mechanics Symposium, eds Nelson, P. & Laubach, S.E., A.A. Balkema, Rotterdam., p. 435–442.

Wenk, H. R., 1978, Are pseudotachylites products of fracture or fusion?: Geology, v. 6, p. 507-511.

Wesnousky, S. G., 1988, Seismological and structural evolution of strike-slip faults: Nature, v. 335, p. 340-343.

Wilson, B., T. Dewers, Z. e. Reches, and J. N. Brune, 2005, Particle size and energetics of gouge from earthquake rupture zones: Nature, v. 434, p. 749-752.

Wiltschko, D. V., 1979, A Mechanical Model for Thrust Sheet Deformation at a Ramp: J. Geophys. Res., v. 84.

Wiprut, D., and M. D. Zoback, 2000, Fault reactivation and fluid flow along a previously dormant normal fault in the northern North Sea: Geology, v. 28, p. 595-598.

Yamamoto, K., N. Sato, and Y. Yabe, 2000, Stress state around the Nojima faultestimated from core measurments: Proceedings of the International Workshop on the Nojima Fault Core and Borehole Data Analysis, p. 239-246.

Zechmeister, M. S., V. Heesakkers, K. Moore, C. Campher, and Z. Reches, 2005, Sintered cataclasite of the Archaean Pretorius fault zone, TauTona mine, South Africa: Eos Trans. AGU, 86(52), Fall Meet. Suppl, Abstract S31B-05.

Zoback, M. D., C. A. Barton, M. Brudy, D. A. Castillo, T. Finkbeiner, B. R. Grollimund, D. B. Moos, P. Peska, C. D. Ward, D. J. Wiprut, and J. A. Hudson, 2003, Determination of stress orientation and magnitude in deep wells: International Journal of Rock Mechanics and Mining Sciences, v. 40, p. 1049-1076.

Zoback, M. D., M. L. Zoback, V. S. Mount, J. Suppe, J. P. Eaton, J. H. Healy, D. H. Oppenheimer, P. A. Reasenberg, L. M. Jones, C. B. Raleigh, I. G. Wong, O. Scotti, and C. M. Wentworth, 1987, New evidence on the state of stress of the San Andreas fault system: Science, v. 238, p. 1105-1111.

Zoback, M. L., M. D. Zoback, J. Adams, M. Assumpcao, S. Bell, E. A. Bergman, P. Blumling, N. R. Brereton, D. Denham, J. Ding, K. Fuchs, N. Gay, S. Gregersen, H. K. Gupta, A. Gvishiani, K. Jacob, R. Klein, P. Knoll, M. Magee, J. L. Mercier, B. C. Muller, C. Paquin, K. Rajendran, O. Stephansson, G. Suarez, M. Suter, A. Udias, Z. H. Xu, and M. Zhizhin, 1989, Global patterns of tectonic stress: Nature, v. 341, p. 291-298.